Coda-Wave Monitoring of Continuously Evolving Material Properties

Zotz-Wilson, Reuben

DOI
10.4233/uuid:9c0b2f03-040b-4ec8-b669-951c5acf1f3b

Publication date
2020

Document Version
Final published version

Citation (APA)
Zotz-Wilson, R. (2020). *Coda-Wave Monitoring of Continuously Evolving Material Properties*. [Dissertation (TU Delft), Delft University of Technology]. https://doi.org/10.4233/uuid:9c0b2f03-040b-4ec8-b669-951c5acf1f3b

CODA-WAVE MONITORING OF CONTINUOUSLY EVOLVING MATERIAL PROPERTIES

Reuben Zotz-Wilson

Coda-Wave Monitoring of Continuously Evolving Material Properties

Coda-Wave Monitoring of Continuously Evolving Material Properties

Dissertation

for the purpose of obtaining the degree of doctor
at Delft University of Technology,
by the authority of the Rector Magnificus, prof. dr. ir. T.H.J.J. van der Hagen,
chair of the Board for Doctorates,
to be defended publicly on
Wednesday, 25 March 2020 at 10:30 o'clock

by

Reuben Denley ZOTZ-WILSON

Master of Science in Applied Geophysics, Delft University of Technology/Eidgenössische Technische Hochschule, Zürich/Rheinisch-Westfälische Technische Hochschule, Aachen
born in Tasmania, Australia

This dissertation has been approved by the promotors:

Prof. dr. ir. C. P. A. Wapenaar
Dr. A. Barnhoorn

Composition of the doctoral committee:

Rector Magnificus	chairman
Prof. dr. ir. C. P. A. Wapenaar	Delft University of Technology, promotor
Dr. A. Barnhoorn	Delft University of Technology, copromotor

Independent members:

Prof. dr. ir. E. C. Slob	Delft University of Technology
Prof. dr. L. G. Evers	Delft University of Technology
Prof. dr. C. J Spiers	Utrecht University
Dr. D. J Verschuur	Delft University of Technology
Dr. A. Obermann	Eidgenössische Technische Hochschule, Zürich

TU Delft

Keywords: coda-wave monitoring, material failure, pore-pressure, early warning systems.

Cover illustration: Reuben Zotz-Wilson generated with imagery created by the Generative Adversarial Network provided by `https://deepdreamgenerator.com`.

ISBN 978-94-6366-262-8

Typesetting system: LaTeX.
Printed in The Netherlands by Gildeprint B.V., Enschede.

An electronic version of this dissertation is available at
`http://repository.tudelft.nl/`.

To

Katja
and my children Anfim and Miron,
for filling my life with love, laughter, and laundry

Summary

Coda-Wave Monitoring of Continuously Evolving Material Properties

We all monitor the world around us through waves. After about sixteen weeks in the womb, the ears and eyes of an infant child begin to deliver the first signals of light and sound waves to the brain. In fact, one could argue that consciousness itself is the feeling one receives when processing large amounts of wavefield data. Despite the integral presence of wavefield monitoring in biology, it is only since the dawn of the information age, that society has been able to monitor the world around us with similar fidelity. Where a recorded wavefield can be assumed to have travelled through a simple medium, it is often possible to resolve an image, though where a disordered medium is encountered, and the wavefield is multiply scattered, this becomes more difficult. It is this disordered portion of a wavefield, often referred to as the coda-wave, which this thesis is primarily concerned with. By considering the coda-wave over the coherent arrivals, one loses the ability to resolve the structure of a medium, though in turn gains improved sensitivity to changes within. This makes coda-wave monitoring particularly well suited to problems in which sensitivity to change is a more important quality than the ability to image the medium. On face value, one might consider coda-wave derived monitoring within Early Warning Systems (EWSs), towards hazards such as earthquakes, landslides, or the failure of critical infrastructure. However, operational deployment of such systems must work from simple, robust, and automated alert criteria, and therefore often rely on coherent wavefield observations, typically through passive measurements at the boundary of a region of interest. It is due to this reliance on clear, automated alert criteria derived from passive observation, which limits the lead time provided by EWSs, from only a few tens of seconds for earthquakes, to one day of warning for landslides.

While coda-wave monitoring methods may present the greatest utility within

early warning systems, there are many areas of research where the objective is to simply quantify the evolution of a particular quantity. Various works have demonstrated the sensitivity of the coda-wave to changes in temperature, velocity, water saturation, and inelastic deformation. An improved phenomenological understanding of the response of the coda-wave under such perturbations is required. This is particularly true in the field of rock mechanics, where considerable effort is made to understand the subtle grain-scale processes which occur under different in-situ conditions.

Therefore, this thesis works towards both the improved utility of the coda-wave within operational monitoring systems, while advancing the understanding of its phenomenological response to different grain-scale changes. This is formed into the following related research objectives:

- The development of robust continuous coda-wave derived monitoring systems. To extract key precursory indicators to the onset of inelastic material deformation. This is considered as an initial step, enabling the eventual automation in EWS.
- Improving the characterisation of inelastic deformation within experimental rock mechanics, through the application of coda-wave derived monitoring methods.
- The demonstration of the spatial imaging capabilities of the coda-wave, during laboratory testing of samples tested under subsurface conditions.

This thesis begins with a mostly methodological study into the robustness of the coda-wave under continuous transient, or sudden large perturbations. It is shown that where a fixed reference material state is considered when monitoring the evolution of inelastic strain, a rapid decay in sensitivity of the system is experienced. An alternative rolling-reference material state is presented, from which clear indicators to the subtle onset of inelastic deformation are determined. It is postulated that the use of such a rolling-reference approach, combined with an active source will advance the utility of the coda-wave within continuous monitoring systems, and in particular EWSs.

This is followed by a study into the coda-wave response of samples from the seismogenic Groningen Gas Field, which are subjective to pore-pressure depletion. It is shown that through the application of coda-wave derived velocity, scattering power, and intrinsic/scattering attenuation, an improved understanding of the grain-scale compaction process is possible. Specifically, it is indicated that the evolution of inelastic strain does not progressively increase with increasing effective stress, but develops in serial stages of predominantly intergranular closure, followed by predominantly intergranular slip. It is postulated that this is the result of continuous stress redistribution within the grain structure. For high porosity samples, the changes in intrinsic attenuation indicate the eventual pervasive formation of intragranular cracks, while for the lower porosity samples the pervasive total closure of crack space is indicated. The implications of these observations on induced seismicity monitoring and geomechanical modelling are discussed.

In the final research chapter of this thesis, the possibility of combining the sensitivity of the coda-wave, while retaining the ability to image the change within a medium is discussed. Specifically, three mudstone samples of different initial water saturation, subjected to triaxial compaction, are monitored via multiple receivers, alternating between active and passive surveying. This experimental design allows for the comparison between the sensitivity of both active and passive Acoustic Emissions (AEs) monitoring. Through the application of an inversion scheme which is based on the approximation of diffusive energy density, the formation of initially microscopic, leading to eventual macroscopic fracturing is monitored within the three-dimensional core volume. These data suggest that the evolution of fracturing within saturated mudstones occurs in several stages of reactivation, with the onset occurring at less than fifty-percent of peak stress. Importantly, for all samples, no AEs were detected, which suggests that these mudstones deform mostly plastically. This has important implications on both the study of aseismic lithology within the laboratory and more critically the assumptions surrounding AE monitoring in the field.

In summary, this thesis presents the advantages of active source, coda-wave derived monitoring within both experimental rock mechanics research, and operational early warning detection systems. This thesis concludes with a proposed research methodology which has the objective unifying the sensitivity provided by the coda-wave, with the requirements for automated detection within Early Warning Systems.

Samenvatting

Monitoren met de coda-golf van doorlopend veranderende materiaal eigenschappen

We zien allemaal de wereld om ons heen met behulp van golven. Nadat een kind ongeveer zestien weken in de baarmoeder is gegroeid beginnen de ogen en oren voor het eerst signalen veroorzaakt door licht- en geluidsgolven naar het brein te sturen. Je zou zelfs kunnen stellen dat het bewustzijn het gevoel is dat men krijgt wanneer men een grote hoeveelheid data in de vorm van golven probeert te verwerken. Hoewel het monitoren van golven een belangrijk onderdeel is in de biologie, is de mensheid pas sinds het begin van het informatietijdperk in staat om de wereld om ons heen te monitoren met vergelijkbare nauwkeurigheid. Als een golfveld door een simpel medium is gepropageerd, is het meestal mogelijk om een beeld van het medium te construeren. Als het medium echter onregelmatig van aard is, waardoor het golfveld meerdere keren wordt weerkaatst, wordt het construeren van een beeld van het medium moeilijker. In dit proefschrift ligt de aandacht voornamelijk op het onregelmatige deel van het golfveld, dat vaak wordt aangduid als de coda-golf. Als men de coda-golf bestudeert in plaats van de coherente golven, wordt het construeren van het beeld van het medium moeilijker, maar wordt de gevoeligheid voor de eigenschappen van het medium sterker. Dit maakt het monitoren met de coda-golf erg geschikt voor situaties waar het bepalen van de eigenschappen van het medium belangrijker is dan de structuur van het medium. Op het eerste gezicht zou het logisch zijn om gebruik te maken van de techniek van het monitoren van de coda-golf in Early Warning Systems (EWSs), die gebruikt worden om gevaren zoals aardbevingen, landverschuivingen of het falen van belangrijke infrastructuren te meten. De operationale opzet van deze systemen is echter gebaseerd op simpele, robuste en automatische waarschuwingscriteria, waardoor ze afhankelijk zijn van het meten van de coherente golfvelden, die meestal gemeten worden op de rand van een gebied van interesse. Door deze afhankelijkheid van duidelijke criteria van passieve metingen

is de voorspellingstijd van EWSs beperkt, beginnend met slechts enkele tientallen seconden voor een aardbeving tot hooguit een dag voor een landverschuiving.

Hoewel methodes voor het monitoren van de coda-golf mogelijk het meest zin hebben voor EWSs zijn er vele takken van onderzoek waar het bepalen van de verandering van een bepaalde kwantiteit het belangrijkste doel is. Verschillende onderzoeken hebben aangetoond dat de coda-golf gevoelig is voor veranderingen in temperatuur, snelheid, water saturatie en niet-elastische deformatie. Een groter begrip van het fenomeen dat de respons coda-golf op dit soort veranderigen veroorzaakt is daarom nodig. Dit is vooral van belang in het veld van de gesteente-mechanica, waar het begrijpen van de subtiele processen die op de korrelschaal werken en onder verschillende omstandigheden onstaan een hoofddoel is.

Vanwege deze redenen is dit proefschrift gericht op het verbeteren van de toepassing van de operationele opzet van het monitoren, terwijl tegelijk het begrip van het fenomeen dat de respons van de coda-golf als gevolg van verschillende veranderingen op de korrelschaal bepaalt wordt verbeterd. Dit leidt tot de volgende onderzoeksdoeleinden:

- Het ontwikkelen van robuuste systemen die continu de coda-golf monitoren. Het bepalen van belangrijke inleidende indicatoren die het begin van niet-elastische deformatie kunnen aanduiden. Dit wordt gezien als een eerste stap, die voor het uiteindelijke automatiseren van een EWS mogelijk maakt.

- Het verbeteren van het bepalen van de niet-elastische deformatie met behulp van experimentele gesteente mechanica, met behulp van de methodes die gebruik maken van het monitoren van de coda-golf.

- Het demonstreren van de mogelijkheden om een ruimtelijk beeld van een medium te maken met behulp van de coda-golf, door middel van het testen van monsters in het lab onder ondergrond omstandigheden.

Dit proefschrift begint met een overwegend methodologisch onderzoek naar hoe robuust de coda-golf is onder geleidelijke of plotseling grote veranderingen. Er wordt aangetoond dat als er bij het monitoren van de verandering van de niet-elastische rek gebruik wordt gemaakt van een materiaal toestand met vaste referentie waardes, er een snelle afname van de gevoeligheid van het systeem wordt waargenomen. Een alternatieve materiaal toestand met wisselende waardes wordt gepresenteerd, waar duidelijke indicatoren worden waargenomen die het subtiele begin van niet-elastische deformatie aangeven. Er wordt gepostuleerd dat het gebruik van een systeem met wisselende waardes samen met metingen van een actieve bron de toepassing van de coda-golf in systemen die doorlopend monitoren kunnen verbeteren, voornamelijk voor EWSs.

Vervolgens wordt er een studie van coda golf responsies gepresenteerd, van monsters uit het seismogenische Groningen gasveld die gevoelig zijn voor afname van de druk in de poriën. Er wordt aangetoond dat het gebruik van de snelheid, verstrooiïngsvermogen en intrinsieke/verstrooiïng demping die uit de coda-golf wordt afgeleid meer inzicht geeft in de compactie processen op de korrelschaal. Er wordt specifiek aangetoond dat de evolutie van niet-elastische rek niet toeneemt met de stijging van

de effectieve stress, maar zich ontwikkelt in stadia van overwegend intergranulaire afdichting, gevolgd door overwegend intergranulaire slip. Er wordt gepostuleerd dat dit het resultaat is van de doorlopende spanningsverdeling binnen de korrelstructuur. Voor monsters met hoge porositeit geven de veranderingen in intrinsieke demping van de energie de uiteindelijke vorming van intragranulaire scheuren aan, terwijl voor de monsters met lagere porositeit de totale sluiting van ruimte van de scheuren wordt aangegeven. De gevolgen van deze observaties op monitoring van geïnduceerde seismiciteit en geomechanische modellering worden besproken.

In het laatste onderzoekshoofdstuk van dit proefschrift wordt de mogelijkheid besproken om de gevoeligheid van de coda-golf te combineren met behoud van het vermogen om de verandering van het beeld van het medium te verkrijgen. In het bijzonder worden drie kleisteenmonsters met verschillende initiële waterverzadiging, blootgesteld aan triaxiale compactie, gemonitord met meerdere ontvangers, waarbij actieve en passieve metingen afgewisseld worden. Deze experimentele opzet maakt het mogelijk om een vergelijking te maken tussen de gevoeligheid van zowel actieve als passieve monitoring van de Akoestische Emissies (AE). Met gebruik van een inversie systeem, dat is gebaseerd op de benadering van diffusieve energiedichtheid, wordt de vorming van aanvankelijk microscopische breking, wat uiteindelijk leidt tot macroscopische breking binnen het driedimensionale kernvolume, gemonitord. Deze gegevens suggereren dat de ontwikkeling van breuk in verzadigde kleistenen plaatsvindt in verschillende stadia van heractivering, waarbij het begin van de breking onstaat als de piekspanning minder dan vijftig procent is. Het is belangijk dat voor alle monsters geen AE werd gedetecteerd, wat suggereert dat deze kleistenen meestal plastisch vervormen. Dit heeft belangrijke gevolgen voor de studie van aseismische lithologie in het laboratorium en voornamelijk voor de aannames rond AE-monitoring in het veld.

Samengevat presenteert dit proefschrift de voordelen van het gebruik van het monitoren met de coda golf met actieve bronnen voor zowel experimenteel onderzoek naar gesteentemechanica als operationele EWSs. Dit proefschrift wordt afgesloten met een voorstel voor een onderzoeksmethode die tot doel heeft om de gevoeligheid van de coda golf te combineren met de vereisten voor geautomatiseerde detectie voor EWSs.

Contents

1

Introduction

"By sacrificing order for disorder,
one gains sensitivity to change"

The rapid increase in societies ability to monitor both the earth [*Obregon et al.*, 2018; *Zhao*, 2019], and the built environment [*Brownjohn*, 2007; *Stähli et al.*, 2015] has to a large extent been driven by the combination of affordable sensors, and the ability to transmit large amounts of data wirelessly. Due to their ubiquitous presence, wave phenomena play a critical role in the monitoring of changes at both the surface, and within a medium. Where one can comfortably assume the wavefield remains coherent, investigation is possible through conventional imaging techniques based on geometrical considerations. However, where the wavefield interacts with disordered media and is multiply scattered, diffusive transport begins to govern the distribution of energy - akin to the Brownian motion of particles. The question of whether a propagating wavefield perceives a medium as homo- or heterogeneous is one of scale. For a certain density ρ_n of scatterers, where their size a_1 is equal to the dominate wavelength λ_0 the attenuation due to scattering will be maximised [*Kawahara et al.*, 2009]. From this standpoint, the degree of heterogeneity of a medium is not an intrinsic property, but one defined by the scale of observation. The mean free path l^* which describes the average distance between scattering events is often expressed as a medium property, when in fact it is determined by both the material and the probing wavefield.

In seismology, the first study of this nominally incoherent portion of recorded waveforms was made by *Aki* [1969], who coined the term "coda" to describe the observed random nature of the tail end of recorded earthquakes. The observation that the amplitude of the coherent arrivals decreased with epicentral distance, while the coda energy remained invariant, was used as evidence of localised backscatter of the incident arrivals. Subsequent works have used coda-wave analysis to study

seismic sources and medium properties [*Rautian and Khalturin*, 1978; *Herrmann*, 1975], or as a tool to quantitatively estimate the strength of random heterogeneity within a region [*Aki and Chouet*, 1975; *Sato*, 1978]. The theoretical basis of these initial works can be separated into single scattering theory at one end [*Sato*, 1977a,b; *Kopnichev*, 1975, 1977a,b] valid for short propagation distances and lapse times, and the diffusive propagation [*Wesley*, 1965; *Aki and Chouet*, 1975] on the other. These theoretical descriptions of the coda-wave gave rise to several phenomenological parameters able to capture the statistical properties of disordered media, such as the total scattering coefficient $g_0 \equiv l^{*-1}$, which describes the scattering power per unit volume (see the grey box), or the S-coda attenuation Q_c^{-1}, measured from the coda amplitude decay rate. Later the seismic albedo B_0, was introduced [*Wu*, 1985], which is a measure of the ratio between scattering ${}^{Sc}Q^{-1}$, and total Q^{-1} attenuation respectively. Radiative transfer theory [*Chandrasekhar*, 1960], provides a link between these statistical descriptions of wave propagation, and the spatiotemporal fluctuations of energy density within random media, and has been developed further to better describe various phenomena of interest to the seismological community [*Wu*, 1985; *Sato*, 1994; *Wu and Aki*, 1988; *Shang and Gao*, 1988; *Zeng et al.*, 1991]. Many of the initial applications of radiative transfer apply the Monte Carlo method for acoustic and isotropic scattering [*Hoshiba*, 1991, 1994; *Yoshimoto*, 2000] and later with elastic mode conversions [*Sens-Schönfelder et al.*, 2009; *Yamamoto and Sato*, 2010].

So far, all of the mentioned coda-wave related field studies can be classified as concerned with the development of spatial maps of scattering properties. Some of the first temporal studies demonstrated the sensitivity of phenomenological parameters such as Q_c^{-1} to changes due to local earthquakes [*Gusev and Lemzikov*, 1985; *Jin and Aki*, 1986, 1989].

Another branch of coda related studies, not discussed until now are those concerned with the phase information within the coda. This by definition requires a temporal comparison of the coda-wave, first described by *Poupinet et al.* [1982] for micro-earthquake doublets around the San Andreas and Calaveras faults [*Poupinet et al.*, 1982] in the USA, and later within the Mt. Merapi volcano in Indonesia [*Ratdomopurbo and Poupinet*, 1995]. These seminal works mark the beginning of the concept by which a scattering medium is considered as an interferometer.

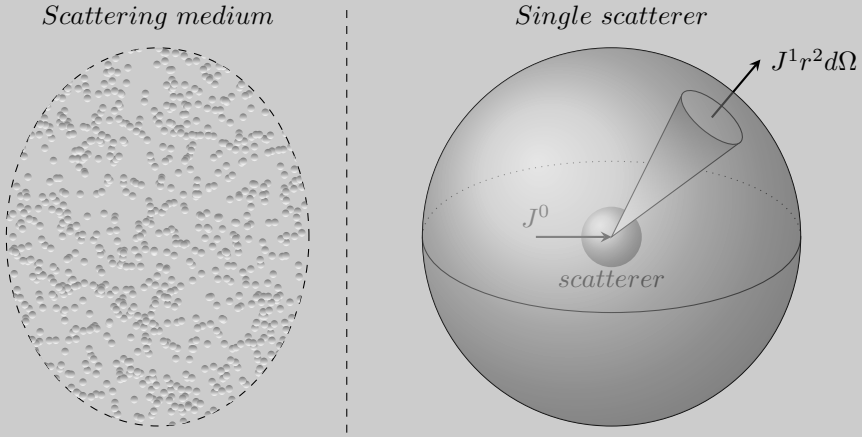

The total scattering coefficient g_0 represents the average scattering power per unit volume over all directions. The differential scattering cross-section is the ratio of scattered energy flux J^1 through a solid angle surface element $r^2 d\Omega$, to the incident energy flux J^0 as [*Sato et at., 2012*],

$$\frac{d\sigma}{d\Omega} = \frac{J^1 r^2}{J^0}. \tag{1.0.1}$$

By taking the integral over all directions ($d\Omega$ segments), g_0 can be defined as,

$$g_0 = \rho_n \oint \frac{d\sigma}{d\Omega} d\Omega = \rho_n \sigma_T \equiv l^{*-1}, \tag{1.0.2}$$

where l^* is the mean free path and ρ_n is the density of scatterers within the medium. For a plane wave of frequency ω, g_0 can then be related to the scattering attenuation ${}^{Sc}Q^{-1}$ as

$${}^{Sc}Q^{-1}(\omega) = \frac{g_0 V_0}{\omega}, \tag{1.0.3}$$

where V_0 is the background velocity of the medium.

1.1 The coda-wave as an interferometer

As a wave propagates beyond one l^*, it begins to lose memory of its incident direction, and therefore the ability to reconstruct an image of the host medium through geometrical considerations. By considering the medium as an interferometer, with this loss in spatial resolution [*Widess*, 1973], comes a gain in sensitivity to changes within the region sampled by the wavefield, making these methods well suited to monitoring applications. It is this concept which underpins the studies presented in this thesis. In the following section a review is given, covering the development and application of three methods which use interferometric principles. Each method considers at least one of the three quantities necessary to describe the evolution of energy density within a scattering medium. These are velocity V_0, and the scattering ${}^{Sc}Q^{-1}$, and intrinsic ${}^{I}Q^{-1}$ [*Yuehua Zeng*, 1991].

■ 1.1.1 Coda-Wave Interferometry

While the first indications that the scattered wavefield could be reliably used as an interferometer were made through direct application to seismological data [*Poupinet et al.*, 1982], the first to explicitly state this intention was *Snieder* [2002a]. The term Coda-Wave Interferometry (CWI) in the most general terms was introduced to describe the theoretical relationship between a homogeneous change within a scattering medium, as measured by a normalised cross-correlation between wavefields recorded in the unperturbed, and perturbed states. While a number of perturbation types are discussed in this seminal work, the most widely applied to date has been the relationship between a phase shift and a change in the relative velocity.

Subsequent geophysical applications have demonstrated the utility and sensitivity of CWI where micro-earthquake doublets enable velocity changes to be determined in the vicinity of active volcanoes [*Snieder and Hagerty*, 2004; *Snieder and Vrijlandt*, 2005; *Grêt*, 2005; *Pandolfi et al.*, 2006; *Martini et al.*, 2009]. Another more recent study demonstrated the temporal effect that large regional earthquakes can have on the velocity structure of volcanoes [*Battaglia et al.*, 2012]. A key requirement of CWI, is the availability of a repeatable source, a fact which has limited many of the initial field-scale applications to regions where impulsive earthquake doublets are found [*Poupinet et al.*, 2008]. One of the first examples where active-source, field-scale, monitoring was conducted is the study by *Wang et al.* [2008], in which changes in barometric pressure were related to velocity variations.

Due to the difficulties associated with active source field-scale studies, several groups have investigated the use of passive monitoring approaches, which make use of the ambient noise-field through seismic interferometry [*Campillo*, 2003; *Wapenaar*, 2004; *Shapiro et al.*, 2005], to retrieve the impulse response of the medium. The applicability of CWI through passive measurements has been demonstrated for volcanoes [*Snieder and Hagerty*, 2004; *Grêt*, 2005; *Sens-Schönfelder and Wegler*, 2006], the lunar subsurface [*Sens-Schönfelder and Larose*, 2008], around fault zones [*Wegler and Sens-Schönfelder*, 2007], and within mines [*Grêt et al.*, 2006a].

Another field of study within which CWI has gained considerable popularity is Non-Destructive Testing (NDT). It has been applied to measure thermal changes

within concrete [*Larose et al.*, 2006; *Wunderlich and Niederleithinger*, 2012], and metal [*Michaels and Michaels*, 2005], or to monitor stress changes due to both the acoustoelastic effect [*Larose and Hall*, 2009; *Stähler et al.*, 2011] and the formation of damage [*Shokouhi et al.*, 2010; *Zhang et al.*, 2011; *Schurr et al.*, 2011; *Zhang et al.*, 2012b; *Masera et al.*, 2011]. Due to many of the same concerns associated with the deployment of active source monitoring infrastructure within seismology, recent efforts have also been made in the NDT community to assess the feasibility of ambient noise applications, initially in the laboratory [*Hadziioannou et al.*, 2009], and more recently on a functioning highway bridge [*Hadziioannou et al.*, 2019]. For a detailed review of CWI in NDT, the reader is referred to *Planès and Larose* [2013].

In addition to the geophysical and NDT applications, initial steps have been made in the rock mechanics community, where CWI has been applied to better characterise laboratory samples exposed to perturbations in temperature, stress, and fluid saturation [*Grêt et al.*, 2006b; *Griffiths et al.*, 2018].

■ 1.1.2 Coda-Wave Decorrelation

The initial formulation of CWI was presented in terms of a homogeneous change in either scatterer location or material velocity, and therefore formulated without the intention of localising a change within the medium. Through the observation in the laboratory that correlation coefficients from different receivers display a spatial dependency, *Larose et al.* [2010] made the first steps in the development of what is referred to in this thesis as Coda-Wave Decorrelation (CWD). While the processing steps remain essentially the same as CWI, the authors present an expression for the theoretical decorrelation coefficient due to the formation of a localised defect, in terms of the total scattering cross-section σ_T. This is based on the approximation of a diffusive sensitivity kernel between source and receiver pairs, which evolves with increasing lapse time. For a receiver network, and a miss-fit function between the theoretical and measured decorrelation coefficients, the location of a single defect is determined in a probabilistic sense. A detailed description of the theoretical underpinnings of this method is given by *Rossetto et al.* [2011], while a least squares approach is proposed by *Planès et al.* [2015], which allows the simultaneous detection of multiple defects. To date, the geophysical applications of CWD inversion have been applied to monitor the structural changes associated with preeruptive and coeruptive changes in a volcano [*Obermann et al.*, 2013a], and due to the Mw 7.9 2008 Wenchuan earthquake [*Obermann et al.*, 2014, 2019]. In these studies ambient noise interferometry was applied to determine the impulse response of the region, from which CWD is applied.

In the NDT community several Structural Health Monitoring applications have been made, locating the formation of a single crack in a concrete bending test [*Larose et al.*, 2015], on a test bridge, and within an aeronautical wind tunnel [*Zhang et al.*, 2018].

The crucial component of CWD inversion, which enables the location of change to be determined are the sensitivity kernels. These encode an approximation of the evolution of wavefield intensity based on certain assumptions of the medium and its boundary conditions. Recently, efforts have been made to derive kernels which

include the coherent arrivals where the single scattering approximation is applicable [*Margerin et al.*, 2016; *Nakahara and Emoto*, 2017], or to include the influence of boundary conditions through numerical modelling of diffusive transport of energy [*Kanu and Snieder*, 2015; *Xue et al.*, 2019]. These steps represent an improvement in the robustness of the method, and can be expected to enable application to a greater range of problems.

1.2 Monitoring changes in intrinsic attenuation

So far we have discussed coda-wave derived monitoring methods for velocity V_0, and the scattering cross-section σ_T of the medium, as related to the scattering attenuation ${}^{Sc}Q^{-1}$. These represent two of the three quantities required to describe the evolution of energy density where both single and diffusive propagation is considered [*Yuehua Zeng*, 1991]. The final quantity which is required is the intrinsic attenuation ${}^{I}Q^{-1}$. The introduction of the "seismic albedo" B_0 by *Wu* [1985],

$$B_0 = \frac{{}^{Sc}Q^{-1}}{{}^{Sc}Q^{-1} + {}^{I}Q^{-1}} = \frac{{}^{Sc}Q^{-1}}{Q^{-1}}. \tag{1.2.1}$$

represented an important step in quantifying ${}^{I}Q^{-1}$. While various methods have been proposed to separate the components of Q^{-1} from measured data [*Aki*, 1980; *Frankel and Wennerberg*, 1987; *Jacobson*, 1987], the most commonly applied in seismology is Multiple Lapse-Time Window Analysis MLTWA. This method was introduced by *Fehler et al.* [1992] and uses the observation that energy density within different time windows of a scattered wavefield is influenced to varying degrees by g_0 and Q^{-1}. A Monte Carlo simulation [*Hoshiba*, 1991] is typically applied to simulate the scattering process, with comparisons to different radiative transfer theories [*Wu*, 1985; *Yuehua Zeng*, 1991]. Since its introduction, MLTWA has been applied to a number of tectonic areas [*Mayeda et al.*, 1992; *Hoshiba*, 1993; *Del Pezzo et al.*, 2011; *Akinci et al.*, 1995; *Pujades et al.*, 1997; *Akinci and Eyidoan*, 2000], with efforts made to consider non-uniform velocity and scattering coefficients [*Hoshiba*, 1995, 1997; *Hoshiba et al.*, 2001], and the layered nature of the earth [*Bianco et al.*, 2002, 2005]. It is important to note that the primary objective of all MLTWA studies to date, has been to establish a spatial map of the attenuative properties, and not to monitor their temporal evolution due to some perturbation.

1.3 Problem statement

The following problem statement is separated into two main areas of concern. Those related to the development of methods which improve the utility of the coda-wave monitoring within Early Warning Systems (EWS), and improving the understanding of changes in material properties through coda-wave monitoring.

By focusing on the diffuse wavefield, one sacrifices order or coherence for sensitivity. The point at which sensitivity is most valuable is where the timelines of

information is of utmost importance. Following this train of thought, one concludes that the application of coda-wave derived monitoring methods is likely to provide the greatest utility to problems of early warning detection. Some of the key requirements of such EWS are [*UN/ISDR: Global*, 2006]

- Simplicity; indicators must provide clear warning signatures which are well understood by the end-users.
- Robustness; able to withstand changes in environmental fluctuations and continuous drift.
- Automated data processing steps, and the triggering of alarms.

So far, due to the added complexity of deploying active source monitoring systems, the majority of the field scale examples of either environmental hazard or Structural Health Monitoring (SHM) have used the passive noise field as the source. This choice can be considered as a trade-off between robustness, automation and sensitivity, for simplicity as the associated instrumentation is greatly reduced.

- The robustness of the system is reduced, as any sudden large or long term drift in the characteristics of the noise will deteriorate the stability of the monitoring system.
- Automation due to the often manual steps required in the preprocessing of that noise field, in order to satisfy the assumption of an ambient random signature.
- One can expect a reduction in the obtainable sensitivity of passive noise-field correlations, in comparison to active source measurements. For passive seismic interferometry systems, the amplitude and frequency of the impulse response cannot be designed to meet the requirements of the system, and therefore the sensitivity of the system is defined by the characteristics of the available noise field.

Due to many of the concerns stated above, outside of academic research, coda-wave derived interferometry has yet to gain a foothold in operational EWSs.

On the other hand, one can consider Earthquake Early Warning (EEW) systems as trading reduced sensitivity, for improved simplicity, robustness, and automation. These systems do not attempt to determine any subtle precursory changes, but rather automate the detection of an actual earthquake [*Allen and Melgar*, 2019]. Depending on the epicentre location, these systems can provide vital seconds to tens of seconds warning of the arrival of damaging surface waves. While EEW systems serve a vital role in earthquake prone regions, their ability to provide a warning is inherently limited by both the epicentre to population centre distance, and the speed at which automation can deliver an alarm.

Before one can incorporate the sensitivity benefits of the coda-wave into EWS in general, the robustness and automation of processing must be addressed. It is suggested that one way to achieve this would be through the adoption of continuous, active source monitoring. This principle is exemplified by the San Andreas Fault Observatory at Depth (SAFOD) study by *Niu et al.* [2008], during which cross-borehole

active source monitoring determined approximately 10 h of pre-seismic phase shift within the coda before a magnitude 3 earthquake.

While coda-wave monitoring methods may present the greatest utility in early warning systems, there are many possible applications where the objective is simply to monitor the evolution of material properties. Within the field of experimental rock mechanics, the majority of the employed methods used to characterise a particular lithology only measure the bulk response of a sample at its boundaries. In order to address this issue, several laboratories over the past few decades have begun to implement geophysical methods to better characterise different lithologies. Aside from a few exceptions [*Griffiths et al.*, 2018; *Grêt et al.*, 2006a], the majority of these focus on the coherent first arrivals, and therefore do not exploit the sensitivity of the coda-wave. Furthermore, while there are several techniques which are able to resolve the heterogeneities of test samples, such as velocity tomography [*Jansen et al.*, 1993; *Brantut*, 2018; *Aben et al.*, 2019] or Acoustic Emissions monitoring [*Lockner*, 1993; *Lei et al.*, 2004; *Heap et al.*, 2009; *Sarout et al.*, 2017], the majority do not provide any spatial information.

1.4 Thesis objectives

The objective of this thesis is to work towards the improved utility of coda-derived monitoring, while advancing the phenomenological understanding of changes in material properties through the lens of the coda-wave. These objectives are realised through

- The development of robust continuous coda-wave derived monitoring systems. To extract key precursory indicators to the onset of inelastic material deformation. This is considered as an initial step, enabling the eventual automation in EWS. This objective is considered within chapter 2 of this thesis.
- Improving the characterisation of inelastic deformation within rock-mechanics testing, through the application of coda-wave derived monitoring methods. This objective is considered within chapter 3 and chapter 4 of this thesis.
- The demonstration of the spatial imaging capabilities of the coda-wave, during laboratory testing of samples tested under subsurface conditions. This objective is considered within chapter 4 of this thesis.

1.5 Thesis outline

This thesis begins in the first research chapter with a mostly methodological study into the robustness of coda-wave monitoring. This is combined in the second research chapter with a phenomenological study of the grain-scale compaction process. While the first two research chapters employ single source-receiver pairs, the final research chapter works to incorporate spatial information through the coda-wave monitoring of a medium with multiple source-receiver pairs.

In chapter 2, a single source-receive arrangement is applied, to monitor Unconfined Compressive Strength (UCS) tests on different laboratory core samples. Here the importance of maintaining sensitivity to the changes in material properties is highlighted by a comparison between a fixed and rolling-reference wavefield for both velocity (CWI) and scattering power (CWD). Through a rolling-reference arrangement, subtle precursory indicators are identified to the classically defined yield point of a material. Furthermore, the relative sensitivity of coda-wave methods is compared with the Time-Of Flight (TOF) of the wavefield. In terms of the stated research objectives, this chapter works to improve the robustness of coda-wave monitoring methods where either sudden large, or long-term transient material perturbations are expected.

In chapter 3, a study of samples from the seismogenic Groningen Gas Field under in-situ conditions is conducted. Here the three coda-wave based methods of CWI, CWD, and MLTWA are applied to monitoring velocity V_0, scattering power g_0, and intrinsic ${}^{I}Q^{-1}$/scattering ${}^{Sc}Q^{-1}$ attenuation respectively. Each sample is subjected to pore-pressure depletion at in-situ conditions over a period of days. Relative changes in each quantity are combined with micro-structural analysis, and the theory of acoustic wave propagation within saturated media to gain insight into the grain-scale compaction process. The implications of this work on both induced seismicity monitoring, and geomechanical modelling are discussed. In terms of the research objectives, this chapter works to advance the understanding of grain scale compaction within saturated porous media, with implications on the field-scale monitoring and modelling of induced seismicity.

In chapter 4, CWD inversion is applied to image the triaxial compressions of Whitby mudstone core samples, providing a 3-D time-lapse description of the evolution and redistribution of fracturing. Here, this active source method is compared with the sensitivity of the passive method of Acoustic Emissions (AE) monitoring for three samples of different initial water saturation. The implications of this research on both the understanding of inelastic strain localisation, and the possible benefits of the method for the rock mechanics community are discussed. In terms of the research objectives, this chapter demonstrates the capabilities of CWD in locating inelastic changes within a laboratory setup, with the sensitivity of the coda-wave.

In chapter 5 a summary of the major findings presented in this thesis is given. This is followed by several recommendations of possible directions for future research, to advance both the feasibility of coda-derived monitoring within early warning detection systems, and to improve the understanding of how specific changes in material properties can be extracted from the coda-wave.

2

Coda-wave monitoring of continuously evolving material properties and the precursory detection of yielding

Abstract The nominally incoherent coda of a scattered wavefield has been shown to be a remarkably sensitive quantitive monitoring tool. Its success is, however, often limited to applications where only moderate or localised changes in the scattering properties of the medium can be assumed. However, the compressional deformation of a relatively homogeneous rock matrix towards failure represents for a monitoring wavefield pronounced changes in both velocity and scattering power often due to a distribution of inelastic changes. A rolling reference wavefield is implemented when applying coda-wave interferometry (CWI) and coda-wave decorrelation (CWD), allowing relative velocity and material scattering power monitoring for such applications. It is demonstrated how this modification enables the qualitative monitoring of stages in material deformation common to unconfined compressive strength tests. In addition, the precursory/subtle onset of material yielding is identifiable in both the CWI and CWD methods, which was not possible when comparing to a fixed reference wavefield. It is, therefore, expected that this approach will enable these coda-based methods to robustly monitor continuous, destructive processes at a variety of scales. Possible applications include critical infrastructure, landslide, and reservoir compaction monitoring where both the subtle continuous and sudden large changes in a material's scattering properties occur.

Published as: Zotz-Wilson, R., Boerrigter, T., Barnhoorn, A., (2018),Coda-wave monitoring of continuously evolving material properties and the precursory detection of yielding, Journal of the Acoustical Society of America, 145,2,1060–1068.
Note that minor changes have been introduced to make the text consistent with the other chapters.

2.1 Introduction

With the advent of affordable sensor networks, along with the ability to transmit large amounts of data wirelessly, the feasibility of evermore complex monitoring systems is increasing rapidly [*Brownjohn*, 2007; *Stähli et al.*, 2015]. Whether it be critical infrastructure structural health monitoring (bridges, dams, nuclear reactors) or environmental hazards (earthquakes, landslides, induced seismicity) or early warning detection to dynamic failure, continuous non-intrusive monitoring is crucial.

Many works have demonstrated the remarkable sensitivity of the scattered wave to media-wide properties, through the estimation of velocity changes over fault zones [*Poupinet et al.*, 1984], in volcanoes [*Grêt*, 2005; *Matsumoto et al.*, 2001; *Ratdomopurbo and Poupinet*, 1995; *Sens-Schönfelder and Wegler*, 2006], landslides [*Mainsant et al.*, 2012], and within the lunar near surface [*Sens-Schönfelder and Larose*, 2008]. Various ultrasonic laboratory experiments have shown the coda's sensitivity to changes at the mesoscopic scale in terms of stress, temperature, and water saturation [*Grêt et al.*, 2006b; *Stähler et al.*, 2011; *Zhang et al.*, 2012b]. The coda-wave interferometry (CWI) formulation presented by *Snieder* [2002a] has served as the basis for many such relative time-lapse monitoring studies on solid media. In the field of optics diffusing wave spectroscopy (DWS)[*Pine et al.*, 1990] has been used to study different aspects of strongly scattered light, and was later extended to acoustics as diffusing acoustic wave spectroscopy (DAWS) [*Page et al.*, 2000] relating phase changes in a wavefield to, for example, monitor the average displacement of scatterers in a fluidised suspension.

In general, the recent research applying CWI has focused on exploiting the sensitivity benefits of the coda-wave in monitoring subtle, often cyclical, non-destructive processes and thereby inferring the average velocity change. To the authors' knowledge, the only studies which have applied CWI well into a region of inelastic deformation have been limited to concrete structures either partially [*Zhang et al.*, 2016] or fully under tensile forces [*Zhang et al.*, 2012b], of which only the latter shows the ability to track velocity changes close to the ultimate strength of the structure.

The method termed coda-wave decorrelation (CWD) as introduced by *Larose et al.* [2010] and later formalised by *Rossetto et al.* [2011] provides a spatiotemporal theoretical expression for the resulting decorrelation between a reference and perturbed wavefield due to the addition of a single or multiple localised scatterers [*Planès et al.*, 2015]. The ability of CWD to locate such a local change in scattering properties with the aid of a maximum likelihood inversion between the measured and theoretical decorrelation has been shown in a laboratory setting [*Larose et al.*, 2015, 2010], around an active volcano [*Obermann et al.*, 2013a] and most recently on a life-sized reinforced concrete structure [*Zhang et al.*, 2016]. The focus of this branch of coda-wave studies is on relating the decorrelation coefficient K between two wavefields to changes in material scattering properties. The most recent concrete structural health monitoring applications of CWD [*Larose et al.*, 2015; *Zhang et al.*, 2016] demonstrate its ability to identify the transition from elastic to inelastic deformation. However, there has been no published work that applies either CWI

or CWD on a rigid material throughout the elastic and inelastic deformation up until catastrophic failure. Furthermore, in both works macroscopic cracking is initiated under tensional bending where the stress field is localised, and, therefore, a more localised crack network results than would otherwise occur under a homogeneous tensional or compressional loading regime [*Paterson and Wong*, 2005]. While such localised changes are well suited to the LOCADIFF algorithm [*Larose et al.*, 2010; *Planès et al.*, 2013], where a more homogeneously distributed fracture network develops the resolution limit of the method will become an issue.

In this study we explore the practical application of these coda-wave focused monitoring methods on a rock matrix undergoing continuous changes in bulk scattering power and intrinsic velocity due to a homogeneous stress field with the goal of identifying defined stages of material deformation [*Heap and Faulkner*, 2008] and the precursory indication to material yielding. In particular, we show that for a fixed reference wavefield $u_u(t)$, monitoring the onset of elastic deformation due to compressional loading, both CWI and CWD monitoring experience a rapid decay in sensitivity. As a result, both are unable to identify the transition from elastic to inelastic deformation.

In order to overcome this, a rolling reference wavefield $u_{p_{j-N}}(t)$, lagging N measurements behind the most recently acquired j^{th} monitoring wavefield $u_{p_j}(t)$, is employed in a normalised cross-correlation formulation. With this simple modification, we show how one is able to identify three defined phases of material deformation common to laboratory unconfined compressive strength (UCS) tests. From this segmentation we are able to determine for two lithologies and three samples, precursory indicators to a material's yield point in both the CWI and CWD trends. It should be mentioned that while the idea of changing the reference has been applied before [*Grêt et al.*, 2006b; *Obermann et al.*, 2013a; *Snieder*, 2002b], and briefly discussed in a rolling formulation in the thesis of *Planès* [2013], its application to enable the continuous monitoring of a material's properties throughout deformation up until catastrophic failure remains unexplored.

2.2 Fixed-reference monitoring of destructive processes

■ 2.2.1 The theory of CWI for monitoring changes in velocity

The formulation of CWI as presented by *Snieder* [2002a] rests upon the understanding that a recorded wavefield $u_u(t)$which has interacted with an unperturbed scattering medium can be represented as the summation of all possible paths P through that medium as

$$u_u(t) = \sum_P A_p(t), \tag{2.2.1}$$

where A_p denotes the wave that propagates along path P. The first major assumption concerning the medium itself is that each individual scatterer has stationary properties, therefore, preventing a change in its scattering cross-section (size, shape, density, and velocity). Additionally, it is assumed that the mean free path l^*, which is indirectly related to the averaged distance between scatterers, is much greater

than the dominant wavelength λ_0.

A perturbed wavefield $u_p(t)$ that has experienced a subtle change $\delta << l^*$ in either the location of scatterers, the location of the source, or the background medium velocity, can then be represented as

$$u_p(t) = \sum_P A_p(t - \tau_P), \tag{2.2.2}$$

where τ_P represents the travel time change along path P . This formulation, therefore, implies that provided the perturbation does not change the dispersion of the wavefield; only a change in the arrival time of $u_u(t)$ will occur. The cross-correlation coefficient $CC(t_s)$ for a particular window of width $2t_w$ centered at time t_k within the coda, $(t_k - t_w)$ to $(t_k + t_w)$ is often presented as

$$CC(t_s) = \frac{\int_{t_k-t_w}^{t_k+t_w} u_u(t)u_p(t+t_s)dt}{\left[\int_{t_k-t_w}^{t_k+t_w} u_u^2(t)dt \int_{t_k-t_w}^{t_k+t_w} u_p^2(t)dt\right]^{1/2}}, \tag{2.2.3}$$

where $u_u(t)$ and $u_p(t)$ are the unperturbed and perturbed waveforms, respectively. This time shifted cross-correlation coefficient $CC(t_s)$ for a small window will reach a maximum when the average travel time perturbation $\langle\tau\rangle$ across all perturbed paths P is,

$$\langle\tau\rangle = t_s. \tag{2.2.4}$$

A homogeneous relative velocity perturbation can then be determined to a first order approximation by

$$\frac{\delta v}{v} = -\frac{\langle\tau\rangle}{t_k}. \tag{2.2.5}$$

If we now consider this in terms of a rock matrix, the first assumption of CWI implies that the size, width, and number of inhomogeneities (e.g., fractures, pores) remains constant in time. Furthermore, it requires that for a change in the phase to dominate the average distance between such inhomogeneities (the mean free path) is considerably larger than a wavelength. The constraint of a non-dispersive perturbation requires that changes in properties such as scattering or intrinsic attenuation are negligible. Provided only a subtle, cyclical, elastic deformation is applied to a medium with a sufficiently high source frequency, these assumptions generally hold within the time period between the perturbed and unperturbed wavefield. This is demonstrated for a rock matrix in the work by *Grêt et al.* [2006b], where CWI derived velocity changes are observed in a sandstone core sample due to a subtle elastic increase in uniaxial compressive stress.

■ 2.2.2 Applying a CWD approach to monitoring changes in scattering properties

In order to enable the coda-based monitoring of scenarios where inelastic material deformation occurs, one can focus on the maximum cross-correlation coefficient $CC(t_s)$ instead of the $t_s = \langle\tau\rangle$ at which its maximum is found. This is equivalent to

the CWD methods discussed earlier, though with the distinction that here the main goal is not to find a single [*Larose et al.*, 2010] or several localised scatterer perturbations [*Planès et al.*, 2015] within the medium but to monitor a global perturbation within the region sampled by the coda-wave.

The scattering power of a medium can be defined in terms of its total scattering coefficient g_0 [*Aki and Chouet*, 1975]. Assuming an idealised scattering medium as a random distribution of n point-like scatterers with number density ρ_n , within a background velocity V_0, and a propagating plane wave, this coefficient can be defined as [*Sato et al.*, 2012],

$$g_0 = \rho_n \sigma_T \equiv l^{*-1}, \tag{2.2.6}$$

which is inversely proportional to a material's mean free path l^*. By applying diffusive propagation theory, *Rossetto et al.* [2011] derived an expression for the theoretical decorrelation coefficient K^T caused by localised perturbation of the total scattering cross-section σ_T. This requires the knowledge of a sensitivity kernel $Q(\mathbf{s}, \mathbf{x_m}, \mathbf{r}, t)$ between a source $\mathbf{s}$ and receiver $\mathbf{r}$ for the perturbation location $\mathbf{x_m}$ and a time t within the coda. Re-writing this in terms of a change in a material's total scattering coefficient g_0 within a background velocity V_0, explicitly in terms of unperturbed and perturbed medium states gives,

$$K^T(\mathbf{X}, t) = \frac{V_0}{2} \int_{V_Q} |\Delta g_{0_{p-u}}(\mathbf{x})| Q(\mathbf{s}, \mathbf{x}, \mathbf{r}, t) dV_Q(\mathbf{x}), \tag{2.2.7}$$

where $\mathbf{X}$ defines the ensemble of n randomly distributed perturbation locations within the kernel volume V_Q, while $|\Delta g_{0_{p-u}}|$ locally defines the difference in total scattering coefficient between the perturbed (at time t_p) and unperturbed material states (at time t_u). Considering eq. (2.2.7) in terms of the evolution of a material's scattering properties, any change in the size or impedance contrast of the scatterers will increase in the decorrelation, as will the addition or removal of scatterers as the number density ρ_n changes. Furthermore, these changes will alter the intensity of the diffusive wavefield [*Paasschens*, 1997; *Pacheco and Snieder*, 2005] through the material's diffusion and attenuation coefficients, resulting in a change in the sensitivity kernel.

Equation 2.2.7 is, therefore, able to describe both a change in the number of scatterers, through ρ_n or in the size and impedance contrast of scatterers, through σ_T , provided one can assume the same sensitivity kernel $Q(\mathbf{s}, x, \mathbf{r}, t)$ in both states. For a large perturbation in g_0, it will become difficult to maintain this approximation as the diffusion and attenuation coefficients between the two medium states begin to diverge. In terms of the measured data, the decorrelation coefficient $(K(t_s) = 1 - CC(t_s))$ between two recorded time-series will approach one, at which point it will only represent a spurious correlation between two time-series. However, provided that a weak perturbation can be ensured in the time interval $t_u - t_p$, the measured $K(t_s)$ can be related to the modulus of the change in a material's scattering coefficient weighted by the sensitivity kernel.

2.3 Rolling-reference coda monitoring of destructive processes

To ensure the assumptions of CWI and CWD are satisfied throughout the long term monitoring of continuously evolving material scattering properties, we propose the use of a rolling reference waveform when determining both the decorrelation coefficient and the relative velocity change. While the idea of manually selecting a different reference wavefield during monitoring is not new [*Grêt et al.*, 2006b; *Obermann et al.*, 2013b], the uses of a rolling reference wavefield enabling the continuous monitoring of a material throughout deformation up until catastrophic failure remains unexplored. Concerning eq. (3.2.1), such a modification requires the fixed reference wavefield $u_u(t)$ to be replaced by a rolling reference wavefield $u_{p_{j-N}}(t)$, in a monitoring sense lagging behind the most recently acquired wavefield $u_{p_j}(t)$ by N measurements. In terms of the decorrelation coefficient,

$$K^{Roll}(t_s) = 1 - \frac{\int_{t_k-t_w}^{t_k+t_w} u_{p_{j-N}}(t) u_{p_j}(t+t_s) dt}{\left[\int_{t_k-t_w}^{t_k+t_w} u^2_{p_{j-N}}(t) dt \int_{t_k-t_w}^{t_k+t_w} u^2_{p_j}(t) dt\right]^{1/2}}. \tag{2.3.1}$$

Provided the repeat measurement period dt_{p_j-N}, at which each $u_{p_j}(t)$ wavefield is recorded is much smaller than the rate of change in the scattering coefficient dg_0/dt_{p_j-N}, this formulation provides the flexibility of selecting a sufficiently small reference lag N such that each correlation is able to better satisfy the assumptions of CWI and CWD. In terms of eq. (2.2.7), for a small dt_{p_j-N} the measured K^{Roll} and the associated t_s provides a qualitative description of the rate-of-change ($\dot{g_0} = dg_{0_{p_j-p_N}}/dt_{p_j-N}$) in g_0 and dv/v, respectively, throughout the monitoring period.

2.4 Experimental setup

In order to experimentally analyse and compare the attributes of fixed and rolling reference forms of CWI and CWD for continuously evolving scattering properties, acoustic monitoring of UCS tests on laboratory scale core samples is made, fig. 2.1. For redundancy, one axial and two radially-mounted transducers acting as receivers-RX, and one axially mounted source-TX transducer are attached to the surface of a core sample. Transducers with a peak operating frequency of 1 or 2.25 MHz are used depending on the experiment. To reduce the presence of noise, the stacking of 512 individual wavelets is made, resulting in a repeat measurement period dt_{p_j-N} of 15 s. An axially increasing force F is applied to each core sample controlled by a constant axial strain rate ($\Delta L/Ldt$) between 1.32 - $4 \times 10^{-6}\,\mathrm{s}^{-1}$. The applied force F and total axial displacement are recorded every half second throughout monitoring up until the sample experiences dynamic failure. The lithologies tested are Bentheimer sandstone [*Peksa et al.*, 2015] which has well-sorted grain sizes (180-320 µm) and high porosity (21-27 %) and a poorly sorted (30-800 µm), zero primary porosity granite sourced from Benin. A summary of the three core sample UCS experiments is provided in table 2.1 along with the abbreviated sample names employed in this work.

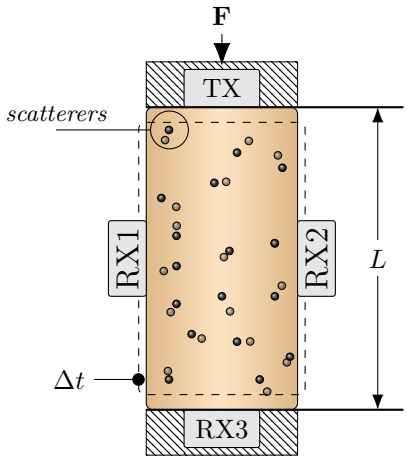

Figure 2.1: *Schematic representation of the UCS core test setup with active acoustic monitoring. An axially mounted* MHz *source (TX) with one axial and two radial receivers (RX) monitoring the changes in scattering properties every* Δt *for increasing load* F *and axial deformation* ΔL*.*

Table 2.1: *Summary of the UCS tests core sample Length and Diameter, lithology, strain rate, and acoustic source frequency.*

	L/D $[mm]$	Lithology	$\Delta L/Ldt$ $[\mathrm{s}^{-1}]$	Src. [MHz]
BNT1	75.01/39.75	Bentheimer sandstone	4.0×10^{-6}	1.0
BNT2	75.11/30.00	Bentheimer sandstone	4.0×10^{-6}	1.0
GRA	75.70/29.80	Benin granite	1.3×10^{-6}	2.25

2.5 CWI and CWD monitoring of an UCS test

Monitoring the evolution of a rock matrix towards dynamic failure with a wavelet at the mesoscopic scale [*Li et al.*, 1998; *Heap and Faulkner*, 2008; *Barnhoorn et al.*, 2010, 2018], is characterised by the continuous evolution of its wavefield propagation properties. For an Unconfined Compressive Strength test this can be illustrated by considering the different stages of material deformation as shown in fig. 2.2 for the BNT1 core sample. Firstly, the initial closure of any existing fractures or pore-space occurs. This is followed by the elastic deformation where a linear stiffening of the rock matrix is expected. These first two stages represent in terms of eq. (2.2.6) a general reduction in the total scattering cross-section σ_T and therefore g_0 of the medium, as the size and then impedance contrast of the fractures reduces. Finally, the onset of inelastic deformation marks the beginning of fracture growth/formation often termed the Fracture Initiation and Growth Threshold (FIGT). The growth and addition of new fractures represents an irreversible increase in σ_T and number den-

sity of fractures ρ_n respectively. Considering these changes in material scattering properties over a typical UCS test, it becomes difficult to make the assumption of a phase dominated or weak change in g_0 necessary in order to apply either CWI or CWD. Focusing first on the Coda-Wave Decorrelation method, in fig. 2.2 we compare the sensitivity of a fixed K^{Fix} versus a rolling K^{Roll} reference decorrelation coefficient to the stages of material deformation common to UCS tests. The K^{Fix}

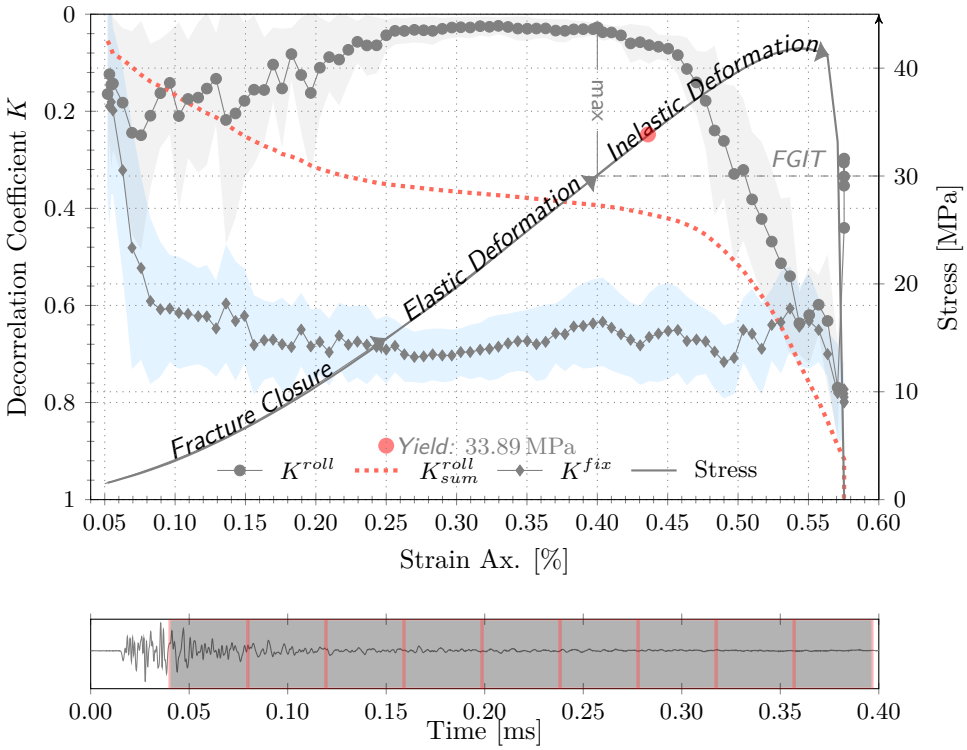

Figure 2.2: *CWD monitoring (receiver 2) of BNT1. The mean fixed reference decorrelation coefficient K^{Fix} is compared with the rolling reference equivalent K^{Roll} and its cumulative sum K^{Roll}_{sum}, calculated from 9 independent correlation windows. The K^{Roll} trend is generated with a rolling lag equal to the repeat measurement period of* 15 s *(i.e. $N = 1$). The shaded area represents the standard deviation about the mean decorrelation as calculated from the* 0.4 ms *correlation windows shown over a single waveform.*

coefficient shows a rapid increase over the first 0.025 % of axial strain, following by a more gradual slope towards 0.7 at the onset of elastic deformation. For the remainder of the USC test K^{Fix} shows little sensitivity to the ongoing deformation, with only a pronounced increase as dynamic failure occuring at 0.56 % axial strain.

This indicates initial fracture closure represents a large perturbation in g_0, though after this point K^{Fix} provides little informative value other then the knowledge that some notable change occurred early on during the monitoring period. In comparison, K^{Roll} which is related to the relative rate of change in g_0 as described by eq. (2.3.1) shows clearly identifiable trends segmenting each of the defined regions of deformation.

- The initial 0.025 % of axial strain results in an increase in the rate of change of decorrelation K^{Roll}. This indicates an acceleration in dg_0/dt (i.e. the curvature or second derivative $|\ddot{g_0}| > 0$) and therefore the rate of fracture closure.

- This is followed by a gradual reduction in K^{Roll} where $|\ddot{g_0}| > 0$, indicating a reducing rate of fracture closure as the rock matrix stiffens leading up to the beginning of elastic deformation.

- The elastic deformation of the material is characterised by a constant, low K^{Roll} and therefore $\dot{g_0}$, where $|\ddot{g_0}| = 0$. Here a unit stiffening of the rock matrix results in a proportional change in g_0 .

- At the Fracture Initiation and Growth Threshold - FIGT inelastic deformation occurs, which results in an increase in g_0, where $\dot{g_0}$ and $|\ddot{g_0}| > 0$. These changes are reflected by initially a gradual and then steep increase in K^{Roll} all the way until dynamic failure. This initial gradual increase is possibly evidence of the sub inelastic region of stable fracture growth before unstable growth continues, noted in literature for crystalline and brittle rocks [*Bieniawski*, 1967].

In order to make a direct comparison with K^{Fix} the scaled $(0-1)$ average cumulative summation of each correlation windows decorrelation coefficient (K^{Roll}_{sum}) is also provided. A general agreement is evident between K^{Fix} and K^{Roll}_{sum} as both show an initial increase, stabilisation, and then final increase within the region of elastic deformation, however the latter clearly shows an improvement in its sensitivity to the underlying perturbations. Most notably, K^{Roll}_{sum} reflects the linear region of elastic deformation as the applied constant strain rate results in a linear stiffening of the medium (i.e. a change in σ_T) and the transition to the non-linear region of elastic fracturing. The smoothed appearance of K^{Roll}_{sum} is a result of its calculation from the average of each independent correlation windows cumulatively summed decorrelation coefficient. In making a similar comparison for Coda-Wave Interferometry monitoring of the BNT1 dataset, the differences in sensitivity between the fixed and rolling reference relative velocity changes as determined by eq. (3.2.2) are compared, see fig. 2.3. The fixed reference $[\delta v/v]^{fix}$ shows an initial coherent increase in velocity in line with the Time Of Flight changes $[\delta v/v]^{TOF}$ derived from the first arrivals, though after only the first 0.12 % of axial strain its trend appears incoherent. In contrast, the rolling reference derived cumulative summation $[\delta v/v]^{roll}_{sum}$ curve tracks the $[\delta v/v]_{TOF}$ curve plateauing over the elastic region, before decaying with increasing inelastic deformation. A maximum in $[\delta v/v]^{roll}_{sum}$ occurs at 22.8 MPa whereas the $[\delta v/v]_{TOF}$ maximum occurs at 35 MPa. The initial increase in relative

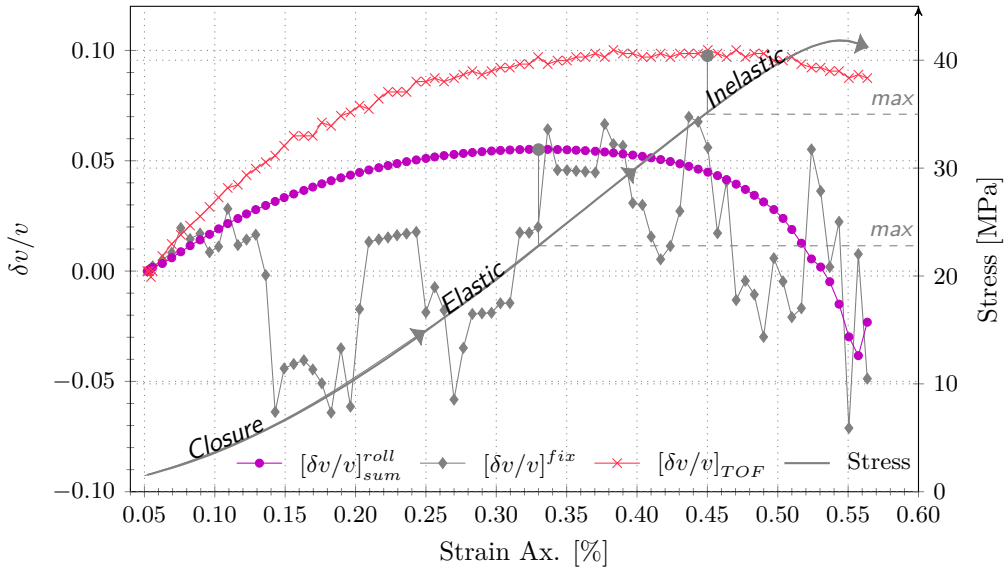

Figure 2.3: *CWI monitoring (receiver RX2) of the BNT1 dataset. The mean fixed reference* $[\delta v/v]^{fix}$ *relative velocity change is compared with the equivalent mean rolling reference cumulative summation* $[\delta v/v]^{roll}_{sum}$ *(max:* 28.9 MPa*) for the 9 windows shown in fig. 2.2. For comparison the Time Of Flight derived* $[\delta v/v]_{TOF}$ *(max:* 35 MPa*) is provided.*

velocity is explained by acoustoelastic theory, while any subsequent reduction in velocity occurs due to the formation of the first micro-cracks [*Selleck et al.*, 1998; *Shah and Hirose*, 2010]. The earlier reduction in $[\delta v/v]^{roll}_{sum}$ indicates the expected improvement in sensitivity of CWI to these inelastic changes [*Zhang et al.*, 2012b]. The presented $[\delta v/v]^{roll}_{sum}$ is the average relative velocity change determined from each of the 9 correlation windows show in fig. 2.2, and for the purpose of this study is only considered as a qualitative indicator of the materials velocity change.

In summary, when applying CWD the three stages of material deformation from initial fracture closure, elastic deformation, and fracture growth are all reflected in the K^{Roll} and K^{Roll}_{sum} trend lines, whereas it is difficult to find any clear segmentation in the K^{Fix} curve. The application of a rolling reference CWI derived $[\delta v/v]^{roll}_{sum}$, while not able to clearly segment each region of deformation does track the Time Of Flight derived changes with improved sensitivity to the onset of inelastic deformation, whereas the fixed reference $[\delta v/v]$ does not.

2.6 Precursory identification of material yielding

Based on the presented ability of both K^{Roll} and $[\delta v/v]^{roll}_{sum}$ to monitor deformation of a rock matrix, we will now assess both methods sensitivity to the onset of inelastic

deformation. The yield point of a material is often defined as the transition from predominantly stable fracture growth to predominantly unstable fracture growth [*Bieniawski*, 1967; *Mogi*, 2007], while others define it as the point the first micro-fractures are formed [*Elliott and Brown*, 1986; *Paterson and Wong*, 2005]. There is however, general consensus that the yield point can be identified on a stress/strain diagram as the onset of non-linear behaviour which follows a linear elastic region. This parameter is of critical importance in the prediction of dynamic material failure as it signifies that permanent material deformation has begun. Typically, the yield point from a UCS test would be determined by hand, though in order to remove some of the ambiguity surrounding this, an automated search is made based on the method described in appendix A.1. On the basis of this yield point, the precursory/subtle detection capabilities of the CWD and CWI methods can be assessed.

For this purpose two additional UCS tests are made, on a repeat Bentheimer (fig. 2.4 - BNT2) and Benin granite (fig. 2.5 - GRA) core sample. As with BNT1, the indication of inelastic deformation (FIGT) is identified at the end of the trough in K^{Roll} as the rate of change in g_0 increases. Similarly, the coda and $[\delta v/v]_{TOF}$ inelastic indicators are identified at the onset of a reduction in velocity as the acoustoelastic effect [*Toupin and Bernstein*, 1961] working to increase the velocity is overcome by the formation of the first micro-fractures [*Zhang et al.*, 2012b]. In order to make a comparison between the different lithologies and datasets, each precursory indicator is quoted in terms of the percentage of the yield stress at which it is found, as presented in fig. 2.6.

For the Bentheimer sandstone samples (BNT1 and 2) the CWI cumulative relative velocity changes $[\delta v/v]^{roll}_{sum}$ indicate the onset of yielding at around 70 % of the yield stress, where the CWD decorrelation coefficient K^{Roll} begins to increase at around 86 % of the yield stress. The GRA sample on the other-hand show K^{Roll} as providing the earliest indication of inelastic deformation at 66 % in comparison to $[\delta v/v]^{roll}_{sum}$ at 89 % of yield stress. This may be a result of the differences in fracturing behaviour between the well sorted quartz-rich, porous grains of the Bentheimer sandstone and the poorly sorted non-porous grains of the Benin granite resulting in reduced sensitivity of the velocity change at the onset of fracturing.

In all cases, the reference $[\delta v/v]_{TOF}$ show no precursory indicative power to material yielding with the onset of decay occurring after the stress-strain identified yield point. The lack of sensitivity of Time-Of-Flight changes to the classically defined yield point which was also noted in the work by *Barnhoorn et al.* [2018]. Refer to the appendix A.1 for a description of the method applied to determine the yield point.

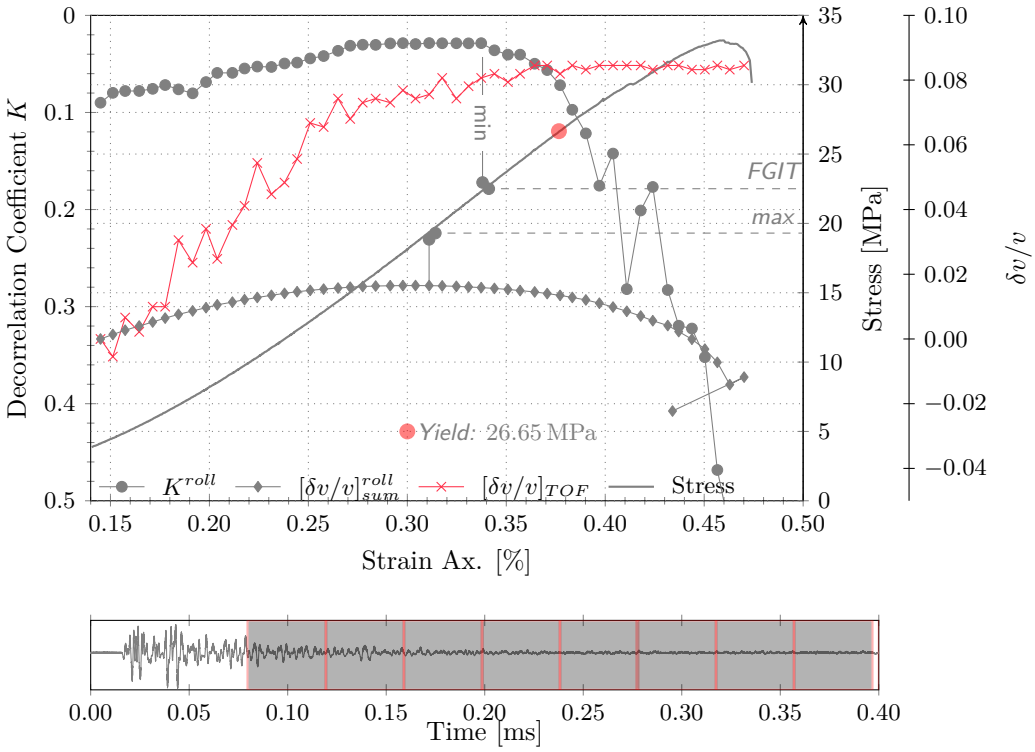

Figure 2.4: *CWD and CWI monitoring of BNT2. The K^{Roll} (FGIT:* 22.5 MPa*) and $[\delta v/v]^{roll}_{sum}$ (max:* 19.3 MPa*) trends are generated with a rolling lag equal to the repeat measurement period of* 15 s *(i.e. $N = 1$), calculated from the average of the 8 independent* 0.04 ms *correlation windows. For comparison the Time Of Flight derived $[\delta v/v]_{TOF}$ (max:* 34 MPa*) is provided.*

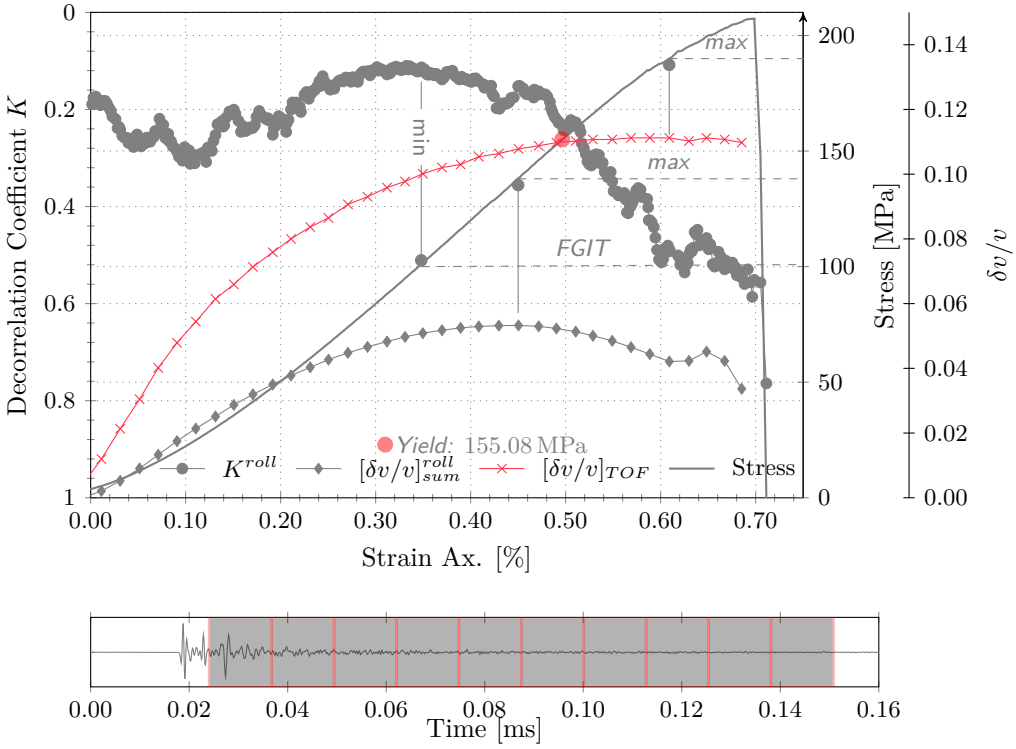

Figure 2.5: *CWD and CWI monitoring of GRA. The K^{Roll} (FGIT:* 101 MPa*) trend is generated with a repeat measurement period of* 150 s *($N = 10$) from the average of the 10 independent,* 0.013 ms *correlation windows shown. The $[\delta v/v]^{roll}_{sum}$ (max:* 138 MPa*) cumulative summation is made for $N = 1$. For comparison the Time Of Flight derived $[\delta v/v]_{TOF}$ (max:* 190 MPa*) is provided.*

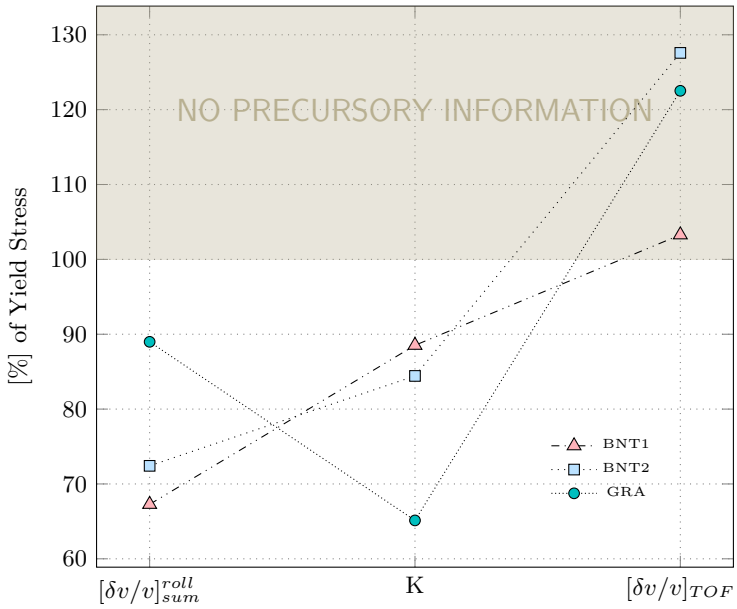

Figure 2.6: *Comparison of the precursory indicators to the yield stress, determined from the rolling reference integrated relative velocity changes* $[\delta v/v]^{roll}_{sum}$*, the rolling reference decorrelation coefficient* K^{Roll}*, and the TOF derived relative velocity changes* $[\delta v/v]_{TOF}$*.*

2.7 Discussion and conclusions

In this study, we have shown that by applying a rolling reference waveform in both the CWI and CWD form, one is able to monitor the evolution of a material's relative velocity change and scattering coefficient where a large inelastic perturbation in its scattering properties occurs. Furthermore, we demonstrate that both approaches provide precursory indication of material yielding as determined from stress-strain measurements. While these benefits have direct applications in terms of providing a better understanding of rock properties in the laboratory, it is expected that such a processing approach will enable a wider range of field scale monitoring applications.

In the structural concrete bending tests by *Zhang et al.* [2016] which applied fixed reference CWI and CWD and the work by *Larose et al.* [2015] where only CWD was applied the authors noted the increase in error of both relative velocity and the decorrelation coefficient as inelastic deformation progressed. While this can be easily overcome by the manual selection of a new reference point during monitoring, we suggest that where the long term, continuously monitoring of both gradual, and sudden inelastic changes is required a rolling reference is the preferred choice. In terms of structural applications, this allows for the gradual long term monitoring of micro-cracking which occur throughout the life of concrete while maintaining sensitivity as an early warning to material failure. Furthermore, to the authors knowledge all applications of CWD where notable inelastic deformation occurs have been under a bending force resulting in localised micro-cracks [*Paterson and Wong*, 2005] where nucleation occurs within a region of tensile stress. As supported by the current study where a homogenous compressional stress field is applied, the issue of rapid decorrelation is likely to become more immediately evident where a more homogeneously distributed fracture network forms.

An active source landslide or rockslide is an example of a near surface environmental geophysics application, where long term monitoring for the purpose of early warning detection to dynamic failure is required. Passive monitoring has been shown to be sensitive to a continuous velocity change, prior to a fluid slippage event [*Mainsant et al.*, 2012], where a rapid reduction in rigidity within a liquefaction region was identified as the mechanism for initial dislocation.

Pore-pressure driven reservoir compaction is a process which is by definition controlled at the grain scale [*Hol et al.*, 2015] with the first large scale induced seismicity events often along existing faults occurring decades after the beginning of production [*Bourne et al.*, 2014; *Van Thienen-Visser and Breunese*, 2015]. An in borehole active source continuous monitoring setup [*Zoback et al.*, 2011], will perhaps be able to identify both the gradual inelastic intergranular compaction [*Pijnenburg et al.*, 2018] as well as the onset of larger scale transgranular cracking which results in surface subsidence [*Pratt and Johnson*, 1926; *Sharp and Hill*, 1995; *Pijpers and Van der Laan*, 2016]. Where long term continuous monitoring is required it is expected that rolling reference processing will help fulfill some of the criteria for Early Warning System [*Stähli et al.*, 2015; *Michoud et al.*, 2013; *UN/ISDR: Global*, 2006], particularly in terms of the robustness, and autonomy of the system.

In the context of this study, the ability to determine the subtle onset of material

yielding was possible with only the knowledge that loading occurs at a constant strain rate, and in the absence of direct stress and strain measurements. Provided the employed source produces wavelengths sensitive to the perturbations in scattering, sensitivity to the mentioned structural-health, landslide, and compaction related monitoring is expected. While the feasibility of such applications requires additional investigation they can all be generalised as monitoring scenarios where both high rate-of-change and long-term transient changes in material scattering properties are of concern. It is therefore suggested that with an approximate knowledge of the underlying direction and type of perturbation, rolling reference coda based monitoring can be a useful addition to the mentioned Early Warning Systems as well as the long term monitoring of a materials scattering properties.

acknowledgments

We would like to thank Christian Reinicke, Cornelis Weemstra, Deyan Draganov, Kees Wapenaar, Lisanne Douma and Richard Bakker for their fruitful discussion throughout this work. Furthermore, the comments made by two anonymous reviewers helped to improve the brevity, clarity and completeness of the work. A special thanks goes to the laboratory support staff at TUDelft, and specifically Karel Heller for his assistance in setting up an automated ultrasonic acquisition system for our experimental work. The recorded data used in this study can be found at https://data.4tu.nl under DOI uuid:e3071a50-7310-4609-95a1-6f8e69e556e2.

3

Coda-Wave based monitoring of pore-pressure depletion-driven compaction of Slochteren Sandstone samples from the Groningen gas field

Abstract Pore-pressure depletion in sandstone reservoirs is well known to cause both elastic and inelastic compaction, often resulting in notable surface subsidence and induced seismicity. Recent studies indicate that in such cases inelastic strain, which is often neglected in geomechanical models, represents a significant proportion of the total strain throughout reservoir production. While there has been considerable effort to quantify the proportion of continuous inelastic deformation from the mechanical response of laboratory samples, there has been little focus to date on the associated acoustic response throughout compaction. With this in mind, we employ three coda-wave based processing methods for the active source monitoring of ultrasonic velocity, scattering power, and intrinsic/scattering attenuation during the pore-pressure depletion of core samples from the Slochteren sandstone reservoir in the Groningen gas field (the Netherlands). Our results corroborate previous studies suggesting that initially, inelastic deformation occurs primarily along intergranular boundaries, with intergranular cracking developing towards the end of depletion and particularly for the highest porosity samples. Furthermore, analysis of Biot-type intrinsic attenuation indicates that this compaction occurs in several stages of predominately intergranular closure, transitioning into primarily intergranular slip/cracking, and eventually porosity-dependent intragranular cracking.

Submitted: Zotz-Wilson, R., Filippidou, N., Van Der Linden, A. ,Verberne, B. A., Barnhoorn, A.,(2019), Coda-Wave Based Monitoring of Pore-Pressure Depletion-driven Compaction of Slochteren Sandstone Samples from the Groningen Gas Field, Under Review - Journal of Geophysical Research - Solid Earth.

Note that minor changes have been introduced to make the text consistent with the other chapters.

We demonstrate how this segmentation of pore-pressure driven compaction can be used to characterise differences in sample properties, and monitor the evolution of microstructural inelastic deformation throughout depletion. We further discuss the feasibility of in/cross-borehole monitoring of reservoir compaction, for both improved geo-mechanical modelling and early warning detection of induced seismicity.

3.1 Introduction

The continued production and resulting pore-pressure (PP) depletion of in-situ reservoir fluid from sandstone reservoirs often results in induced seismicity [*David et al.*, 2012; *Grasso*, 1992; *Segall and Fitzgerald*, 1998; *Suckale*, 2009; *Van Eijs et al.*, 2006], and field wide surface subsidence [*Pratt and Johnson*, 1926; *Sharp and Hill*, 1995; *Fialko and Simons*, 2000; *Morton et al.*, 2006; *Van Wees et al.*, 2014]. The driver for both the observable surface movement and induced seismicity is the increase in effective stress [*Zoback*, 2007]. The Groningen gas field located in the NE Netherlands has experienced several large seismic events since the beginning of production in 1963, resulting in damage to buildings and infrastructure [*Van Thienen-Visser and Breunese*, 2015], as well as notable surface subsidence [*Van Thienen-Visser and Fokker*, 2017]. Since the early 1970s, the primary measurement tool for reservoir compaction has been the monitoring of in-borehole radioactive depth markers [*Mobach and Gussinklo*, 1994]. This method is sensitive only to near borehole compaction, and requires repeat logging surveys over the reservoir, currently repeated every 5 years [*Doornhof et al.*, 2006]. Recently, an attempt was made to improve the timeliness of such in-borehole compaction data with the trial of Distributed Strain Sensing (DSS) technology [*Cannon and Kole*, 2017], enabling continuous monitoring of compaction. While the system represents an improvement in sensitivity, timeliness, and coverage if eventually deployed field-wide, it remains a near-borehole measurement.

Surface subsidence data in Groningen, resulting from both reservoir and overburden compaction, is acquired from optical levelling and Permanent Scatterer Interferometric Synthetic Aperture Radar (PS-InSAR). In comparison to optical levelling which requires successive field campaigns, PS-InSAR represents improved timeliness and spatial coverage of surface subsidence data [*Doornhof et al.*, 2006], though it is still limited by the density of Permanent Scatterers. Considering the current state of both subsidence and reservoir compaction monitoring, the available data represents insufficient timeliness and coverage to be used as an early warning system to induced seismicity [*UN/ISDR: Global*, 2006]. Alternatively, both the compaction and surface subsidence measurements as detailed above are used as input to reservoir compaction models [*Mossop*, 2012; *Den Haan*, 1994; *De Waal*, 1986]. In combination with history matching with production flow rates and pressure data, such models are developed to provide both a spatial estimate of future compaction and the associated uncertainty [*Van Thienen-Visser and Fokker*, 2017]. Within such models, laboratory experiments conducted at in-situ conditions simulating the reservoir provide a crucial data source to better constrain the modelling [*De Waal*, 1986; *Pruiksma et al.*, 2015]. Recent experiments by Hol et al. (2018) and Pijnenburg et al. (2018, 2019) demonstrate the important role of inelastic deformation occurring at low strains, during compaction of Slochteren sandstone recovered from the Groningen field. As pointed out by Pijnenburg et al. (2019), the often ignored inelastic component of compaction at low strains may play a major role in geomechanical models describing reservoir compaction, induced subsidence and seismicity [*Mulders*, 2003; *Van Eijs et al.*, 2006; *Bourne et al.*, 2014; *Lele et al.*, 2016; *Wass-*

ing, 2015; *Dempsey and Suckale*, 2017; *Zbinden et al.*, 2017] . However, the issue of upscaling, i.e., how best to extrapolate laboratory scale results to field-scale models, remains [*Spiers et al.*, 2017].

In an effort to improve both the understanding of low strain compaction, and how best to extrapolate from the grain scale, we employ three active source coda-wave based geophysical monitoring methods to Slochteren sandstone well-bore core samples, subjected to pore-pressure depletion. The methods applied are Coda-Wave Interferometry - CWI for velocity, Coda-Wave Decorrelation - CWD for scattering power, and Multi-Lapse Time Window Analysis - MLTWA for attenuation monitoring. Each method is applied throughout both continuous and multi-cycle Uniaxial Pore Pressure Depletion (UPPD) protocols [*Dudley et al.*, 2016], from the pre-production value of 35 MPa down to 3 MPa. The capabilities of each method in informing on the process of reservoir compaction, as controlled at the grain boundary by intergranular re-arrangement [*Bernabé et al.*, 1994; *Menéndez et al.*, 1996; *Pijnenburg et al.*, 2018] or intragranular/transgranular cracking [*Brantut et al.*, 2013; *Baud et al.*, 2004; *Heap et al.*, 2009, 2015; *Brantut et al.*, 2013] are discussed. Our results not only corroborate the conclusions of *Hol et al.* [2018a]; *Pijnenburg et al.* [2018, 2019], that inelastic strain in the Slochteren sandstone occurs in the early stages of depletion, but imply that compaction represents a serial process which may be segmented into stages of predominantly intergranular closure followed by predominantly intergranular slip/ intragranular cracking. We summarize these findings using a new conceptual model for the grain scale mechanisms controlling compaction, and discuss the geomechanical implications of our work, including for field-based monitoring of reservoir compaction using the coda-wave.

3.2 Materials and methods

■ 3.2.1 Slochteren sandstone samples and characterisation

The Slochteren sandstone within the Groningen gas field in the Netherlands lies at approximately 3 km depth and has a thickness of 100 to 200 m. As a result of the nearly 55 years of production, the pore pressure has decreased from 35 MPa to ∼8 MPa [*NAM*, 2013, 2016a], with the gas water contact within the field ranging from 50 to 150 m from the top of the reservoir [*NAM*, 2013]. In July 2015, ∼200 m of 3.5 inch (89 mm) diameter core was extracted from the ZRP-3a test well, located in the centre of the Groningen gas field, which included sections of underburden, reservoir, and caprock. At the time of coring, the reservoir pressure was approximately 10 MPa [*van Eijs*, 2015]. With the aid of computerised X-ray tomography suitable samples were selected at random intervals within a True Vertical Depth (TVD) range of 3530 to 3667 m. In the present study we analyse core samples from a subset of this range between TVD 3632.94 and 3562.08 m, and porosity between 19.2 and 29.6 %, which is representative of the average values in the centre of the reservoir between 18 and 22 % [*NAM*, 2016b].

A total of four separate core series (123, 134, 133 and 137) are tested, from which three to five plugs of length/diameter 2/1 inch (50/25 mm) or 3/1.5 inch (76/38 mm)

Table 3.1: *Summary of the Pore-Pressure Depletion test samples and experimental parameters.*

	Depl. rate MPa h^{-1}	Length [mm]	Diameter [mm]	Type
123AV	0.6	50.2	24.8	UPPD-MC3
123BV	0.6	50.3	24.8	UPPD-MC2
123DV	0.6	50.1	24.7	UPPD-MC3 AE
133BV	2.5	74.5	37.5	UPPD
137AV	0.6	75.8	38.0	UPPD-MC3
137BV	0.6	75.7	37.9	UPPD
134BV	0.6	75.8	37.33	UPPD

The depletion rate in MPa h^{-1} refers to the effective depletion rate from beginning to the end of the experiment, while the instantaneous depletion rate of 2.5 MPa h^{-1} is the same for all UPPD-MC tests. Type defines the experimental protocol undertaken, either Uniaxial strain Pore-Pressure Depletion UPPD or the UPPD-Multi Cycle protocol for 1, 2, or 3 stages of cyclical loading. The type AE defines Acoustic Emissions testing where no active source data was acquired.

(labeled A,B,...,E) are extracted parallel ('V') to the core axis, see table 3.1. Visual inspection of all plugs showed that they are microstructurally relatively homogeneous on the mm- to cm-scales. To avoid any geochemical changes a synthetic brine matching the *in-situ* pore-fluid was used during both storage and the subsequent depletion experiments. One plug from each series was used to measure sample porosity by immersion (Hg, Chloroform), and permeability to N_2 at a constant confining pressure of 2.75 MPa. The remaining core material from each 3.5 inch diameter core is used to conduct laser particle size analysis, where the mean grain size ranges from 139.9 to 258.6 µm and sorting from 3.17 to 3.6 [*Blott and Pye*, 2001]. Furthermore, X-ray Diffraction (XRD) analysis was performed on plugs taken from each of the core series, with the quartz fraction ranging from 62 to 76 % and clay content from 8 to 15 %, see table 3.2 for greater detail on the mineral composition of each sample. In the study by *Hol et al.* [2018a] it is suggested that inelastic compaction of the Slochteren sandstone is dominantly controlled by porosity, the skewness of the grain size distribution, and the fraction of weak mineralization, while various studies [*Borg et al.*, 1960; *Brzesowsky et al.*, 2014, 2011; *Hangx et al.*, 2010] indicate the strength of sandstone grains increases with grain size. Therefore, we present the micro-structural characterization of each core plug primarily in terms of these four quantities (see table 3.2). An inferred 'strong' rock matrix contains a relatively high proportion of large quartz grains (quartz fraction), with fines between these grains (large negative skewness of particle size distribution) consisting of stronger miner-

als (plagioclase, illite, and mica), and a relatively low porosity. The inferred weak equivalent contains a high porosity with abundant weak K-feldspar (Kfs) (leached), dolomite (dol), kaolinite (Kao) and chlorite (chl) minerals, and a low proportion of fines between small grains. Considering each core in order of lowest to highest porosity, the 137 series at 19.2 % is characterised as very coarse, silty, medium sand with a high fraction (19 %BW) of weak minerals (Kfs(leached)+dol+kao+chl, *Hol et al.* [2018a]) and a low proportion of fine grain skewness ($Sk_g = -2.22$). While all samples fall within the poorly sorted range (σ_g : 2.0 to 4.0), this sample is the least well sorted ($\sigma_g = 3.59$). The 123 series has a porosity of 24.7 % and is slightly better sorted ($\sigma_g = 3.28$) with moderate fraction of weak minerals (14 %BW), with a greater fine grain skewness ($Sk_g = -2.26$). The 133 series is weakened by its high porosity (28.0 %), fine grains and low fine grain skewness ($Sk_g = -2.17$), though strengthened by a low fraction of weak minerals. The 134 series has an even higher porosity (29.6 %) with the same low fraction of weak minerals, though it has the highest fine grain skewness ($Sk_g = -2.29$) and largest average grain size. A notable difference between this core sample and the other high porosity sample is that it exhibits more than three times the permeability (351 mD vs 96.9 mD) despite having a larger proportion of fine grain material (i.e. negative skewness).

■ 3.2.2 Experimental conditions and procedure

Active source ultrasonic waveform data is recorded during both continuous linear and cyclical pore-pressure depletion, from the initial pre-depletion reservoir pressure of 35 MPa down to a maximum depletion of 3 MPa. Following the International Society of Rock Mechanics (ISRM), we employ the Uniaxial Strain Pore Pressure Depletion (UPPD) protocol [*Dudley et al.*, 2016] to simulate the mechanical response of sandstone reservoirs subject to gas production. The cyclical pore-pressure experiments referred to as UPPD-Multi Cycle are depleted at an instantaneous depletion rate of 2.5 MPa h^{-1} during intervals of cyclical loading, though an effective rate of 0.6 MPa h^{-1} depletion is maintained between these intervals. This modified UPPD protocol was devised to resolve the contribution of inelastic strain to the total strain per depletion step [*Hol et al.*, 2018a], where one (30 to 25 MPa), two (19 to 14 MPa) and three (8 to 3 MPa) step cyclical movements in pore-pressure are implemented, each consisting of three cycles with an amplitude of 5 MPa. All experiments are performed within the same type of pressure cell as depicted in fig. 3.1, in which simultaneous measurements of both mechanical and acoustic data are made. The pore-pressure is controlled on the uniaxial strain boundary condition. The active source acoustic data acquisition is performed using ultrasonic transducers at a peak operating frequency of 800 kHz as source and receiver. Noise averaging of 100 repeat measurements is performed for each measurement period $dt_{p_{j-1}}$, with a sampling frequency of 20 MHz, resulting in a single waveform of 10 000 samples or 0.5 ms in length. The repeat measurement period $dt_{p_{j-1}}$ is changed depending on the experimentation length and rate of depletion from 1, 3 or 5 min, while all other mechanical data are acquired every 0.5 s. Where Acoustic Emissions (AE) monitoring is performed, the IMaGE Cecchi data acquisition system is used with 100 to 1000 kHz frequency range operating at a detection threshold of 20 %.

Table 3.2: *Bulk rock properties characterizing each core sample used*

Core	TVD [m]	ϕ_0 [%]	Perm. [mD]	Grain Size [µm]	Sorting σ_g	Skewness Sk_g	Whole Rock (%BW)											
							Quartz	Illite/Smectite	Albite	Strong	Kaolinite/Chlorite	Microcline	Dolomite	Fe-dolomite	Weak	Barite	Siderite	TOTAL % (WR)
137	3632.9	19.2	2.0	155.4	3.59	-2.22	62	7	12	81	8	2	6	3	19	0	Tr	100
123	3562.0	24.7	61.6	139.9	3.28	-2.26	69	3	14	86	7	5	1	1	14	0	Tr	100
133	3559.8	28.0	96.9	202.4	3.17	-2.17	76	4	13	93	4	2	1	Tr	7	0	Tr	100
134	3559.9	29.6	351	258.6	3.31	-2.29	80	1	10	91	5	2	Tr	Tr	7	0	0	100

TVD denotes the True Vertical Depth origin of each sample in the ZRP test well. ϕ_0 denotes the porosity at the beginning of depletion in percent. The sorting and skewness refer to the grain size distribution as determined by the geometric method of moments [*Blott and Pye*, 2001]. The mineral content determined from XRD testing is given in terms of the whole rock percent. The Strong and Weak columns sum the content of respectively relatively strong and weak minerals indicated to the left.

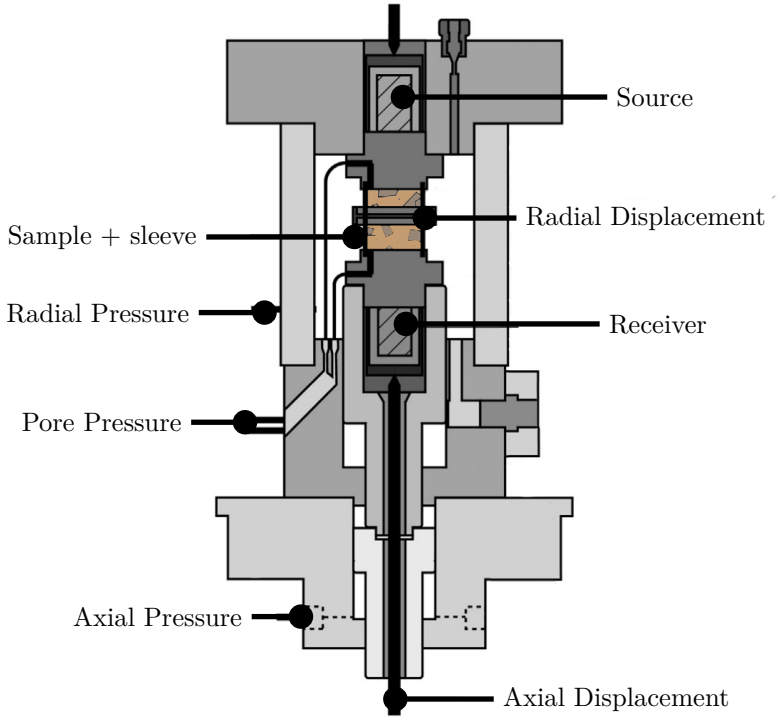

Figure 3.1: *Schematic representation of the triaxial pressure vessel. The elastomer covered sample is housed within the main pressure vessel which controls the radial pressure, while the pore-pressure is controlled by the inlet and outlet lines at either end of the sample. The axial pressure is controlled by a hydraulically-driven piston. Piezo-electric transducers, operating as source or receivers for the acquisition of acoustic data are separated from the axial ends of the test sample by stainless steel.*

■ 3.2.3 Coda-Wave analysis methods

The coda or diffuse portion of a scattered wavefield is known for its order of magnitude sensitivity gain to changes in wavefield propagation, compared to the coherent first arrivals. The phenomenological study of the coda wave in terms of the solid earth was first provided by *Aki and Chouet* [1975]. Since then there have been several approaches suggested for the practical analysis of the complex structure of these highly scattered wavefields [*Kopnichev*, 1975; *Sato*, 1977a; *Wu*, 1982; *Poupinet et al.*, 1984]. In this work, we apply three such methods with an active ultrasonic source in order to monitor pore-pressure driven compaction. In the following description of the theory the term "scatterers" is used to describe local inhomogeneities in microstructure, such as grain boundaries, intra, inter and transgranular fractures.

Furthermore, for the CWI and CWD methods a rolling-reference comparison is made between the current and past recorded wavefields, to maintain constant sensitivity to changes in material properties [*Zotz-Wilson et al.*, 2019]. For this, we define the most recently acquired monitoring wavefield as $u_{p_j}(t)$ and a previously recorded wavefield $u_{p_{j-N}}(t)$ recorded N measurement steps in the past.

Coda-Wave Interferometry

The method of Coda-Wave Interferometry (CWI) [*Snieder et al.*, 2002] monitors the velocity change between two recorded wavefields. This comparison is made by determining the lag t_s which produces the maximum time shifted cross-correlation coefficient between two wavefields as,

$$CC(t_s) = \frac{\int_{t_k-t_w}^{t_k+t_w} u_{p_{j-N}}(t) u_{p_j}(t+t_s) dt}{\left[\int_{t_k-t_w}^{t_k+t_w} u_{p_{j-N}}^2(t) dt \int_{t_k-t_w}^{t_k+t_w} u_{p_j}^2(t) dt\right]^{1/2}}. \tag{3.2.1}$$

for a time window of width $2t_w$ within the coda centred at t_k. The correlation lag t_s between $u_{p_{j-N}}(t)$ and $u_{p_j}(t)$ corresponds to the average travel time perturbation $\langle\tau\rangle$, which allows the velocity change to be determined to a first order approximation as,

$$\frac{\delta v}{v} = -\frac{\langle\tau\rangle}{t_k}. \tag{3.2.2}$$

Each incremental change determined from eqs. (3.2.1) and (3.2.2) is then cumulatively added to the previous, thereby tracking relative velocity changes derived from the coda dv/v^{coda} throughout the monitoring period.

Coda-Wave Decorrelation

A scattering material can be described by the parameters of total scattering cross-section σ_T representing the scattering power of a single scatterer, and the number density of scatterers ρ_n within the medium [*Aki and Chouet*, 1975]. The total scattering coefficient of a material is then given by,

$$g_0 = \rho_n \sigma_T \equiv {l^*}^{-1}, \tag{3.2.3}$$

where l^* is the mean free path, representative of the average distance between the scatterers. Coda-Wave Decorrelation (CWD) relates a change in the decorrelation coefficient $K(t_s) = 1 - CC(t_s)$ as determined by eq. (3.2.1) to a change in g_0. While the original formulation of CWD was developed in order to spatially locate changes in scattering within a medium [*Rossetto et al.*, 2011; *Larose et al.*, 2010], in the present study we assume a homogeneous perturbation in g_0 between perturbed and unperturbed (p and u) material states. Under this assumption the theoretical decorrelation coefficient $K^T(t)$ can be given as,

$$K^T(t) = \frac{V_0}{2} t \left|\Delta g_{0_{p-u}}\right|, \tag{3.2.4}$$

where t defines the time within the coda-wave and V_0 is the background velocity. Therefore a change in the number of scatterers ρ_n or their scattering power σ_T (e.g. size or impedance contrast), will result in an increase in the decorrelation coefficient between the two material states. In other words, the greater the difference between the two material states in terms of scattering properties, the greater the resulting decorrelation coefficient will be. Due to the use of a rolling reference comparison in eq. (3.2.1), the measured decorrelation coefficient $K(t_s)$ throughout monitoring reflects changes in the absolute || value of the rate of change in the scattering coefficient $\dot{g_0}$ [*Zotz-Wilson et al.*, 2019] or $|\dot{g_0}|$.

Multi-Lapse Time Window Analysis

The attenuation of a propagating wavefield is a necessary quantity to fully describe the evolution of energy density within the coda-wave. On a field-scale, the study of the underlying mechanisms controlling this quantity has often been driven by the desire to map attenuation within different regions [*Roecker et al.*, 1982; *Yoshimoto et al.*, 1993, 1998; *Mayeda et al.*, 1992], or in a laboratory to parameterise sedimentary rocks for resource exploration [*Mavko et al.*, 1979; *Toksoz and Johnston*, 1981]. The total measurable attenuation Q^{-1} or inverse quality factor can be defined as,

$$Q^{-1} = {}^{I}Q^{-1} + {}^{Sc}Q^{-1}, \tag{3.2.5}$$

where ${}^{I}Q^{-1}$ is the intrinsic attenuation representing the conversion of vibration energy from the wavefield to heat. Many of the proposed mechanisms by which ${}^{I}Q^{-1}$ occurs are based on observations at the microscopic scale structure of porous media. This conversion of energy from particle velocity can take place for example due to frictional sliding on the surfaces of thin cracks [*Walsh*, 1966], or due to the viscous movement of liquid through cracks or pore throats [*Walsh*, 1969]. Unlike intrinsic attenuation, the scattering ${}^{Sc}Q^{-1}$ does not remove energy from the wavefield but redistributes it within the medium. This redistribution of energy is expected to reach a maximum where the product of the scatterer radius a_1 and the dominant wavenumber k_0 reach one ($a_1 k_0 = 1$), or more generally the dominant wavelength is on the same order of the dimension of the crack/scatterer [*Kawahara et al.*, 2009]. For an angular frequency ω, ${}^{Sc}Q^{-1}$ is related to the material's scattering coefficient g_0 and seismic velocity V_0 by,

$${}^{Sc}Q^{-1} = \frac{V_0 g_0}{\omega}. \tag{3.2.6}$$

The theoretical description provided in the work by *Wu* [1985] demonstrates that the energy density distribution within a scattered wavefield can be related to the relative proportion of these two components which make up a material's total Q^{-1}. While several methods have been proposed to determine the proportion of ${}^{I}Q^{-1}$ and ${}^{Sc}Q^{-1}$ from recorded seismograms [*Aki*, 1980; *Frankel and Wennerberg*, 1987; *Jacobson*, 1987], for the purpose of the present study we make use of the Multiple Lapse-Time Window Analysis MLTWA method introduced by *Fehler et al.* [1992], which is commonly applied in seismology. As the name suggests this approach is based

on the relative variation of energy density within different time-windows, where the early portion of an S-wave is dominated by the total attenuation of the medium, while the coda consists of scattered S-waves whose amplitude is controlled by the total scattering coefficient g_0. As MLTWA is traditionally applied to seismological applications [*Rachman et al.*, 2017; *Del Pezzo et al.*, 2011; *Rachman et al.*, 2015; *Chung et al.*, 2018; *Abdel-Fattah et al.*, 2008; *Rachman et al.*, 2017; *Mayeda et al.*, 1992], it is formulated in terms of increasing distance from a source, as the goal is to spatially map the attenuative properties (proportion of ${}^{I}Q^{-1}$ and ${}^{Sc}Q^{-1}$) within a region. However, in the context of monitoring we consider the changes in attenuation over time, for a fixed location. Maintaining the notation of *Fehler et al.* [1992] we define an early time-window over the onset of the shear wave arrival, and a late time window over the coda where E_1 and E_3 define the total energy within the respective time windows. The ratio R_1 can then be defined as,

$$R_1(t_{p_j}) = \log_{10}\left[\frac{E_3(t_{p_j})}{E_1(t_{p_j})}\right] \tag{3.2.7}$$

which is dominantly affected by changes in the scattering attenuation ${}^{Sc}Q^{-1}$ within each wavefield acquired at some time t_{p_j}. For example, an increase in the energy within the coda ($E_3(t_{p_j})$) in relation to the coherent arrivals captures an increase in ${}^{Sc}Q^{-1}$ as more of the coherent energy is scattered into the coda. Note that this ratio is the inverse of that applied in seismological applications as in the laboratory environment the radial surface of the test sample is immersed in fluid, and therefore much of the energy is reflected at the sample boundaries. In other words, the scattered energy is mostly trapped within, therefore an increase in scattering power of the medium increases rather then decreases the coda energy density at the receiver. The change in a second ratio R_2 defined as,

$$R_2(t_{p_j}) = \log_{10}\left[\frac{E_1(t_{p_0})}{E_1(t_{p_j})}\right], \tag{3.2.8}$$

is dominated by the change in total attenuation Q^{-1} experience by the wavefield, as referenced to the beginning of monitoring at time t_{p_0}. The increase in the energy within window E_1 at time t_{p_j} in relation to that at time t_{p_0} represents a decrease in the materials total attenuation coefficient Q^{-1}. In other words, an increase in the coherent energy can be attributed to both a reduction in the proportion intrinsically absorbed (${}^{I}Q^{-1}$), and the proportion scattered into the coda (${}^{Sc}Q^{-1}$). Typically the ratios R_1 and R_2 are subsequently matched to either radiative transfer theory [*Hoshiba*, 1991; *Fehler et al.*, 1992] or numerically modelled seismograms [*Bianco et al.*, 2005; *Hoshiba*, 1995, 1997; *Hoshiba et al.*, 2001], thereby allowing for the quantitative characterisation of the attenuation ${}^{Sc}Q^{-1}$ and ${}^{I}Q^{-1}$. However, as the current work is only concerned with monitoring the relative changes in these properties over time, and to derive insight from this information, we forgo the additional complexity and computational effort of applying a Monte Carlo type simulation. From this simplification, we define

$$\Delta R_1(t_{p_j}) = R_1(t_{p_j}) - R_1(t_{p_{j=0}}) \approx \Delta {}^{Sc}Q^{-1}(t_{p_j}), \tag{3.2.9}$$

and

$$\Delta R_2(t_{p_j}) = R_2(t_{p_j}) - R_2(t_{p_{j=0}}) \approx \Delta Q^{-1}(t_{p_j}). \tag{3.2.10}$$

From eqs. (3.2.5), (3.2.9) and (3.2.10) $\Delta^I Q^{-1}$ is determined as

$$\Delta^I Q^{-1}(t_{p_j}) = \Delta Q^{-1}(t_{p_j}) - \Delta^{Sc} Q^{-1}(t_{p_j}). \tag{3.2.11}$$

In summary, from the application of MLTWA theory we derive parameters tracking the relative changes in Q^{-1}, ${}^{Sc}Q^{-1}$, and ${}^{I}Q^{-1}$ determined directly from the measured waveforms during monitoring.

3.3 Microstructural analysis methods

Samples from core interval 123, table 3.2, recovered from experiments conducted using 2 and 3 depletion cycles, as well as a virgin sample which was not deformed in the laboratory, were used to prepare polished sections (2.5 cm x 5 cm) for investigation of the grain scale microstructure. The samples were resin-impregnated, cut along a direction parallel to the direction of coring and axial compression, and then polished to ∼1 mm thickness. Section-scale mosaics of backscattered electron (BSE) micrographs were prepared using a FEI Helios Nanolab G3 scanning electron microscope, employing an acceleration voltage of 10 kV, beam current of 1.6 nA, and a working distance of 4 mm. Mosaic stitching was achieved using the plugin developed by *Preibisch et al.* [2009], for the open-source, Java-based image processing software "ImageJ", *Schindelin et al.* [2012]. Using each section-scale mosaic we defined subsections spanning the upper, middle, and lower parts of the sample, each measuring 80 to 170 mm^2 in size. Each subsection was used for mapping of intragranular cracks, broadly following the approach described by *Verberne and Spiers* [2017]. Cracks are identified as lineaments of black pixels within a single grain (Fig. 1), traced using an Wacom Intuos Pro pen tablet connected to ImageJ. In this method, the projected 2D crack length and curvature are reasonably accurately identified. Crack width, on the other hand, is in the majority of cases impossible to resolve using the present micrographs (fig. 3.2). Branching cracks and cracks in multiply fractured grains are counted individually. Crack mapping was performed by 3 different individuals who were unaware of sample origin, and several maps or portions thereof have been reinterpreted to check reproduction. This revealed an error of ±15 % to the number of cracks in each map (N_{cr}), which is mainly caused by interpretative ambiguities on the nature and identification of an intragranular alignment of black pixels. The crack density (ρ_{cr}) is calculated using $\rho_{cr} = N_{cr}/A_{map}(1-\phi)$, where A_{map} is the area of the BSE mosaic used for preparing the crack map overlay, and ϕ is the pore area determined using an Otsu-threshold [*Otsu*, 1979; *Verberne and Spiers*, 2017].

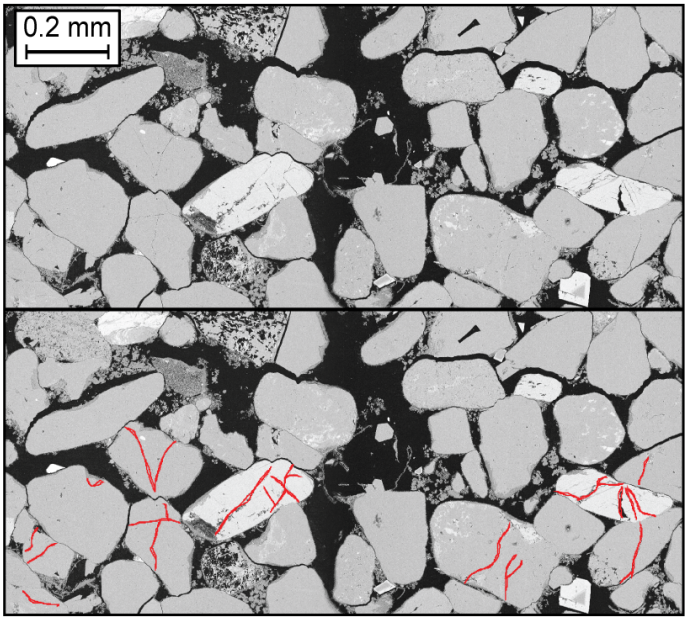

Figure 3.2: *Examples of cracks identified in each map.*

3.4 Results

Firstly we present results from coda-derived monitoring methods for two UPPD experiments performed at different rates of depletion. This is then followed by results from the UPPD-Multi-Cycle experiments, including the Acoustic Emissions (AE) data set on a single core series. Finally, we compare the microstructural characteristics of each sample with the UPPD, UPPD-MC, and AE data.

■ 3.4.1 Continuous depletion

The continuous depletion from the pressure of 35 MPa at a rate of 0.6 MPa h^{-1} takes approximately 55 h until the maximum depletion of 3 MPa is reached. Considering firstly the CWI derived relative velocity changes dv/v^{coda} for sample 137BV (fig. 3.3.b), we note the acoustoelastic [*Toupin and Bernstein*, 1961] increase with effective stress up until 25 h, after which a reduction in the rate of increase occurs, which is typically associated with the increased prevalence of inelastic deformation (micro-cracks) working to dampen the elastic increase [*Zhang et al.*, 2012b; *Selleck et al.*, 1998; *Shah and Hirose*, 2010]. Aside from this point of departure from a linear purely acoustoelastic behaviour, no additional trends are evident in these data. In comparison, the Coda Wave Decorrelation coefficient $K(|g_0|)$ and MLTWA derived attenuative properties ($\Delta\,^{Sc}Q^{-1}$, ΔQ^{-1}, and $\Delta\,^{I}Q^{-1}$) all show varying trends which are either negatively or positively correlated with the reduction in pore-pressure, see

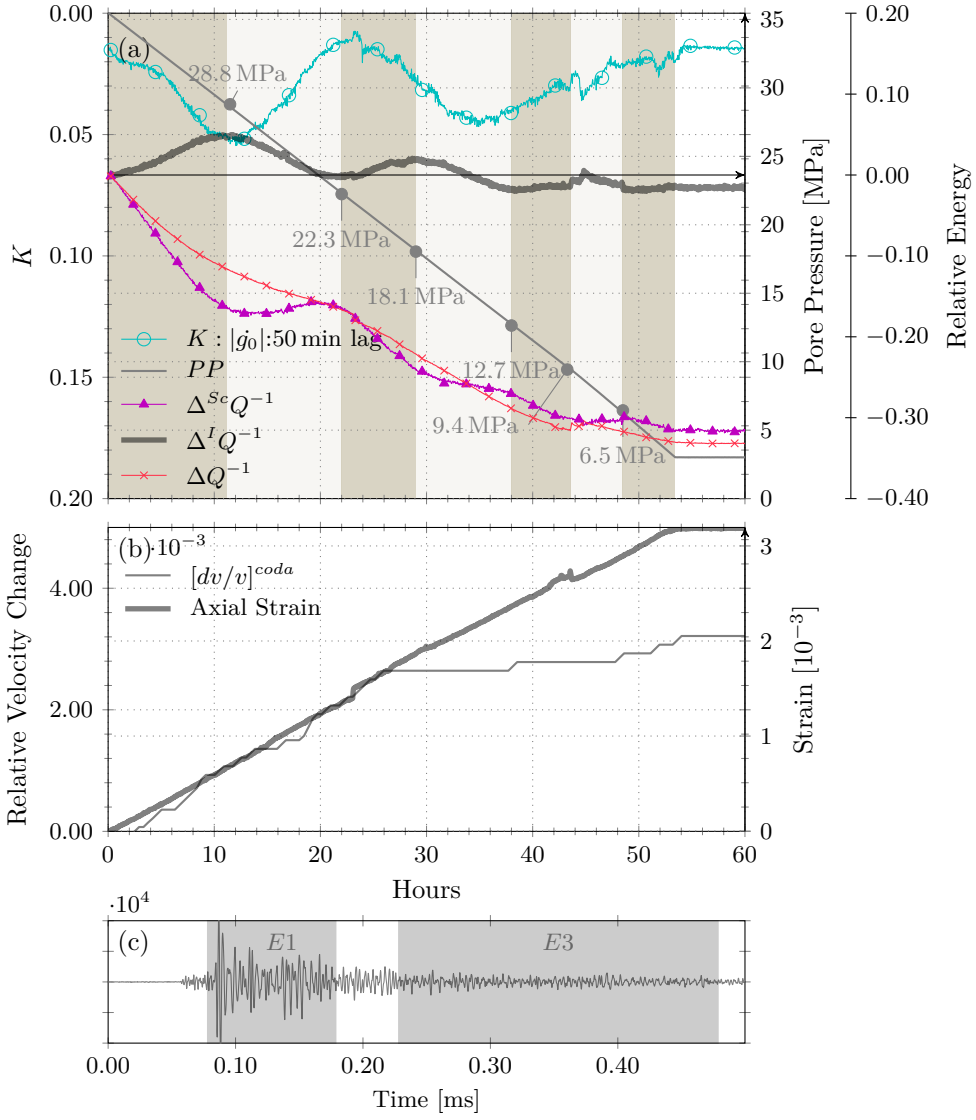

Figure 3.3: *The 137BV* 19.2 % *porosity sample depleted at* 0.6 MPa h^{-1} *with the UPPD protocol. a) Monitoring of the decorrelation coefficient* $K(|g_0|)$ *with a reference lag of* 50 min *and the relative changes in attenuative coefficients* ΔQ^{-1}, $\Delta^{Sc}Q^{-1}$, *and* $\Delta^{I}Q^{-1}$. *b) The CWI derived relative velocity changes* dv/v^{coda} *are compared with the axial strain. c) Acquired waveform showing the* 0.1 ms E_1 *and* 0.25 ms E_3 *windows.*

fig. 3.3.a. Using increasing or decreasing $\Delta\,^{I}Q^{-1}$ (positive or negative covariance) as boundary criteria, we identify 7 stages of pore pressure-depletion driven compaction;

[1] The initial reduction in pore-pressure (PP) results in an increase in $\Delta\,^{I}Q^{-1}$ while ΔQ^{-1} and $\Delta\,^{Sc}Q^{-1}$ reduce. These changes occur in line with an increase in decorrelation $K(|\dot{g_0}|)$.

[2] The first stage of reducing $\Delta\,^{I}Q^{-1}$ occurs at 28.8 MPa as $\Delta\,^{Sc}Q^{-1}$ increases while ΔQ^{-1} continues to reduce. These attenuative changes occur in line with a reduction in $K(|\dot{g_0}|)$.

[3] The second region of increasing $\Delta\,^{I}Q^{-1}$ occurs at 22.3 MPa as both $\Delta\,^{Sc}Q^{-1}$ and ΔQ^{-1} decrease, again coinciding with an increase in $K(|\dot{g_0}|)$.

[4] The second region of reducing $\Delta\,^{I}Q^{-1}$ begins at 18.1 MPa, where the slope in $\Delta\,^{Sc}Q^{-1}$ reduces, while ΔQ^{-1} maintains a near-constant rate of reduction. There is an increase in $K(|\dot{g_0}|)$ for approximately two-thirds of this stage, followed by a gradual reduction.

[5] A slight increase $\Delta\,^{I}Q^{-1}$ occurs, with the continued reduction in the total and scattering attenuation coefficients. The decorrelation coefficient $K(|\dot{g_0}|)$ continues its reduction within this stage.

[6] At the transition with the previous stage we note an increase in the rate of axial strain occurs (see fig. 3.3.b), followed by fluctuations in $K(|\dot{g_0}|)$, which are also observed in ΔQ^{-1} and $\Delta\,^{I}Q^{-1}$. For the remainder of this stage a slight reduction in $\Delta\,^{I}Q^{-1}$, and a slight increase in $\Delta\,^{Sc}Q^{-1}$ occurs. Within this region the PP drops below that at the time of coring ($\sim$10 MPa).

[7] The final region of very slightly increasing $\Delta\,^{I}Q^{-1}$ occurs up until maximum depletion at 3 MPa, as $\Delta\,^{Sc}Q^{-1}$ and ΔQ^{-1} decrease.

In summary, the continuous linear depletion protocol UPPD for sample 137BV is segmented into regions of increasing and decreasing $\Delta\,^{I}Q^{-1}$. We also note a gradual reduction in the average $\Delta\,^{I}Q^{-1}$ within each stage, and an overall reduction compared with the pre-depletion state. While the scattering attenuation $\Delta\,^{Sc}Q^{-1}$ does increase during stages 2 and 5, it follows the general reduction of ΔQ^{-1}. Unlike all other tests, due to a temporary failure of the pore-pressure line during the build up stage this sample was exposed to effective stress above reservoir conditions at the time of coring. Considering now the 29.6 % porosity 134BV sample which was depleted at a rate of 0.6 MPa h^{-1} (see, fig. 3.4) a similar segmentation into, in this case nine stages of increasing or decreasing $\Delta\,^{I}Q^{-1}$ is possible. The total Q^{-1} and scattering $^{Sc}Q^{-1}$ attenuation indicators show a continued reduction up until $\sim$10 MPa. However, in contrast with sample 137BV, Q^{-1} and $^{Sc}Q^{-1}$ begin to stabilise and then increase as maximum depletion approaches. Another difference is that a region of creep in terms of the materials attenuative properties is identified during $\sim$40 h of constant PP after maximum depletion. This region of creep also shows a single large increase in $K(|\dot{g_0}|)$ for $\sim$2 h commencing at $\sim$84 h. This sudden

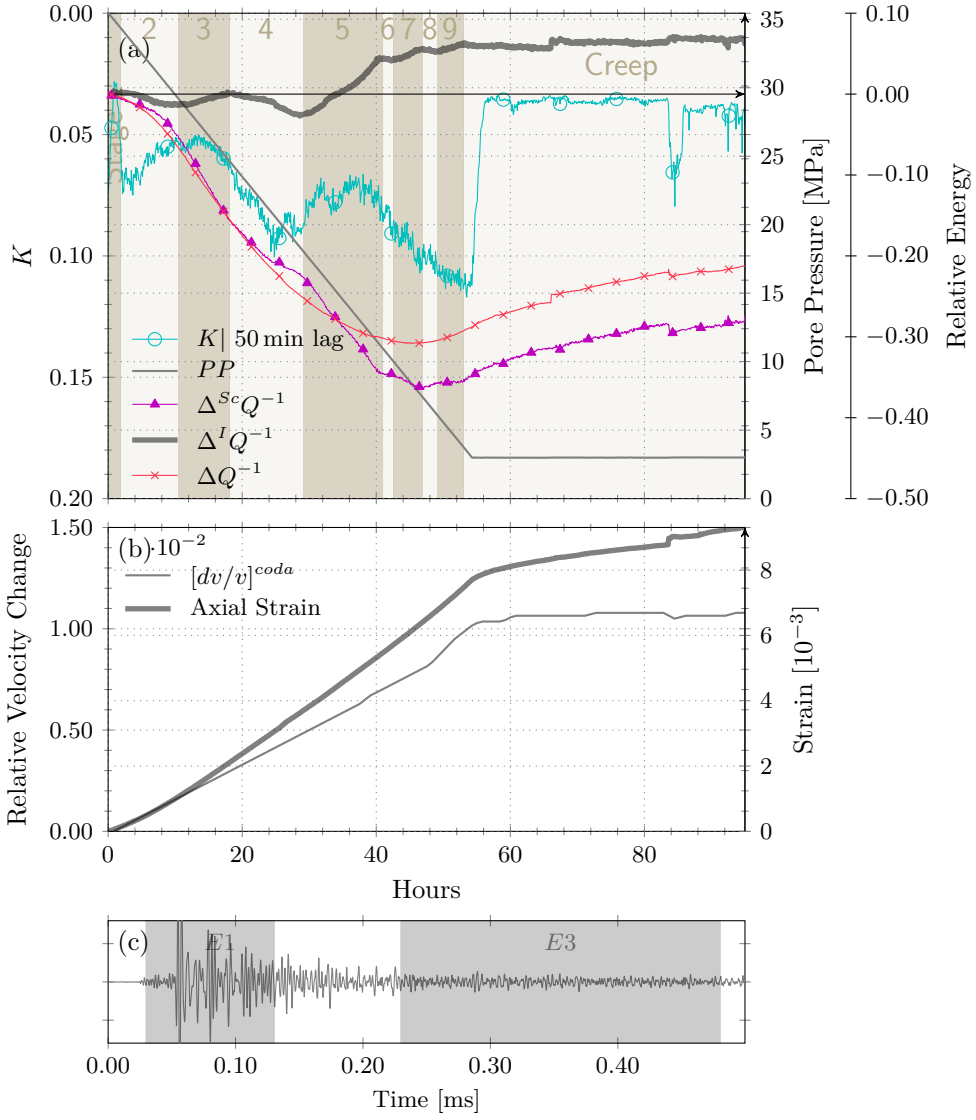

Figure 3.4: *The 134BV 29.6 % porosity sample depleted at* $0.6\,\mathrm{MPa\,h^{-1}}$ *with the UPPD protocol. a) Monitoring of the decorrelation coefficient* $K(|g_0|)$ *with a reference lag of* 50 min *and the relative changes in attenuative coefficients* ΔQ^{-1}, $\Delta\,^{Sc}Q^{-1}$, *and* $\Delta\,^{I}Q^{-1}$. *b) The CWI derived relative velocity change* dv/v^{coda} *are compared with the axial strain. c) Acquired waveform showing the* 0.1 ms E_1 *and* 0.25 ms E_3 *windows.*

change is also identifiable by a sudden increase in $\Delta\,{}^{I}Q^{-1}$ and the axial strain, while a decrease is noted for $\Delta dv/v^{coda}$, ΔQ^{-1}, and $\Delta\,{}^{Sc}Q^{-1}$. This test resulted in an overall increase, not a decrease in $\Delta\,{}^{I}Q^{-1}$ compared with the pre-depleted state. Furthermore, in contrast to sample 137BV, the relative velocity changes identified from the coda follow the trend of the axial strain profile throughout the depletion, though not during the region of creep, where it remains mostly constant. A third experiment using sample 133BV, of 28 % porosity, depleted at 2.5 MPa h^{-1}, showed ten compaction stages (fig. 3.5). In contrast with sample 134BV, a total increase in ${}^{I}Q^{-1}$ occurs only after (∼7 h) of creep following the completion of the depletion protocol. No notable increases in $\Delta\,{}^{Sc}Q^{-1}$ occurs during this creep stage. The increase in the decorrelation coefficient $K(|\dot{g}_0|)$, which results from the increased depletion rate is evident, moving from an average of ∼0.03 for 134BV to ∼0.14. Furthermore, the PP at the transitions between stages for sample 137BV is consistently lower than noted for the higher porosity samples (134 BV and 133BV). In summary, aside from the above-stated differences, all three samples (137BV, and 134/133BV) show segmentation based on ${}^{I}Q^{-1}$, and a total reduction in $\Delta\,{}^{Sc}Q^{-1}$ and Q^{-1} compared with their pre-depletion state.

■ 3.4.2 Cyclical depletion

Now that we have established the signature of pore-pressure driven compaction for a linear profile, the effects of cyclical loading on the acoustic response are considered. The modified UPPD-Multi-Cycle protocol was initially devised to study the proportion of total to elastic strain [*Hol et al.*, 2018a], though for this study we focus on its relationship with coda derived parameters ${}^{Sc}Q^{-1}$, ${}^{I}Q^{-1}$, $K(|\dot{g}_0|)$, and dv/v^{coda}. Considering sample 123AV in fig. 3.6, a total of four stages are identified as segmented by the covariance of $\Delta\,{}^{I}Q^{-1}$ with PP, with no observable creep after maximum depletion. The decorrelation coefficient $K(|\dot{g}_0|)$ reflects the changes in PP, averaging 0.09 during the first three stages. As virgin pore-pressure is reached ($PP < \sim$10 MPa) an increase to $K(|\dot{g}_0|) \approx 0.20$ occurs during the transition from stage three to four. As with the UPPD tests the relative velocity changes dv/v^{coda} reflect the profile of axial strain. To assess the significance of stage transitions in terms of Acoustic Emissions (AE), passive monitoring was performed during a full UPPD-MC protocol on a sister plug from the 123 core series (fig. 3.7). We note that large increases in the AE rate occur at 28, 21 and 8 MPa, which coincide with the stage transitions (1-2, 2-3, and 3-4) identified on the sister plug 123AV (see fig. 3.6). Furthermore, the rate of AE increase over these three regions from 12 counts/h to 23 counts/h, and then as virgin PP is reached to 25 counts/h. This point also coincides with an increase in the counts per axial strain from 100 counts per 1×10^{-3} strain to 300 counts per 1×10^{-3} strain. During the Multi-Cycle regions, and particularly at the turnaround between decreasing and increasing pore-pressure, smaller scale increases in the AE rate are also observed.

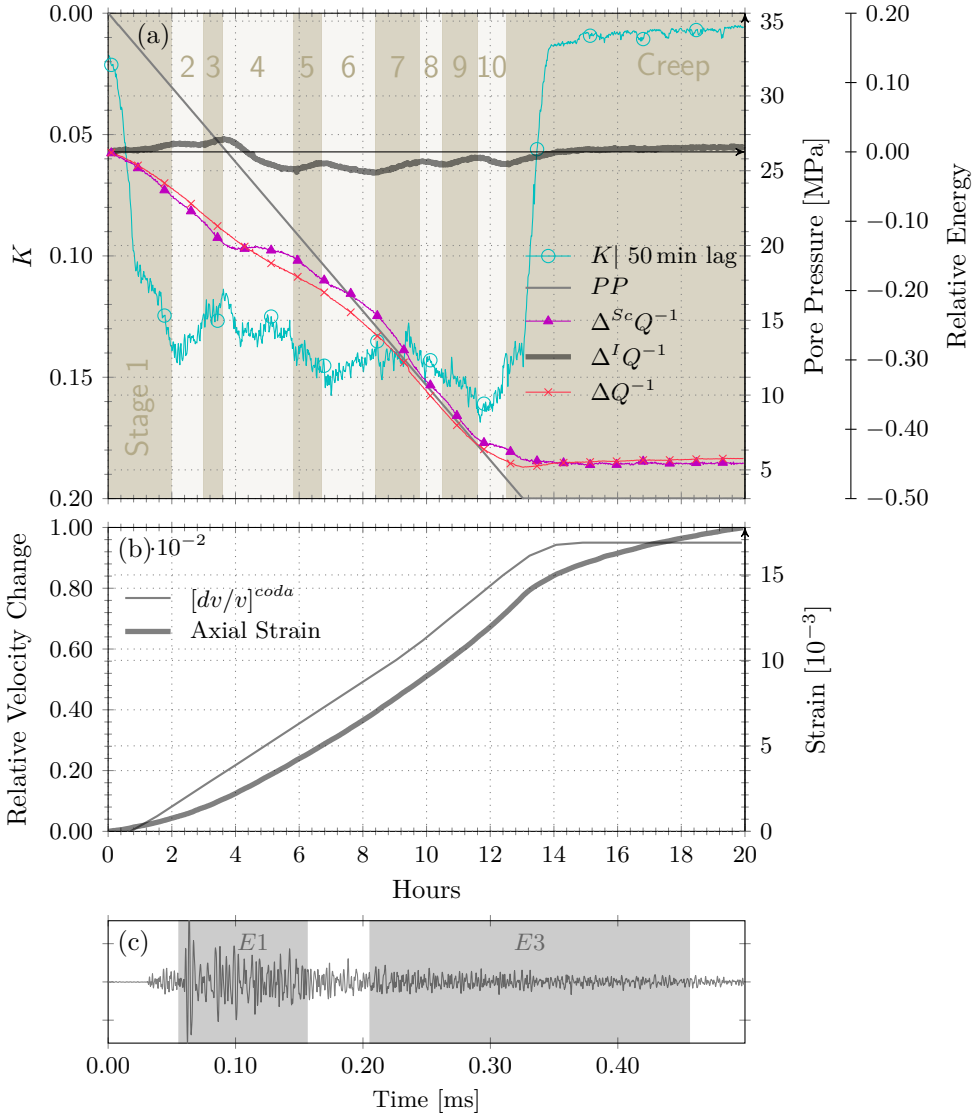

Figure 3.5: *The 133BV* 28.13 % *porosity sample depleted at* 2.5 MPa h^{-1} *with the UPPD protocol. a) Monitoring of the decorrelation coefficient* $K(|\dot{g}_0|)$ *with a reference lag of* 50 min *and the relative changes in attenuative coefficients* ΔQ^{-1}, $\Delta\,^{Sc}Q^{-1}$, *and* $\Delta\,^{I}Q^{-1}$. *b) The CWI derived relative velocity change* dv/v^{coda} *are compared with the axial strain. c) Acquired waveform showing the* 0.1 ms E_1 *and* 0.25 ms E_3 *windows.*

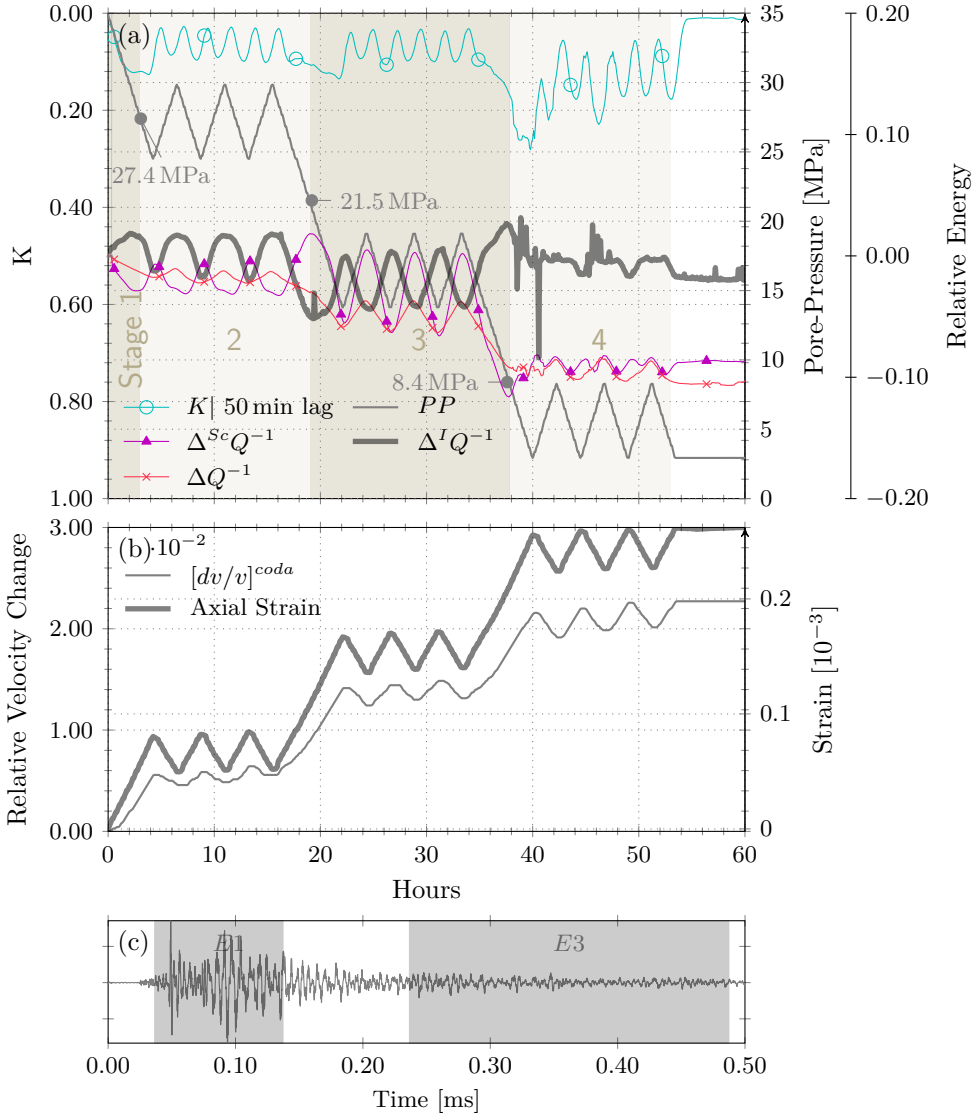

Figure 3.6: *The 123AV* 24.68 % *porosity sample depleted at* 0.6 MPa h^{-1} *with the UPPD-MC protocol. a) Monitoring of the decorrelation coefficient* $K(|g_0|)$ *with a reference lag of* 50 min *and the relative changes in attenuative coefficients* ΔQ^{-1}, $\Delta\,^{Sc}Q^{-1}$, *and* $\Delta\,^{I}Q^{-1}$. *b) The CWI derived relative velocity change* dv/v^{coda} *are compared with the axial strain. c) Acquired waveform showing the* 0.1 ms E_1 *and* 0.25 ms E_3 *windows.*

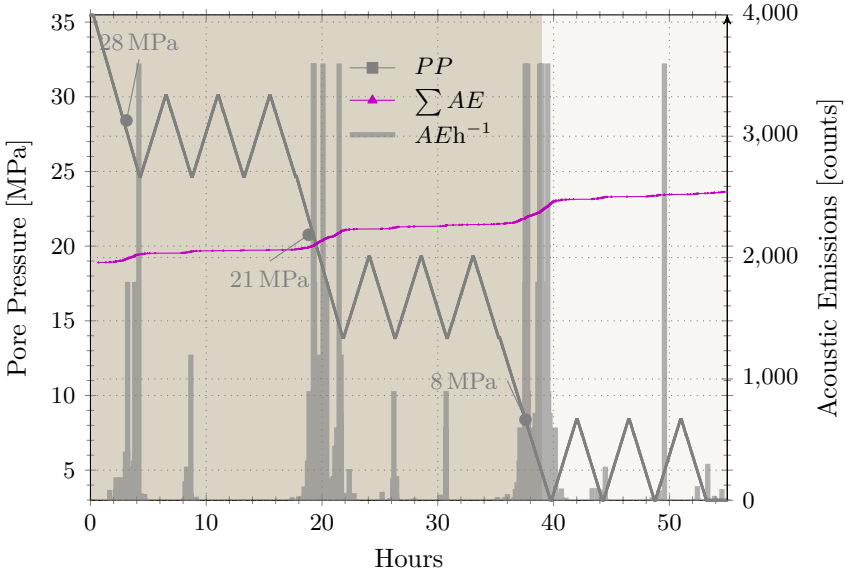

Figure 3.7: *The 123DV 24.68 % porosity sample depleted at* $0.6\,\mathrm{MPa\,h^{-1}}$ *with the UPPD-MC protocol. Acoustic Emission monitoring is performed with both the cumulative* $\sum AE$ *and rate of emissions* $AE\mathrm{h}^{-1}$ *data provided. The onset of the three regions of notable increase in AE rate are annotated in terms of the pore-pressure at which they occur.*

■ 3.4.3 Stage transitions

In fig. 3.8 we compare the pore-pressure, relative velocity dv/v^{coda}, and decorrelation $K(|\dot{g}_0|)$ at the point of transition between each of the identified compaction stages. Firstly, considering the pore-pressure (fig. 3.8.a), a separation can be observed between high (>28 %, 133BV and 134BV) and lower porosity samples. These samples show a transition between compaction stages at relatively high pore pressure (or lower effective stress) compared with all other samples. Further, the effect of Multi-Cycle loading appears to reduce both the number of stages (137AV vs 137BV) and the actual pore-pressure at which those transitions occur (stage 3-4 for 123AV and 137AV). The 123 series experiments show repeatability within 1 MPa for both the overlapping transitions (1-2 and 2-3) and the identified increase in the AE rate (123DV).

Secondly, the relative velocity change at the stage transitions (fig. 3.8.b) show dependency on both porosity and Multi-Cycle loading. Considering sister plugs 123AV and 123BV, we see close agreement between the relative velocity change at each of the overlapping stage transitions, and a continued increase to a maximum of 2.24 % change. In comparison, the 19.2 % porosity Multi-Cycle experiment 137AV shows a shallower slope and lower total change than the 123 series tests, though

compared with its sister plug (137BV) which did not experience Multi-Cycle loading, more than double the dv/v^{coda} is registered. The high porosity UPPD tests (134BV and 133BV), show a lower overall change in dv/v^{coda} than all UPPD-MC test, indicating Multi-Cycle loading plays a greater role than initial sample porosity in determining the extent to which the velocity increases.

The decorrelation $K(|\dot{g}_0|)$ however, shows no clear influence of either porosity or Multi-Cycle loading, but rather a separation based on the instantaneous rate of depletion. The UPPD experiments depleted at $0.6\,\mathrm{MPa\,h^{-1}}$ show notably lower $K(|\dot{g}_0|)$ than those depleted at $2.5\,\mathrm{MPa\,h^{-1}}$, see fig. 3.8.c. As with the pore-pressure and dv/v^{coda} stage transitions, the repeatability of the sister plugs from the 123 series is also evident in $K(|\dot{g}_0|)$.

Finally, we compare the relative change in intrinsic attenuation ${}^{I}Q^{-1}$ after maximum depletion is reached, with each samples initial porosity, see fig. 3.9. The samples with porosity below 24.68 % (series 123 and 137) showed a total reduction in ${}^{I}Q^{-1}$, whereas the two very high porosity series (133 and 134) experience an increase in ${}^{I}Q^{-1}$. These data suggest a logarithmic trend, intersecting $\Delta\,{}^{I}Q^{-1} = 0$ at ϕ_0: 27.5 %. Sample 123BV, which did not reach maximum depletion, was excluded from this fit, and shows a larger decrease in ${}^{I}Q^{-1}$ than its sister plug 123AV. The 137AV test shows a larger reduction in ${}^{I}Q^{-1}$ than its sister plug 137BV. Correlations between $\Delta\,{}^{I}Q^{-1}$ and the porosity dependent parameters of permeability and the mean grain size as well as the fraction of weak mineralisation are also identified, see fig. A.3. No clear correlations between the final $\Delta\,{}^{I}Q^{-1}$ and the grain sorting σ_g or skewness Sk_g parameters were identified.

■ 3.4.4 Microstructural analyses

Post-depletion microstructural crack map analysis was performed on backscattered electron mosaic images from the two (123BV) and three (123AV) stage depleted UPPD-MC tests. A sister plug from the same 123 series core is used as a reference to the non-depleted material state. Please refer to appendix A.3.S1 for reference high-resolution images of the stitched mosaic sections of each core plug. In table 3.3 a summary of the number of intragranular cracks N_{cr}, area of each mosaic A_{map}, and the resulting crack densities ρ_{cr} from this analysis is provided. The mapped samples showed large numbers of multiply fractured grains in a concentrated zone close to the sample ends (bottom or top), suggesting that strain localization occurred during the axial loading test [*Baud et al.*, 2004]. As crack mapping of crushed grains in dilated parts of the sample is less reliable these regions would typically be removed from the microstructual analysis. However, in order to make comparisons with the acoustic coda-derived monitoring methods which represent an ensemble response of the entire core sample, the crack density values from the ends are included, and therefore the intragranular crack density ρ_{cr} can only be assessed semi-quantitatively. Comparing N_{cr} in relation to the reference core, for both the two (123BV) and three (123AV) step UPPD-MC tests, we identify a 60 % ($\Delta N_{cr} = 6179$) and 50 % ($\Delta N_{cr} = 3233$) increase respectively. The larger total N_{cr} identified for the partially depleted (14 MPa), compared with the fully depleted (3 MPa), suggests that either

Table 3.3: *Summary of the crack map statistical properties.*

Core segment	N_{cr}	A_{map} [mm^2]	ρ_{cr} [N$_{cr}$/mm^2]	
123 (reference)				
top	766	83.1	11.6 ± 1.7	16.0
middle A	619	50.9	15.4 ± 2.3	
middle B	494	41.2	15.0 ± 2.3	
bottom	1423	86.8	21.0 ± 3.1	
123BV (2 cycles)				
top	3405	173.6	25.3 ± 3.8	26.6
middle	3271	175.1	23.8 ± 3.6	
bottom	2805	107.8	33.0 ± 5.0	
123AV (3 cycles)				
top	2436	108.5	30.7 ± 4.6	25.2
middle A	1122	63.0	22.5 ± 3.4	
middle B	961	63.2	19.1 ± 2.9	
bottom	2016	100.3	25.2 ± 3.8	

N_{cr} denotes the number of cracks, A_{map} is the area of each mosaic, while ρ_{cr} is the granular crack density.

the 123BV sample had a higher proportion of intragranular cracks before depletion, or significantly more cracks formed at a lower pore pressure than the 123AV sample. In both cases one must assume a degree of inhomogeneity in terms either in-situ crack density or granular strength within the core, from which each sister plug was taken.

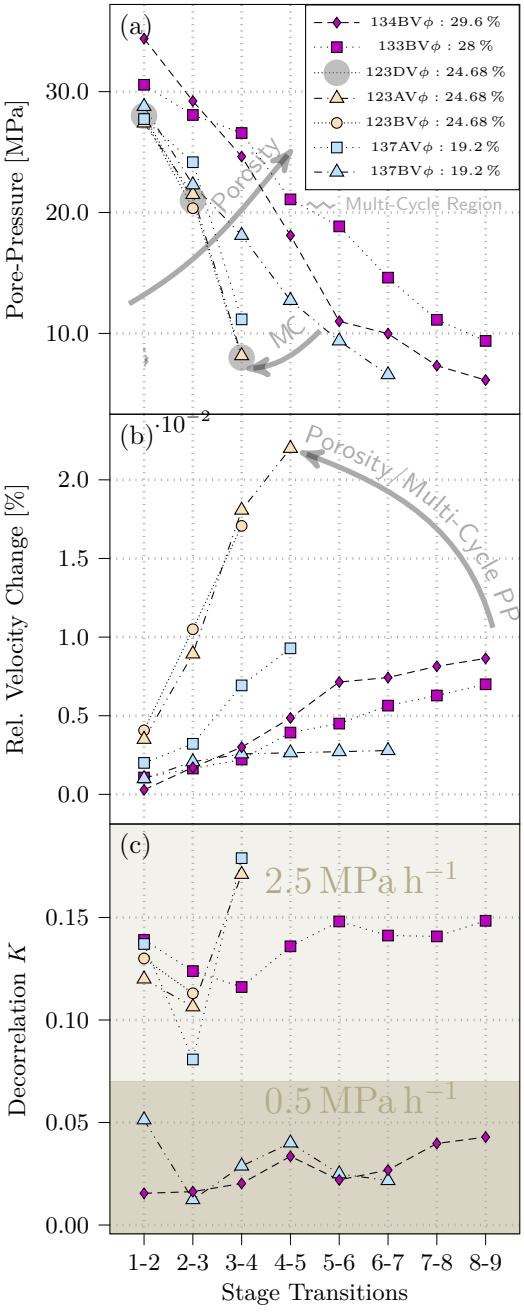

Figure 3.8: *Comparison of (a) the pore-pressure, (b) the relative velocity, and (c) the decorrelation coefficient $K(|g_0|)$ at the point of transition from increasing/decreasing $\Delta^I Q^{-1}$. Stage transitions separated by Multi-Cycle regions are annotated as such. See appendix A.2 for tests 123BV and 137AV.*

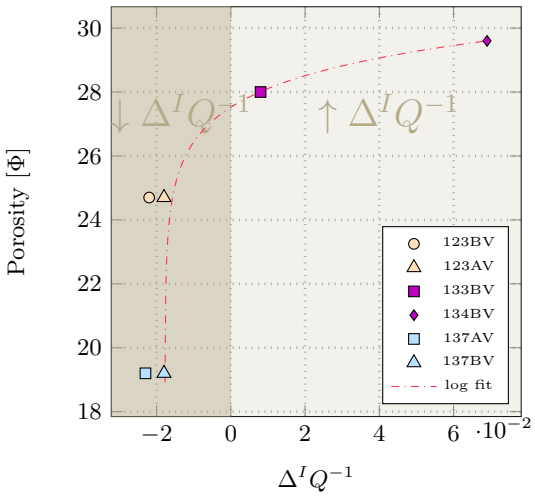

Figure 3.9: *Comparison of the relative change in the intrinsic attenuation $\Delta\,{}^{I}Q^{-1}$ at maximum depletion vs porosity. A logarithmic fit is indicated with samples <27 % porosity showing a reduction in ${}^{I}Q^{-1}$, while samples above show an increase in ${}^{I}Q^{-1}$. Sample 123BV is excluded from the logarithmic fit as it was only partially depleted. See appendix A.2 for tests 123BV and 137AV.*

3.5 Discussion

The coda-derived acoustic monitoring methods described above have all demonstrated sensitivity to pore-pressure depletion driven compaction of the Slochteren sandstone. In the following section, we will discuss in detail the interpretation of each identified stage of compaction segmented by the criteria of increasing or decreasing intrinsic attenuation. This will then be followed by discussion on the effect of the porosity, mean grain-size, grain-size skewness, mineralogy and the multi-cycle loading during depletion, on the observed changes in attenuation (${}^{I}Q^{-1}, Q^{-1}, {}^{Sc}Q^{-1}$), $K(|\dot{g}_0|)$, and dv/v^{coda}.

Generalised Conceptual Model for the observed compaction stages

The observed segmentation of pore-pressure depletion driven compaction based on changes in intrinsic attenuation $\Delta\, {}^{I}Q^{-1}$, represents additional available data in characterising the grain scale processes underway during depletion. Combined with the decorrelation coefficient $K(|\dot{g}_0|)$ and the CWI derived relative changes in velocity (dv/v^{coda}), this potentially yields valuable insight into the acoustic response of a producing reservoir. At the grain scale the intrinsic attenuation of propagating waves in porous rock occurs primarily at grain interfaces (boundaries, fractures), with negligible losses occurring within the grain material itself. Although there are several possible mechanisms for such attenuation, for fully saturated porous and permeable media at ultrasonic frequencies, the dissipation of energy due to the relative motion of the grain surface with respect to the pore fluid is expected to be dominant [*Johnston et al.*, 1979]. A theoretical description of this was first provided by *Biot* [1956] and later developed by *Stoll and Bryan* [1970], where the particle motion of a propagating wavefield translates a solid to fluid interface, in effect dragging along the adjacent pore fluid. Although this formulation is dependent on both the matrix and fluid elastic moduli, density and porosity, the viscous resistance to fluid flow as defined by,

$$b = \frac{3\mu\phi}{a_1^2}, \tag{3.5.1}$$

is expected to have the greatest influence on this viscous drag attenuative mechanism [*Stoll and Bryan*, 1970]. Here, μ is the fluid viscosity, ϕ is the matrix porosity, and $2a_1$ is characteristic of the thickness/diameter of the dilated cracks or pores. Assuming a constant fluid viscosity μ, the theory predicts that for a reduction in thickness of the in-situ cracks, an increase in b and therefore ${}^{I}Q^{-1}$ will occur. The associated reduction in porosity is expected to play a lesser role, especially for a rock matrix with a small proportion of porosity held within dilated cracks.

By considering the Biot-type flow model describing changes in ${}^{I}Q^{-1}$ as captured by eq. (3.5.1), along with changes in ${}^{Sc}Q^{-1}$, $K(|\dot{g}_0|)$, and dv/v^{coda}, we develop a generalised conceptual model for the observed stages of increasing or decreasing ${}^{I}Q^{-1}$, see table 3.4. This model is based on observations from previous studies on the Slochteren sandstone [*Pijnenburg et al.*, 2018, 2019; *Hol et al.*, 2018a], the UPPD and UPPD-MD experiments figs. 3.3 to 3.6, as well as the crack density analysis

summarised in table 3.3.

- **(a) Initial Intergranular Closure:** The in-situ fracture network open at the pre-depletion pore-pressure (35 MPa) begins to progressively close [*David et al.*, 2012; *Walsh*, 1965]. In terms of a propagating wavefield this represents a reduction in the thickness $2a_1$ and therefore the scattering cross-section σ_T. A reduction in σ_T in turn results in a reduction in g_0 (see eq. (3.2.3)) and therefore ${}^{Sc}Q^{-1}$, see eq. (3.2.6). This reduction in $2a_1$ of the open fractures and pores works to increase the materials overall resistance to fluid flow b at these locations, subsequently increasing the intrinsic attenuation ${}^{I}Q^{-1}$.

- **Transition:** The number of regions undergoing closure begins to reduce as the redistribution of stress concentrations begin to increase regions undergoing intergranular cracking/slip events.

- **(b) Intergranular slip and cracking:** The process of intergranular slip or cracking of cemented grain boundaries represents an increase in $2a_1$, σ_T and thus the scattering attenuation ${}^{Sc}Q^{-1}$. This increase in separation ($2a_1$) between grain boundaries reduces b, and therefore ${}^{I}Q^{-1}$.

- **Transition:** The number of regions undergoing intergranular cracking/slip reduce as the redistribution of stress concentrations causes an increase in the proportion of realigned grain boundaries experiencing closure.

- **(c) Subsequent Intergranular Closure:** The extent of the reduction in ${}^{Sc}Q^{-1}$ and increase in ${}^{I}Q^{-1}$ is controlled by both the number of locations experiencing closure and the magnitude of this closure. With continued depletion the total closure of some of the crack space is possible, resulting in a reduction in both ${}^{Sc}Q^{-1}$ and ${}^{I}Q^{-1}$ as the effective number density ρ_n of cracks in which viscous attenuation is possible, reduces. Where the total closure of the crack space is dominant, an overall reduction in ${}^{I}Q^{-1}$ will occur in relation to the materials pre-depletion state.

Depending on rock material properties such as the distribution of intergranular cementation strengths, the coordination number (number of loading points per grain) as controlled by the particle size skewness Sk_g, and the proportion of crack porosity, further regions of intergranular cracking and slip are possible. This is indicated in table 3.4, with increasing depletion by a repeat of stages **(b)** and **(c)**.

- **Transition:** The last available regions for closure reduce as the redistribution of stress concentrations reaches sufficient force to initiate the first intra/transgranular crack growth and formation.

- **(d) Intra/Transgranular cracking:** The formation of new intra or transgranular cracks, will increase the number density ρ_n and the scattering cross-section σ_T in the location of crack formation. The introduction of new cracks within the medium represents an increase in the number of regions capable of both scattering, ${}^{Sc}Q^{-1}$, and intrinsically attenuating, ${}^{I}Q^{-1}$, the wavefield.

Furthermore, depending on the stiffness of the resulting network of fractures, additional stages of realignment and closure followed with additional cracking is possible, indicated in table 3.4 by a repeat of stage d.

It is important to note that while this conceptual model describes the compaction process in stages dominated by either intergranular closure, intergranular cracking, or transgranular cracking, it still allows for the continuous development of inelastic deformation with effective stress [*Pijnenburg et al.*, 2018, 2019; *Hol et al.*, 2018a]. For example, in a stage characterised by predominantly intergranular closure, a lesser proportion of inelastic intergranular cracking/slip is expected. This conceptual model as summarized in table 3.4 will now be discussed in terms of the UPPD tests and their associated micro-structure. Considering firstly the 19.2 % porosity sample (fig. 3.3), during the pore-pressure depletion up until ∼10 MPa, stages of closure followed by intergranular cracking are interpreted, in terms of table 3.4 transitioning through a-b-c-b-c. A general reduction in the amplitude of oscillations in ${}^{I}Q^{-1}$ occurs during these five stages. This can be understood by considering that with increased effective stress a proportion of the crack porosity experiences total closure, and the subsequent displacement of the bound fluid. In terms of the acoustic response this results in an effective reduction in the number density of cracks ρ_n within which the Biot-type attenuative mechanism can operate. This is most evident in Stage 5 where only a very slight increase in ${}^{I}Q^{-1}$ occurs. The sudden increases in ${}^{I}Q^{-1}$ at the onset of stage 6 (44 and 45 h) is suggestive of larger scale intra/transgranular cracking, see table 3.4 panel d. This interpretation is supported by the fact that the sample has reached virgin pore-pressure ($PP < \sim$10 MPa), or effective stress levels in excess of those experienced within the reservoir. The remainder of stage 6, shows a small reduction in ${}^{I}Q^{-1}$ and an increase in ${}^{Sc}Q^{-1}$ (table 3.4), consistent with intergranular slip or cracking, see panel c.1. As maximum depletion is approached in stage 7, very slight closure and stiffening of the entire network of fractures occurs (fig. 3.3), resulting in a total negative change in ${}^{I}Q^{-1}$ in comparison to pre-depletion conditions. This indicates that the total closure of cracks which reduces the effective ρ_n, is dominant over any intragranular cracking which works to increase ρ_n and therefore ${}^{I}Q^{-1}$. This is described in panel c.2. In other words, the acoustic response of this sample indicates that predominantly intergranular cracking/slip occurs throughout depletion, with evidence of some larger intragranular cracking below ∼10 MPa.

If we apply this generalised model when interpreting the acoustic response of the two higher porosity samples 134BV and 133BV ($\phi_0 > 28$ %), we note a number of differences. Firstly, compared with sample 137BV ($\phi_0 = 19.2$ %) these high ϕ_0 samples show from 2 to 3 additional stages of transition between increasing and decreasing ${}^{I}Q^{-1}$ (see figs. 3.4 and 3.5). This is interpreted as a result of the larger total axial strain (3.2×10^{-3} vs 8×10^{-2} and 17×10^{-3}) which the higher porosity sample experience. Furthermore, both experiments show evidence of post-depletion creep, though this is much more evident in the 134BV test. In terms of material properties, both cores have the same low proportion of relatively weak minerals (7 %), though sample 134BV has a greater amount of relatively fine grains (negative skewness of −2.29 vs −2.17) which is expected to strengthen the grain framework

Table 3.4: *Interpretation of pore-pressure compaction at the grain scale.*

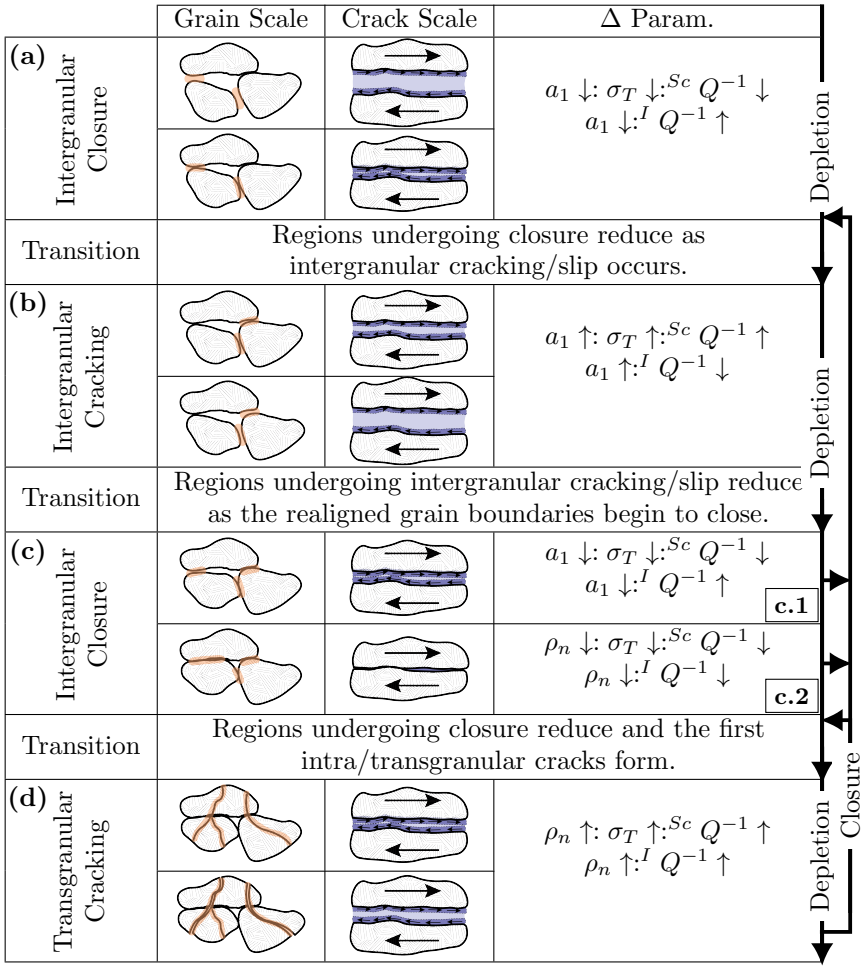

Conceptual model relating changes at the Grain/Crack scale for three grains, to changes in a materials bulk scattering and intrinsic attenuative properties, Δ Param. The increase↑/decrease↓ in the total scattering cross-section σ_T or number density of scatterers ρ_n results in an increase↑/decrease↓ in the scattering attenuation $^{Sc}Q^{-1}$. An increase↑/decrease↓ in the width or diameter of the open crack space a_1 results in a decrease↓/increase↑ in the intrinsic attenuation $^{I}Q^{-1}$. An increase↑/decrease↓ in ρ_n results in an increase↑/decrease↓ in $^{I}Q^{-1}$. At the transition between stages of compaction, a reduction in the number of regions undergoing the latter process, and an increase in the number of regions undergoing the former process occurs. The arrows to the right of the table allow for a repeat of processes with continued depletion.

[*Hol et al.*, 2018a], and a larger average grain size (258.6 µm vs 202.4 µm) which is expected to strengthen those larger grains [*Borg et al.*, 1960; *Brzesowsky et al.*, 2014, 2011; *Chuhan et al.*, 2002; *Hangx et al.*, 2010]. The larger negative skewness of grain sizes further suggests a greater distribution of both grain strengths within the sample, and the contact area and therefore intergranular friction/cementation strengths between grains. Therefore, the proportion of weak friction/cementation strengths between grains, and the proportion of weak grains is increased, which is consistent with the larger observed creep for sample 134BV after maximum depletion. These differences are also reflected in the decorrelation coefficient $K(|\dot{g}_0|)$ between 134BV and 133BV during creep, with the former showing more than double the inferred rate-of-change in g_0. As sample 134BV displays a relatively constant ${}^{I}Q^{-1}$ during this creep stage, while ${}^{Sc}Q^{-1}$ increases, this suggests that ρ_n changes little, and that the creep develops primarily by intergranular slip. Sample 133BV however shows a slight increase in ${}^{I}Q^{-1}$ and ${}^{Sc}Q^{-1}$, suggesting that the creep develops primarily by inter or intra/transgranular granular cracking. The actual mechanism for crack propagation, whether it be intra or transgranular, for relatively high porosity ($\phi_0 > 21.6\,\%$) Slochteren was identified by *Pijnenburg et al.* [2018] as stress corrosion cracking [*Brantut et al.*, 2013; *Heap et al.*, 2009, 2015].

Another difference between the two high porosity samples (134BV and 133BV) and 137BV is the overall increase in the intrinsic attenuation ${}^{I}Q^{-1}$ (see fig. 3.9). In terms of our conceptual model, this indicates that the addition of for example intragranular cracks thereby increasing ρ_n, is dominant over the total closure of cracks which works to reduce the effective ρ_n. For 134BV (fig. 3.4) this is most pronounced with the first 4 stages displaying predominately intergranular compaction, though from stage 5 onward increased intragranular crack formation begins to dominate as ${}^{I}Q^{-1}$ increases above its pre-depletion reference. In comparison 133BV only shows an eventual positive change in ${}^{I}Q^{-1}$ during the $\sim$7 h of creep following the completion of the UPPD protocol.

The transitions between stages as described in table 3.4 represents a change in the dominant grain scale compaction process. This interpretation is supported by the correlation between increased Acoustic Emissions rate (fig. 3.8.a), and the identified transition between compaction stages for two sister plugs from the same core series (figs. 3.6 and A.1). These increases in the AE rate occur at the onset of stages identified as either, intergranular cracking/slip or intergranular crack closure. This provides independent evidence that at the very least these regions represent notable changes in the compaction process. Additionally, the clear increase in the AE counts per strain below $\sim$8 MPa, supports the interpretation that increased intragranular cracking occurs towards the end of depletion, as the sample is subjected to virgin effective stress.

The presence of inelastic strain throughout the compaction of Slochteren sandstone samples was identified by *Pijnenburg et al.* [2018, 2019]; *Hol et al.* [2018a], for a range of porosities, and has also been observed during hydrostatic testing of Berea and Darley Dale sandstone [*Shalev et al.*, 2014]. *Pijnenburg et al.* [2018] infer that the presence of inelastic strain throughout compaction is related to the logarithmic distribution of grain and grain contact strengths [*Borg et al.*, 1960; *Brzesowsky*

et al., 2014, 2011; *Chuhan et al.*, 2002; *Hangx et al.*, 2010] resulting in early inelastic strain development. Our coda-wave derived monitoring of Q^{-1}, ${}^{Sc}Q^{-1}$, ${}^{I}Q^{-1}$, $K|\dot{g_0}|$, and AE not only corroborates this finding, but provides evidence that pore-pressure driven compaction in the Slochteren sandstone may be subdivided into several serial processes (stages), characterised by predominately intergranular closure followed by predominately intergranular slip, and depending on the micro-structural properties of the sample, eventually the pervasive formation of intragranular/transgranular cracks. We suggest through a generalised conceptual model, which is itself based on Biot-type attenuation, that the mechanism by which the transition between the identified stages of compaction occurs is the continuous re-distribution of stress concentrations within the grain structure.

■ 3.5.1 Effect of initial sample properties and multi-cycling on compaction stages

In this section, we discuss the relative effect of the initial sample properties such as porosity, permeability, mean grain size and the Multi-Cycling of pore pressure on the identified stages of compaction. These parameters will be discussed in terms of the pore-pressure, relative velocity change dv/v^{coda}, decorrelation coefficient $K|\dot{g_0}|$, and attenuation ${}^{I}Q^{-1}$.

Considering firstly porosity, the fact that the high porosity (134BV and 133BV) samples show stage transitions at consistently higher pore-pressure (fig. 3.8.a) indicates unsurprisingly that the onset of predominately intergranular cracking or slip for these samples occurs at a lower effective stress. The relative velocity change also shows a clear positive dependency on the initial sample porosity as is expected by the acoustoelastic stiffening of the core (fig. 3.8.b). The decorrelation coefficient $K(|\dot{g_0}|)$ however, appears to be mostly influenced by the rate-of-depletion. Its apparent porosity independence can be understood, when considering that $K(|\dot{g_0}|)$ is determined from the normalised cross-correlation, and is therefore only dependent on the rate-of-change in the scattering coefficient g_0, which is obviously dependent on the rate at which the sample is depleted. The identified logarithmic relationship between porosity and the relative change in intrinsic attenuation ${}^{I}Q^{-1}$ (fig. 3.9) indicates that for initial sample porosity greater than 27 % an eventual increase in ${}^{I}Q^{-1}$ is expected, and otherwise a reduction. In terms of the presented conceptual compaction model this describes a situation where the lower porosity samples (123BV/AV and 137BV/AV) experience a greater proportion of total closure of the crack space, and thus a reduction in the effective number density ρ_n of cracks in which such viscous attenuation occurs. Conversely, the higher porosity samples indicate that a lower portion of the crack space fully closes and a greater proportion of intragranular cracks form, thereby increasing ρ_n in which viscous attenuation occurs. This interpretation is supported by the fact that the partially depleted 123BV sample with a larger number of intragranular cracks ($N_{cr} = 6179$) displayed a larger final $\Delta\,{}^{I}Q^{-1}$ than its fully depleted 123AV sister plug ($N_{cr} = 3233$). This indicates that for this 24.7 % ϕ_0 sample, the majority of the intragranular crack space was present prior to the onset of depletion, thereby resulting in a greater number of fully closed cracks, despite only undergoing a partial depletion of the pore pressure

(14 MPa verses 3 MPa). If alternatively, the observed larger N_{cr} in this sample were formed during the depletion process, one would expect a relative increase in $\Delta\,^{I}Q^{-1}$, which is not the case. Consequently, this indicates some degree of inhomogeneity in terms of crack density within the 123 core, from which plugs BV and AV are taken. The observed N_{cr} and total change in $\Delta\,^{I}Q^{-1}$ support the findings of *Pijnenburg et al.* [2018], that intergranular cracking occurs mostly in the lower porosity samples, with only those of higher initial porosity resulting in pronounced intragranular cracking. Furthermore, in sandstones generally, intergranular cracking combined with intergranular slip are expected to be the dominant inelastic mechanisms at the onset of compression [*Shalev et al.*, 2014; *Bernabé et al.*, 1994; *DiGiovanni et al.*, 2007; *Ord et al.*, 1991; *David et al.*, 2001; *Menéndez et al.*, 1996]. The expectation of a reduction in the proportion of crack/pore space which experiences total closure for the highly porous and permeable samples can be understood when considering that the majority of this volume is held within large aspect ratio pores, which do not fully close under pressure. *Fatt and Davis* [1952] found a reduction in effective permeability of 25 % for sandstone, while *Frangos* [1967] noted up to an order of magnitude reduction for the much less permeable Westerly granite, which can be interpreted as a greater proportion of fully closed crack space.

While initial sample porosity can be generally considered to have the greatest influence on the development of inelastic strain [*Hol et al.*, 2018b,a; *Pijnenburg et al.*, 2018, 2019], we also note correlations between the total change in $\Delta\,^{I}Q^{-1}$ and the initial permeability, mean grain-size, and the fraction of weak mineralisation (fig. A.3). Clearly both permeability and mean grain-size cannot be considered as independent of sample porosity, and as such show the same positive correlation with $\Delta\,^{I}Q^{-1}$. The fraction of weak mineralisation, however shows a negative correlation with increasing $\Delta\,^{I}Q^{-1}$, which supports the findings of *Hol et al.* [2018b,a], namely that the presence of increase weak mineralisation increases the proportion of inelastic intergranular strain and therefore the proportion of totally closed cracks.

The strain hardening influence of the cyclical loading of stress on the Slochteren sandstone was noted by *Pijnenburg et al.* [2018], with a clear dependency on initial sample porosity. The repeated cycling of pore-pressure performed during the UPPD-MC test can be expected to accelerate the redistribution of stress concentrations at the grain scale. In terms of the acoustic response, this is considered as the reason for the observed reduced number of compaction stages, and larger relative velocity increase (acoustoelastic effect [*Grinfeld and Norris*, 1996]), noted in all Multi-Cycle tests. Further, the influence of the Multi-Cycle loading on the acoustoelastic stiffening of the samples appears to be dominant over a samples ϕ_0.

In summary, the application of the presented coda-derived monitoring methods indicate that pore-pressure driven compaction in the Slochteren sandstone may be subdivided into several serial processes (stages), characterised by predominately intergranular closure followed by predominately intergranular slip, and depending on the micro-structural properties of the sample, eventually the pervasive formation of intragranular/transgranular cracks. The presented discussion provides a first step towards characterising the acoustic response of the Slochteren sandstone in terms of different material properties. Fluctuations in $K|\dot{g}_0|$ have been shown to

correspond to the onset of virgin pore-pressure levels, as well as indicating the sudden formation of larger transgranular cracks. The point at which $\Delta\,{}^{I}Q^{-1}$ begins to steadily increase has been linked with the pervasive increase in crack density for high porosity samples. The ability to constrain such changes to a particular pore-pressure during a depletion test provides valuable additional information on the compaction process. We therefore suggest, that with sufficient data to enable statistical analysis, an improved understanding of the relative importance and interdependencies of the possible proxies for inelastic compaction will result.

■ 3.5.2 Implications on the depletion of seismogenic sandstone reservoirs

The release of seismicity within the Groningen gas field has been shown to occur primarily along preexisting faults [*Dost et al.*, 2017; *Spetzler and Dost*, 2017; *Lele et al.*, 2016], due to differential compaction of the surrounding strata [*Mulders*, 2003]. In the studies of *Van Eijs et al.* [2006]; *Bourne et al.* [2014], generally three key parameters are identified as important in controlling seismicity: the extent of the depletion pressure drop (ΔP), reservoir fault density (F), and the compressibility (c_m). While ΔP and F simply state the requirement for a significant pressure drop within the vicinity of an existing fault, c_m states that the surrounding material is sufficiently compressible such that, for example frictional forces can build up along faults. If we extrapolate the findings of this study to the field-scale, regions of Slochteren sandstone with initial porosity above 27 % are expected to experience a relative increase in the Biot-type intrinsic attenuation as maximum depletion is approached. Our generalised conceptual model suggests that this increase in ${}^{I}Q^{-1}$ is due to the pervasive formation of intragranular cracks, resulting in a large increase in c_m. Such an increase in granular cracking and therefore compaction for the very highest porosity regions, has implications for both the development of induced seismicity and probabilistic hazard maps [*Dost et al.*, 2017], not to mention geomechanical modelling for the reservoir in question. The importance of including the inelastic component of compaction has also been highlighted by *Pijnenburg et al.* [2019] for geomechanical models which typically make a poroelastic assumption [*Bourne et al.*, 2014; *Lele et al.*, 2016; *Wassing*, 2015; *Dempsey and Suckale*, 2017; *Zbinden et al.*, 2017].

The Biot-type intrinsic attenuative mechanism considered in this study is frequency-dependent, and is only expected to be measurable for a source wavefield operating at ultrasonic frequencies. This limits in-field monitoring infrastructure to an in-borehole, kHz source and receiver setup, similar to that applied at the San Andreas Fault Observatory at Depth (SAFOD) [*Zoback et al.*, 2011], near Parkfield, California. Despite the coverage of such a setup being limited to near-borehole changes, it still represents an improvement in terms of sensitivity, and spatial/temporal resolution when compared to the radioactive depth markers, or Distributed Strain Sensing (DSS). If one however considers, active source monitoring at seismic frequencies, a cross-well setup becomes a feasible application. While the influence of Biot-type attenuation will not be measurable, other intrinsic attenuative mechanisms such as squirting flow or friction loss [*Johnston et al.*, 1979] are expected to become dominant, and sensitive to grain scale variations in fluid saturation and pore-pressure.

While there have been numerous works which monitor changes in attenuation, at both the laboratory [*Lockner et al.*, 1977; *Barnhoorn et al.*, 2018] and field-scale [*RAJI and Rietbrock*, 2012; *Shabelansky et al.*, 2015], to the authors' knowledge, monitoring changes in scattering and intrinsic attenuation as components to total attenuation has received no attention. At surface seismic frequencies 3–100 Hz, this can be attributed to the fact that scattering attenuation is strongly dependent on frequency ($\propto f^{1.48}$ [*Akinci and Eyidoan*, 2000], $\propto f^4$ [*Johnston et al.*, 1979]), and therefore is no longer influenced by grain scale changes. In a closely spaced cross-well setup however, 300–1300 Hz has been shown to be achievable [*Zhang et al.*, 2012a], and can be expected to be sensitive to metre scale changes in, for example preexisting fracture networks. Such a monitoring setup may maintain sensitivity to changes in attenuation associated with for example, the introduction of fluid into a fracture network, a process which has itself been linked with increased risk of induced seismicity [*Zbinden et al.*, 2017]. We therefore suggest, that with further investigation into the relationship between reservoir properties and continued compaction, at such cross-well seismic frequencies, improvements to both the timeliness and spatial coverage of compaction monitoring will result. This can be expected to have direct benefits in terms of seismicity and subsidence modelling, for example by providing information on the development of changes around preexisting faults which are too small to be reliably mapped [*Bourne et al.*, 2014]. Furthermore, it would represent a meaningful step towards real-time active source monitoring of compaction, and the possible detection of subtle/precursory indicators to large-scale induced seismicity. As passive seismicity monitoring is only capable of detecting events which are sufficiently large to reach the borehole receivers, it is insensitive to small events happening at the grain scale, not to mention any pre-seismic compaction changes. In contrast, an active-source repeat survey is in principle able to detect both truly pre-seismic changes, as well as seismicity of insufficient magnitude to reach a receiver.

3.6 Conclusion

In this study, we performed Uniaxial Strain Pore Pressure Depletion (UPPD) experiments on Slochteren sandstone core samples, taken from a test well in the centre of the seismogenic Groningen gas field. The applied depletion in each test commenced at the pre-production reservoir pore-pressure of ∼35 MPa, and ended below the reservoir coring pressure (∼10 MPa) to a maximum depletion of 3 MPa. Fully and partially depleted UPPD Multi-Cycle experiments were performed, and on one core series both pre and post microstructural comparisons and Acoustic Emissions monitoring were conducted. Comparisons between these data were used to infer the influence of both MC pore-pressure fluctuations and the formation of intra/transgranular cracks. All experiments, aside from the AE dataset were monitored with axially mounted receiver and source transducers operating at ultrasonic frequencies, with regular repeat measurements every few minutes. From this dataset, we applied three coda-derived monitoring methods which infer changes in the scattering coefficient $|\dot{g}_0|$, the velocity dv/v^{coda}, and the scattering ${}^{Sc}Q^{-1}$ and intrinsic

${}^{I}Q^{-1}$ attenuation. The main conclusions of this work are;

- The analysis of the changes in scattering and Biot-type intrinsic attenuation throughout depletion, indicate that compaction occurs in stages of predominantly intergranular closure, transitioning into predominantly intergranular slip/cracking. With continued depletion, and a suitably weak grain structure, the pervasive formation of intra/transgranular cracks is expected.
- The total relative increase in ${}^{I}Q^{-1}$ at the end of depletion for samples of $\phi_0 > 27\,\%$ (fig. 3.9) indicates that, for the very highest porosity Slochteren sandstones, the pervasive increase in crack density dominates over the closure of preexisting cracks.
- Acoustic Emissions monitoring shows that a significant increase in grain scale seismicity occurs at regions identified as either the onset of intergranular slip/cracking or the onset of predominantly closure. The tripling of the AE counts per strain below $\sim$8 MPa, supports the interpretation that intergranular or transgranular cracking occurs towards the end of depletion, below the reservoir coring pressure.
- The transition from reservoir coring to virgin pore-pressure is identifiable by an increase in $K(|\dot{g}_0|)$, and the stabilisation or increase (where $\phi_0 > 27\%$) in ${}^{I}Q^{-1}$.

Acknowledgments

The authors thank Nederlandse Aardolie Maatschappij (Jan van Elk, Dirk Doornhof) and Shell Global Solutions International (Sander Hol, Fons Marcelis and Ab Coorn) for their collaboration with the Delft University of Technology, without which this work would not be possible. A special thanks goes to Steve Oates for his review of the manuscript before submission. The raw acoustic and mechanical data used in this study is available at *Zotz-Wilson* [2019a], under the name "Zotz-Wilson, Reuben; Filippidou, Nikoletta; Van Der Linder, Arjan; Verberne, Berend; Barnhoorn, Auke: Acoustic, mechanical, and microstructure data used in: Coda-Wave Based Monitoring of Pore-Pressure Depletion-driven Compaction of Slochteren Sandstone Samples from the Groningen Gas Field". The python module pyCoda developed for the purpose of data processing and analysis is available through the open-source release [*Zotz-Wilson*, 2019b].

4

Ultrasonic imaging of the onset and growth of fractures within partially saturated Whitby Mudstone using coda-wave decorrelation inversion

Abstract Coda-wave Decorrelation (CWD) time-lapse imaging during the triaxial compression of Whitby Mudstone cores provides a 3-D description of the evolution and redistribution of inelastic strain concentrations. Acoustic Emissions (AE) monitoring is also performed between any two consecutive active source surveys. From these data, we investigate the impact of initial water saturation S_w on the onset, growth, and reactivation of inelastic deformation, compared to the post-deformation fracture network extracted from X-ray tomography scans. Our results indicate for the applied strain-rate and degree of initial water saturation that the Whitby mudstone does not produce any AE of sufficient magnitude to be detected above the noise level. This is true for both the initial onset of inelasticity, and during the region failure. In contrast, the CWD results indicate the onset of what is interpreted as localised regions of inelastic strain at less than fifty percent of peak differential stress. The aseismic nature of these clay-rich rocks suggests that mostly plastic deformation occurs, from the microscopic, up until macroscopic shear fracture failure.

Under Review: Zotz-Wilson R., Douma L.,Sarout J., Dautriat J., Dewhurst D., Barnhoorn A., (2019), Ultrasonic Imaging of the onset and growth of fractures within Partially Saturated Whitby Mudstone using coda-wave decorrelation inversion, Journal of Geophysical Research - Solid Earth. Note that minor changes have been introduced to make the text consistent with the other chapters.

4.1 Introduction

Mudstones play an important role in many civil infrastructure, energy and resource projects globally. They act as impermeable seals in conventional hydrocarbon or carbon capture reservoirs [*Busch et al.*, 2008; *Armitage et al.*, 2016], or as both a source [*Jianghui et al.*, 2012] and reservoir rock [*Aplin and Macquaker*, 2011] in unconventional hydrocarbon projects. Several permanent nuclear storage projects plan to [*Brookins*, 1976; *Vomvoris et al.*, 2013] or already employ [*Aikas and Sundell*, 2014] mudstones as the host rock for both high and low grade radioactive waste. Due to their global abundance [*Garrels and Mackenzie*, 1969], civil infrastructure project such as tunnels, dams, and bridges often directly interact with mudstones [*Yoshida et al.*, 1997; *Wang et al.*, 2013; *Izumi et al.*, 1998], presenting a variety of engineering challenges. Furthermore, shales and mudstones are considered as a key input when developing susceptibility maps for environmental damage due to landslides [*Ayalew and Yamagishi*, 2005]. It is therefore essential to gain an understanding of the mechanical properties of mudstones under a variety of environmental conditions. To this end, laboratory triaxial testing of core samples subjected to realistic subsurface temperature, pressure, stress, and saturation conditions are essential. While the bulk core properties are generally attainable by measurements at the boundary, the determination of the time and location at which inelastic changes develop, requires techniques which are sensitive to localised changes within the core. Acoustic Emissions (AEs) monitoring has been a commonly applied technique within rock-mechanics laboratories for more than two decades [*Lockner*, 1993; *Lei et al.*, 2004; *Heap et al.*, 2009; *Sarout et al.*, 2017], enabling the rate, location, and effective stress at which fracturing develops to be extracted from passive acoustic monitoring. Some inherent limitation of AEs monitoring are that it requires: (i) the magnitude of acoustic energy emitted during fracturing to be sufficiently large; (ii) and within the dynamic range that it is detectable by the available sensor network. Further, AEs monitoring is unable to detect inelastic changes which are truly aseismic in nature [*Main*, 1990].

In this study, we apply both active source acoustic and passive AEs monitoring, on three laboratory scale core samples of different initial water saturation. The aim is to monitor both the location and time of fracturing from active source monitoring, in comparison with the onset of AEs, thereby providing an indication of the degree to which pre-seismic changes occur. This is based on the premise that active source methods do not rely on the spontaneous emission of acoustic energy in order to detect the presence of inelastic deformation, and therefore remain in principle sensitive to aseismic fracturing. While there have been a number of velocity tomography monitoring applications in laboratory rock deformation experiments [*Jansen et al.*, 1993; *Brantut*, 2018; *Aben et al.*, 2019], enabling the three-dimensional imaging of rock fracturing, in this work we apply Coda-Wave Decorrelation (CWD) inversion for the first time within experimental rock mechanics. The CWD method makes use of the coda of recorded waveforms and therefore can be expected to display improved sensitivity when compared to methods which rely on the coherent arrivals [*Snieder*, 2002a; *Grêt*, 2005; *Zotz-Wilson et al.*, 2019]. While the first publication

and experimental application of CWD demonstrates the ability of the method to locate, in a probabilistic sense, the formation of a single defect within a concrete slab [*Larose et al.*, 2010], in this study we apply a least-squares approach which has the potential to locate, in terms of a physical quantity, multiple regions of change simultaneously [*Planès et al.*, 2015].

The results of this study, monitoring the active and passive acoustic response of mudstone samples of differing initial water saturation, provides valuable information on the development of both microscopic inelastic strain (diffuse damage) and the emergence of larger coalesced macroscopic shear fractures.

4.2 Materials and methods

■ 4.2.1 Sample material and preparation

The mudstone samples originate from the outcropping Whitby Mudstone formation (WMF), United Kingdom (UK). The WMF is deposited in the East-English Cleveland Basin in anoxic bottom conditions [*Powell*, 2010]. This Toarcian Age mudstone formation consists of three members, including the Grey Shale Member, Mulgrave Shale Member, and Alum Shale Member [*Powell*, 2010]. The Mulgrave Shale Member (Lower Jurassic) is the lateral equivalent of the Dutch Posidonia Shale Formation (PSF), the main shale gas target in the Netherlands. The maximum burial depth of the mudstones in the Cleveland Basin is ∼4 km, where the top of the Lower Jurassic does not exceed ∼2.5 km [*Pye*, 1985]. The WMF has been considered an analogue for the Dutch PSF [*Zijp et al.*, 2015], since the PSF is not outcropping in the Netherlands, core material is badly preserved, and available log data is limited.

The WMF is a relatively clay-rich rock, composed of 50 % to 70 % inter-layered illite/smectite, illite, and kaolinite [*Houben et al.*, 2016a]. The organic matter (TOC ∼6 %) is often inter-layered within the matrix [*Zijp et al.*, 2015; *Houben et al.*, 2016a]. The porosity of the mudstones originating from the Mulgrave Shale Member is ∼13 %, based on the wet and dry mass of a mudstone core [*Douma et al.*, 2019]. The matrix permeability is in the range of $10 \times 10^{-23}\,\mathrm{m}^2$ to $10 \times 10^{-18}\,\mathrm{m}^2$, and pore diameters are between 72 and 300 nm [*Houben et al.*, 2016b].

Mudstone blocks are sampled from a wave-cut platform on the east coast of England, north of Whitby (UK), near Runswick Bay. The mudstones in the outcrop are submerged daily by seawater, due to the tidal cycle. Immediately after sampling, the mudstone blocks were stored in seawater to prevent initial pore water loss. Seawater was used because the assumption was made that the pore fluid of the mudstones became in chemical equilibrium with the seawater over geological time. Cylindrical core plugs were cored normal to the bedding out of the same larger sample block and have a length of ∼80 mm and a diameter of ∼40 mm. During coring, seawater was used as cooling fluid to prevent shrinkage or swelling of the clays. After coring, the core plugs were stored at room temperature in three different desiccators with a constant relative humidity atmosphere of ∼85 %, 75 %, and 35 %. At these relative humidities, the corresponding water saturations achieved after several weeks

(until mass stabilization) are $\sim 70 \pm 10\,\%$, $\sim 58 \pm 10\,\%$, and $\sim 28 \pm 10\,\%$, obtained by subtracting the brine volume divided by the pore volume from the initial water saturation [*Douma et al.*, 2019]. The different relative humidity atmospheres were created by using oversaturated brine solutions, as explained in detail by *Laloui et al.* [2013]. The three core plugs were used for rock mechanical testing after equilibrating for approximately two months in a desiccator.

■ 4.2.2 Experimental procedure

The experimental setup used for the mechanical and ultrasonic testing includes a triaxial stress vessel, multichannel ultrasonic monitoring system, and ultrasonic P-wave transducers. A similar setup was used by *Sarout et al.* [2015, 2017] and *Douma et al.* [2019]. The partially-saturated core plugs are placed in a Viton sleeve to prevent contact with the surrounding confining oil. Two opposed linear variable differential transformers (LVDTs) monitor the axial displacement. The local circumferential strain is measured with a strain gauge-based cantilever mounted through the Viton sleeve, directly on the lateral surface of the core plug.

Two aluminium spacers (38 mm diameter; 1 mm thickness) are placed on top and bottom of the partially-saturated core plugs (see fig. 4.1), to achieve macroscopically undrained conditions during the deformation of the rock. This means that there is no pore pressure control or monitoring during testing, and that no fluid is allowed to exit the core plug. The experiments are all performed at room temperature (22 °C). A detailed description of the experimental procedure is given by *Douma et al.* [2019], though in essence this can be summarised as:

- An increase in confining pressure at a rate of $0.5\,\mathrm{MPa\,min^{-1}}$ until 15 MPa, followed by a consolidation stage of about three days under isotropic stress conditions.
- Subsequently, a vertical stress is applied orthogonal to the bedding with a constant axial strain rate of $1 \times 10^{-7}\,\mathrm{s^{-1}}$ until failure of the WMF sample.

A total of fourteen piezo-ceramic-based P-wave transducers (footprint diameter 6 mm, dominant resonant frequency 0.5 MHz) are directly attached to the Whitby Mudstone (WM) sample (see fig. 4.1), through the Viton sleeve, which record the ultrasonic signals propagated through the sample from a particular transducer. Each transducer acts sequentially as a source S_i, while the other thirteen transducers act as receivers/sensors R_j. During each survey, multiple repeat measurements are performed, and the recorded waveforms are stacking at each R_j, thereby improving the Signal-to-Noise Ratio (SNR). Each survey consists of 182 (14×13) stacked waveforms, recorded during a time window of 410 µs, at a sampling rate of 10 MHz, and an amplitude resolution of 12-bit [*Sarout et al.*, 2015]. Surveys are conducted at regular time intervals of either 2.5 or 5 min during a deformation experiment. Each active source survey takes ∼30 s, in the time between all fourteen transducers are switched to passive monitoring mode, allowing the detection and recording of spontaneous fracturing events referred to as Acoustic Emissions (AEs). In preparation for subsequent processing, the data recorded during each survey p are arranged into

an impulse response data cube $\mathbf{D}_p$, with each waveform stored corresponding to S_i in rows, R_j in columns, for P surveys.

In order to ascertain the actual extent of the fracture network formed during triaxial failure, all tested WM samples were scanned before and after experimentation using an X-ray computed tomography scanner. The created data set has a voxel size of 100x100x400 μm.

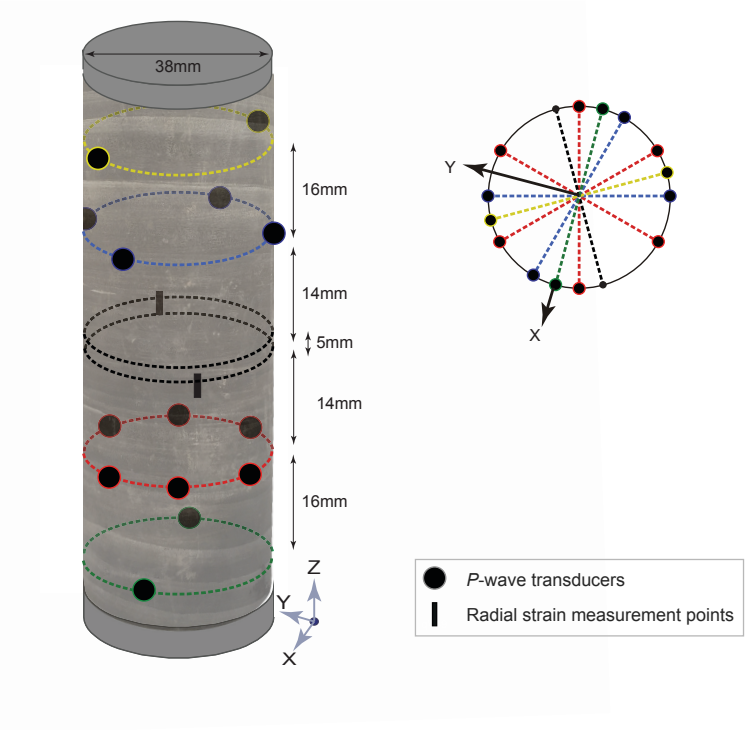

Figure 4.1: *Configuration 14 radially mounted transducers, aligned with the middle of each core sample*

■ 4.2.3 Coda-Wave Decorrelation inversion procedure

This section summaries the theory and inversion workflow applied to the three impulse response data cubes $\mathbf{D}_n$ obtained form the three triaxial experiments. The work by *Larose et al.* [2010] was the first description of what we refer to as Coda-Wave Decorrelation Inversion, in which the formation of a single defect within a concrete block was located, by active source, time-lapse measurements from several ultrasonic receivers. Since this initial publication, other works have applied CWD inversion to monitor the formation of cracks in concrete structures [*Larose et al.*,

2015; *Zhang et al.*, 2016], or study changes due to volcanic [*Obermann et al.*, 2013a] or tectonic [*Obermann et al.*, 2014, 2019] activity. In this work, we apply a linear least-squares inversion method, for the time-lapse monitoring of shale faulting under triaxial stress conditions. The python code developed by *Zotz-Wilson* [2019b] is used for this purpose. For a detailed description of the theory employed, please refer to *Planès et al.* [2015].

The basic premise of CWD is that a change in the scattering properties of a medium can be inferred by a comparison between wavefields recorded before and after the change. This comparison is performed via a normalised cross-correlation, with the measured decorrelation coefficient K^m calculated for a window $[t_k - t_w, t_k + t_w]$ within the coda. Similar to Coda-Wave Interferometry (CWI) which relates the phase shift of this correlation to a change in elastic wavespeed [*Larose and Hall*, 2009; *Payan et al.*, 2009; *Zhang et al.*, 2012b; *Grêt et al.*, 2006b] or temperature [*Grêt et al.*, 2006b; *Weaver and Lobkis*, 2000; *Larose et al.*, 2006] of the medium, CWD relates the corresponding K^m to a change in the scattering properties of the medium. In terms of the processing, for each survey p, the measured decorrelation coefficient K^m_{ij} between a reference survey D_{ref} and perturbed survey D_p, is calculated for each source i and receiver j and non-overlapping window of width $2t_w$ within the coda. The resulting data decorrelation matrix $\mathbf{K}^m_p$ of dimensions $[S_i, R_j, t_k]$ for each survey p, serves as the observed data input to an inversion scheme.

In order to relate each K^m_{ij} for various windows within the coda, to localised changes within the core sample, a theoretical estimation of the decorrelation coefficient $K^T_{ij}(\mathbf{r}, t_k)$ [*Rossetto et al.*, 2011; *Planès et al.*, 2014], due to a change in scattering at location $\mathbf{r}$ is made. In its simplest form,

$$K^T_{ij}(\mathbf{r}, t_k) = \frac{V_0 \sigma_T}{2} Q(S_i, R_j, \mathbf{r}, t_k), \tag{4.2.1}$$

where σ_T is the scattering cross-section of a defect at position $\mathbf{r}$ within background velocity V_0. The sensitivity kernel $Q(...)$ used in this work is that derived by *Rossetto et al.* [2011] as,

$$Q(S_i, R_j, \mathbf{r}, t_k) = \frac{1}{4\pi\mathcal{D}} \left(\frac{1}{s_i} + \frac{1}{r_j} \right) \exp \left[\frac{||S_i - R_j||^2 - (s_i + r_j)^2}{4\mathcal{D}t_k} \right], \tag{4.2.2}$$

where $s_i = ||S_i - \mathbf{r}||$, $r_j = ||R_j - \mathbf{r}||$ and $\mathcal{D}$ is the diffusivity of the medium. This kernel provides a description of the expected sensitivity of a particular sensor arrangement (S_i, R_j,) at elapse time t_k to a perturbation at position $\mathbf{r}$. For the three-dimensional visualisation of each sensitivity kernel between different S_i/R_j pairs, see appendix A.4.S1. The core volume is then discretised into tetrahedra, allowing eq. (4.2.1) to be calculated at the centre of each. A forward problem is then formulated in vector/matrix form as,

$$\mathbf{K}^m_p = \mathbf{G}\mathbf{m}, \tag{4.2.3}$$

where $\mathbf{K}^m_p$ is arranged into a vector of measured decorrelation coefficients at survey p, for each S_i - R_j pair, and correlation window. The matrix $\mathbf{G}$ stores the sensitivity kernels $Q(S_i, R_j, \mathbf{r}, t_k)$ row-wise, calculated at each tetrahedron. The true model

parameters $\mathbf{m}$ is a vector containing the density of σ_T perturbations within each tetrahedron given as σ_{T_ρ} with the dimensions $\mathrm{mm}^2/\mathrm{mm}^3$. A least-squares formulation is adopted [*Tarantola*, 2005], in order to estimate the model parameters $\tilde{\mathbf{m}}$. As σ_{T_ρ} must be positive, an iterative procedure is applied for each $\mathbf{K}_p^m$ by which any negative $\tilde{\mathbf{m}}$ are discarded until convergence is achieved, generally requiring no more than 10 iterations.

In order to make comparisons between each tested sample, we maintain the same relative weights in the inversion miss-fit function. The standard deviation σ_m from the *a priori* model m_{priori} is 0.53, which controls the degree to which the measured data are fitted. The other free parameter in the inversion is L_c which is set to 12.26 for all three tests, and represents the correlation distance between cells. The diffusivity $\mathcal{D}$ in eq. (4.2.2) is assumed to remain constant throughout each test, and is therefore estimated from a single trace selected at approximately 50 % of peak stress by the approach described in *Anugonda et al.* [2001]. This simplification is motivated by the observation of previous applications of CWD [*Zhang et al.*, 2018], that the inversion is relatively insensitive to changes in $\mathcal{D}$.

Additionally, each successive time-step in the inversion p is independent of one another as the initial m_{priori} are set to zero. Therefore, any observed correlations between successive distributions of σ_{T_ρ} are derived from the input data $\mathbf{K}_p^m$. A total of four, non-overlapping 40 µs correlation windows beginning at 50 µs up until 210 µs within the coda are applied. The value of 50 µs is selected as it follows the arrival of maximum S-wave energy, from which point the wavefield shows a diffusive decay in energy. The width of each correlation window must be significantly larger than the dominant period T_0 of the wavefield, while the number of windows must be balanced against computational cost.

The core volume is discretised into a tetrahedral mesh of 3.2 mm characteristic length [*Geuzaine and Remacle*, 2017], resulting in ∼15 000 cells, thereby keeping the computational time low. The model parameters $\tilde{\mathbf{m}}$ resulting from each inversion time-step p are mapped onto the tetrahedral mesh, providing an indication of the spatio-temporal changes in the density of scattering cross-section σ_{T_ρ} with respect to the reference data cube D_{ref}. The reference point is selected towards the beginning of axial stress loading, once confining pressure has been applied, thereby ensuring each ultrasonic transducer is sufficiently coupled to the lateral surface of the WM sample (see fig. 4.1). Furthermore, in all cases a comparison is made between the $\tilde{\mathbf{m}}$ distribution resulting from: (i) a fixed reference comparison (i.e. consecutive correlations between D_{p_i} and D_{ref}); and (ii) the $\tilde{\mathbf{m}}$ distribution resulting from a rolling reference comparison, (i.e. consecutive correlations between D_{p_i} and D_{p_i-N} which lags behind p_i by N surveys). Where large changes in $\mathbf{K}_n^m$ are identified early on during a given deformation experiment, a second D_{ref} is defined in order to avoid large decorrelation and therefore a reduction in sensitivity to subsequent changes [*Zotz-Wilson et al.*, 2019].

4.3 Results

The analysis of the mudstone samples will be presented from highest to lowest water saturation, i.e., 70%, 58% and 28%. For each sample, the distribution of σ_{T_ρ} throughout deformation is compared to the post-failure fracture network as imaged by post-mortem X-ray CT scanning. In order to quantitatively compare the three-dimensional inversion results with the evolution of stress during axial loading, 4 mm spheres are placed within the centre of regions of high σ_{T_ρ}; and the average value of all intersected tetrahedra is calculated for each survey/time step throughout the experiment. This allows direct quantitive comparison of the three-dimensional distribution of σ_{T_ρ} to be compared with the changes in differential stress.

In all cases, rolling reference monitoring is performed to ensure the rate-of-change in σ_{T_ρ} correlates with the fixed reference results, thereby avoiding a spurious correlation after sudden large or prolonged changes in the medium [*Zotz-Wilson et al.*, 2019]. For the samples of lower initial water saturation (58 % and 28 %), two fixed reference points, before and after large changes in σ_{T_ρ} are defined. For the 70 % S_w sample in which only a single large shear fracture formed (fig. 4.2.b), only a single reference point is necessary. For each deformation experiment, we report the evolution of differential stress in time, including the 3 days of consolidation under isotropic stress preceding the axial loading stage.

Depending on the experiment, active source surveys were conducted every 2.3 min or 5 min. No acoustic emissions were detected during the (1.8 min or 4.5 min) period of passive monitoring between each consecutive active survey. Therefore, for the applied strain rate of $1 \times 10^{-7}\,\mathrm{s}^{-1}$, and saturation levels, the Whitby mudstone is considered to produce no AEs of sufficient magnitude to be detected.

Sample of 70 % initial water saturation

For the 70 % sample shown in fig. 4.2.a, an initial increase in σ_{T_ρ} occurs at the base of the main shear fracture (point A in fig. 4.2.b), which was identified from the post-mortem X-ray CT images. The fixed reference changes in σ_{T_ρ} within the region of point A in fig. 4.2.a show an initial increase at 13.75 MPa or 36 % of the peak stress. This initial increase peaks at ∼20 MPa and 90 h, before reducing again until ∼26 MPa at 98 h. This is immediately followed by a second increase, around the onset of non-linear deformation. A third smaller rise occurs at ∼106 h, followed by a smaller reduction up until ∼113 h. A final slight increase in σ_{T_ρ} leading up to peak stress at 37.82 MPa occurs, followed by a slight drop coinciding with the point of failure. This is followed by ∼20 h of slip along the newly formed shear feature(s), during which σ_{T_ρ} shows a gradual increase, plateauing out towards the end of experimentation.

The rolling-reference dashed curve in the region of point A (fig. 4.2.a) provides an indication of the rate-of-change in σ_{T_ρ} between surveys performed 4.22 h apart. This curve shows its largest value at 89 h followed by peaks of reducing magnitude coinciding with the increase noted in the fixed-reference results at 102 h and 108 h. This provides confidence in the fixed-reference distribution of σ_{T_ρ}. At the peak stress, a final larger increase in the rolling reference σ_{T_ρ} curve occurs.

The six snapshots taken at the plain disks • shown in fig. 4.2.a, display the σ_{T_ρ} distribution for both x-z slices (fig. 4.3), and slices parallel to the A-B fracture plane (fig. 4.4). For a movie of these figures covering the entire experiment see appendix A.4.S3. The differences between the first two time-steps ($\bullet_1 - \bullet_2$) in both figures show a localised increase in σ_{T_ρ} towards the base of the main shear fracture (A), with some distribution along the fracture plane. As stress increases, the point of largest σ_{T_ρ} moves further downward along the fracture plane, with the fracture tip also showing a region of increased σ_{T_ρ}, slightly skewed to the right side of the fracture plane, see point B in fig. 4.4. Further, there is a reduction in the distribution around point B and an increase in the extent at the fracture base (point A) before ($\bullet_4 - \bullet_5$) and after ($\bullet_5 - \bullet_6$) failure. The x-z slices (fig. 4.3) also capture the downward movement and increase in σ_{T_ρ} toward the base of the main fracture.

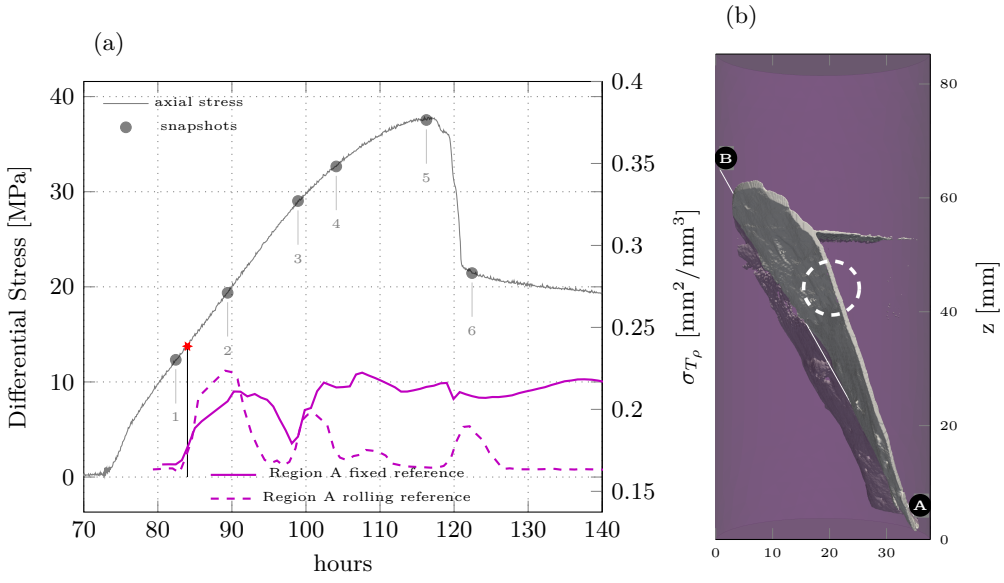

Figure 4.2: *(a) Monitoring of the 70% S_w sample, showing the development in terms of scattering cross-section σ_{T_ρ} (reference at 80 h and the rate-of-change of σ_{T_ρ} (rolling reference lag of 4.22 h) for a 4 mm sampling sphere located at the base of the main shear fracture. The annotated ★ indicates the identified point at which σ_{T_ρ} first localises, while • indicate the snapshots displayed in figs. 4.3 and 4.4. (b) X-Ray post-deformation single shear fracture, with a dehydration fracture plane at ∼55 mm. The dashed region was obscured during X-Ray tomography by a transducer and therefore represents an interpretation. See appendix A.4.S2 for an isometric view rotation of the fracture network.*

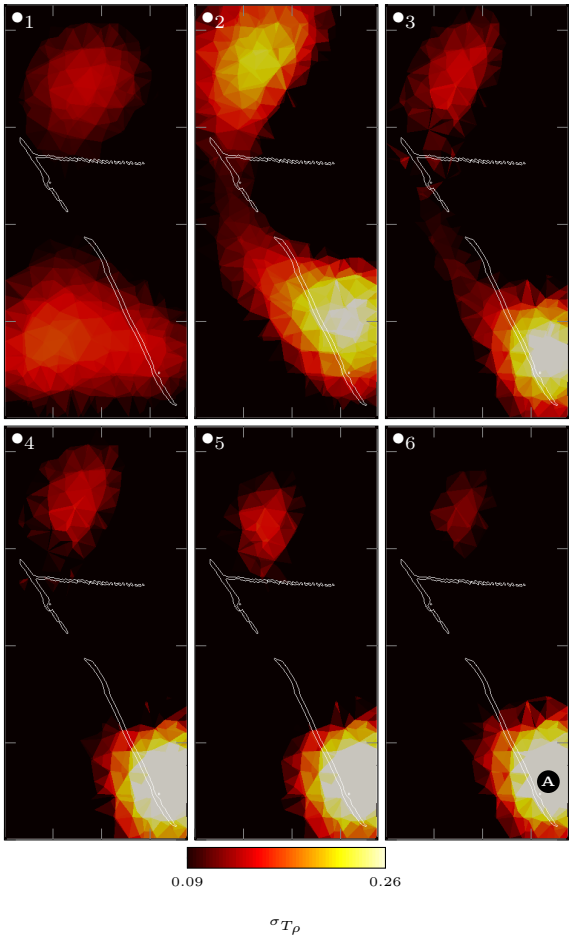

Figure 4.3: *The 70% S_w sample sliced along the x-z plane for time steps $\bullet_1$ to $\bullet_6$ as indicated by the $\bullet$ symbols in fig. 4.2.a. Point A indicates the position of the* 4 mm *sampling sphere at t_6. See appendix A.4.S3 for a movie of this figure.*

Sample of 58 % initial water saturation

The 58 % sample shows two shear fractures. The main fracture extends from the lower right (A) of the x-z slice, up until ∼58 mm on the left (B) as shown in fig. 4.5.b. The smaller fracture extends from the approximate centre of the x-z slice (C), up until ∼35 mm (D). The CWD inversion results indicate an initial increase in σ_{T_ρ} within the upper end of the minor fracture (region D), peaking at ∼100 h, see fig. 4.5.a. The distribution of this initial increase is captured at the ▲ snapshots, shown in fig. 4.6, or as a movie in appendix A.4.S4. Between $\blacktriangle_1 - \blacktriangle_3$ upward drift

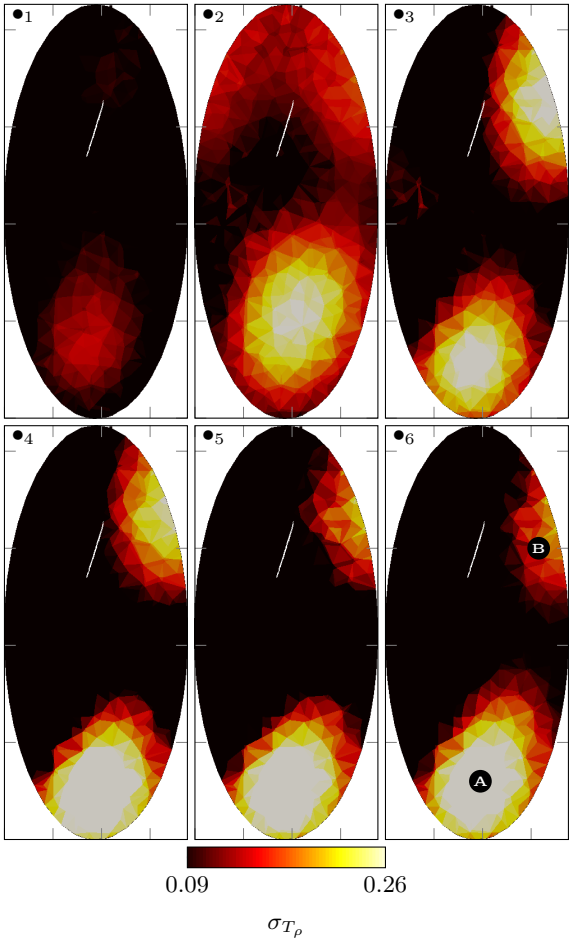

Figure 4.4: *The 70% S_w sliced parallel to the fracture plane A-B, for time steps $\bullet_1$ to $\bullet_6$ as indicated by the $\bullet$ symbols in fig. 4.2.a. Point A indicates the position of the sampling sphere at t_6, while point B shows the position of the maximum σ_{T_ρ} around the fracture tip. See appendix A.4.S3 for a movie of this figure.*

in the location of maximum σ_{T_ρ} occurs, followed by an increase in both magnitude and spatial distribution from $\blacktriangle_4$-$\blacktriangle_5$. The final snapshot ($\blacktriangle_6$) shows the subsequent reduction in magnitude and spatial distribution. Just prior to the peak σ_{T_ρ} noted at 98 h along the minor fracture (region D curve in fig. 4.5.a), an increase occurs at both the base (region A curve) and tip (region B curve) of the major fracture. The six ■ snapshots shown in fig. 4.7 indicate a progressive increase in σ_{T_ρ} towards the major fracture tip (B), continuing all the way to peak stress at 51.29 MPa. The x-z sliced

distribution reflecting the • snapshots generated from a reference at 90 h (fig. 4.8) show a process by which the region of largest σ_{T_ρ} alternates between the minor (D) and major fracture (A) regions (•$_1$-•$_4$), and then focuses at the main fracture just prior (•$_5$) to, and after (•$_6$) the point of dynamic failure. See appendix A.4.S5 for a movie of both the x-z and major fracture slice.

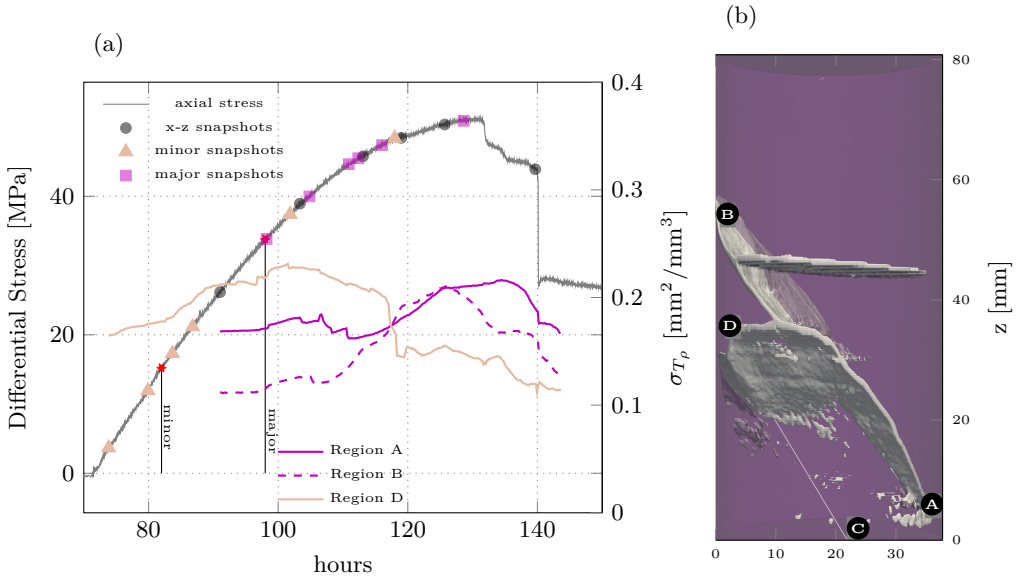

Figure 4.5: *(a) Monitoring of the 58% S_w sample, showing the development in terms of scattering cross-section σ_{T_ρ} for three* 4 mm *spheres located within the minor and main shear fractures. The annotated ★ indicates the identified point at which σ_{T_ρ} first localises, while •, ▲, and ■ indicate the snapshots displayed in figs. 4.6 to 4.8. (b) X-Ray post-deformation major (A-B) and minor (C-D) shear fractures, with a preexisting dehydration fracture plane at ∼45 mm. See appendix A.4.S2 for an isometric view rotation of the fracture network.*

Sample of 28 % initial water saturation

The 28 % sample post-deformation fracture network consists of one large shear fracture, traversing from the lower left to right of the x-z slice (A-B in fig. 4.9.b), with preexisting dehydration fracture planes at the bottom (E) and two at the top (F) of the core. Around the base of the large fracture (A), several smaller fractures coalesce into a single fracture (C-D in fig. 4.9.b). Careful inspection of the post deformation X-Ray scans indicates several smaller fractures, most of which are on one side of the main shear fracture, though there also exists a smaller fracture which

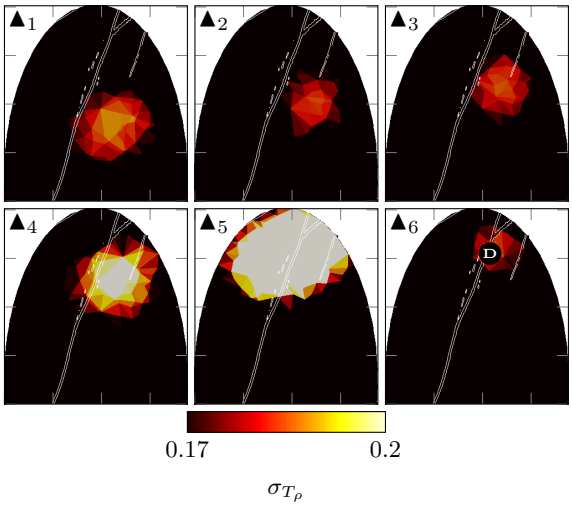

Figure 4.6: *The 58% S_w sample sliced along the minor fracture plane C-D, for time steps $\blacktriangle_1$ to $\blacktriangle_6$ as indicated by the ▲ symbols in fig. 4.5.a. Point D indicates the position of the* 4 mm *sampling sphere at t_6. See appendix A.4.S4 for a movie of this figure.*

originates from two conical low-density heterogeneities (E) at the base of the core. Furthermore, the dashed region in fig. 4.9.b from the base of the core up until the lower dehydration fracture at E, was damaged during testing and subsequently this region fell off when the core was extracted from the pressure vessel. For the first ∼10 min of experimentation the applied strain rate is $1 \times 10^{-6}\,\mathrm{s}^{-1}$ up until 7 MPa, after which it is corrected to $1 \times 10^{-7}\,\mathrm{s}^{-1}$ for the remainder of the test. During this period of increased strain rate, in the centre region of the minor fracture (C-D) an increase in σ_{T_ρ} occurs, the spacial distribution of which is captured at the ■ snapshots indicated in fig. 4.9 and displayed in fig. 4.10. For a movie of both figures see appendix A.4.S6. While the first two time-steps $\blacksquare_1$ - $\blacksquare_2$ show almost the same distribution, the third $\blacksquare_3$ indicates an increase in magnitude and upward movement. This is then followed ($\blacksquare_4$ - $\blacksquare_6$) by an increase in distribution and magnitude. Shortly afterwards a subsequent reduction in σ_{T_ρ} occurs. In order to improve sensitivity to subsequent changes, a reference point at 105 h is selected. The results from this redefined reference show an increase in σ_{T_ρ} within a region coinciding with the two low-density heterogeneities (E), and in a region around the upper dehydration fractures (F). See the • snapshots indicated in fig. 4.9 and displayed in fig. 4.11. For a movie of both figures see appendix A.4.S7. This centre of maximum σ_{T_ρ} around E moves downward as it increases ($\bullet_1$ - $\bullet_3$), up until 130 h, at which point a gradual reduction begins. During $\bullet_1$ - $\bullet_3$ we also note a region of increasing σ_{T_ρ} around the upper dehydration fracture F. After peak stress is reached at ∼167 h a rapid redistribution of σ_{T_ρ} over the main fracture plane occurs (Region A curve in fig. 4.9.a),

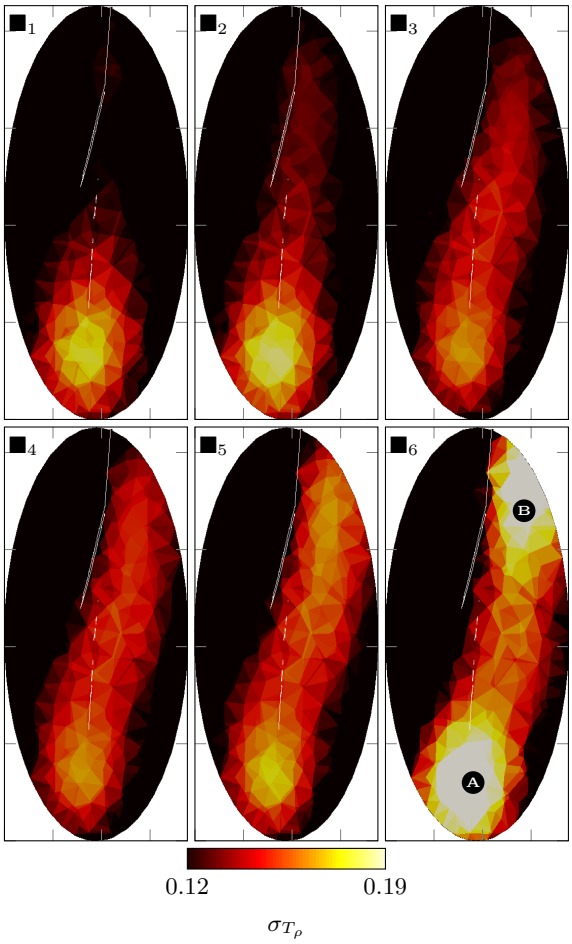

Figure 4.7: *The 58% S_w sample sliced along the fracture plane A-B, for time steps* ■$_1$ *to* ■$_6$ *as indicated by the* ■ *symbols in fig. 4.5.a. Points A and B indicate the position of the* 4 mm *sampling sphere at* t_6. *See appendix A.4.S4 for a movie of this figure.*

which increases post-failure, between •$_5$ and •$_6$. This re-activation of the region surrounding the main fracture plane is spatially captured by the □ snapshots shown in fig. 4.12 and movie in appendix A.4.S7, which shows minimal increase between □$_1$ and □$_2$ prior to peak stress, followed by increased distribution □$_3$ – □$_6$ after failure.

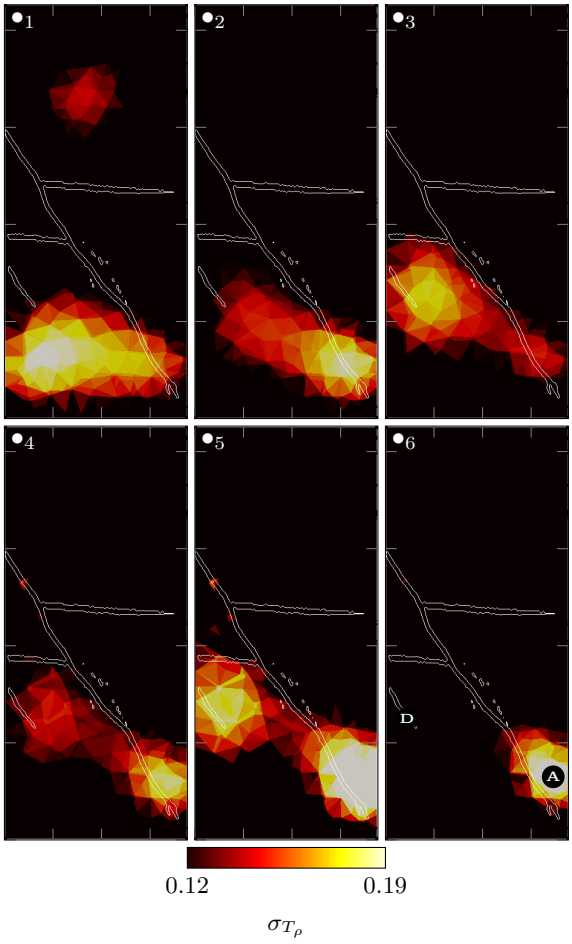

Figure 4.8: *The 58% S_w sample sliced along the x-z plane for time steps $\bullet_1$ to $\bullet_6$ as indicated by the $\bullet$ symbols in fig. 4.5.a, and a reference at* 90 h. *Points A and D indicate the position of the* 4 mm *sampling spheres at* t_6. *See appendix A.4.S4 for a movie of this figure.*

Comparative analysis

For each of the samples of varying initial S_w, an initial increase in σ_{T_ρ} is determined, based on the criterion of an increase in both its rate-of-change and spatial focus. This point is marked in figures figs. 4.2, 4.5 and 4.9 by a ★. For both the 70 and 58 % S_w samples an increase in localised σ_{T_ρ} is found at ∼14 MPa, while for the 28 % S_w this occurs at 6.5 MPa, see fig. 4.13. Additionally, we identify a negative correlation between S_w and the peak differential stress achieved during each test.

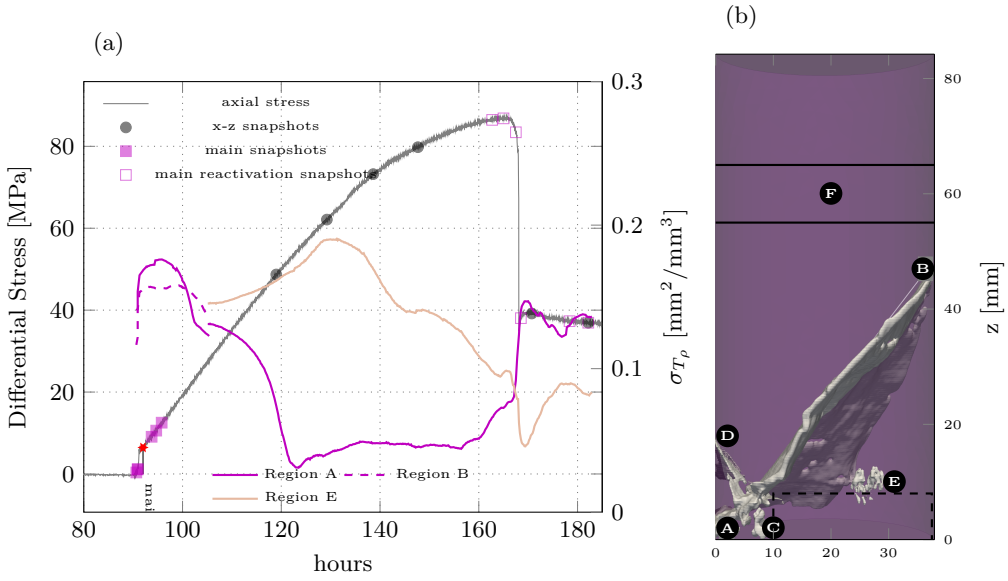

Figure 4.9: *(a) Monitoring of the 28% S_w sample, showing the development of σ_{T_ρ} at the base and tip of the main fracture, and in a region surrounding the high-density impurities. Note the dashed, Region B curve is only shown for the fixed-reference distribution at the beginning of the stress increase. The annotated ★ indicates the identified point at which σ_{T_ρ} first localises, while ●, ■, and □ indicate the snapshots displayed in figs. 4.10 to 4.12. (b) X-Ray post-deformation major (A-B) and minor (C-D) shear fractures, with preexisting dehydration fracture planes above and below F, and below E. Two low-density impurities present in the sample are indicated at point E. The dashed regions below E was damaged during testing, and therefore was not present during X-Ray tomography. See appendix A.4.appendix A.4.S2 for an isometric view rotation of the fracture network.*

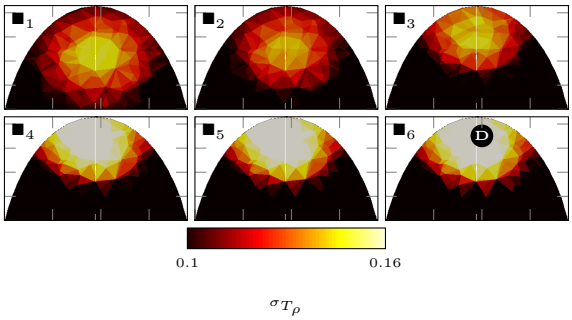

Figure 4.10: *The 28% S_w sample sliced along the minor fracture plane C-D, for time steps* ■$_1$ *to* ■$_6$ *as indicated by the* ■ *symbols in fig. 4.9. Point D indicates the position of the* 4 mm *sampling sphere at* t_6*. See appendix A.4.S6 for a movie of this figure.*

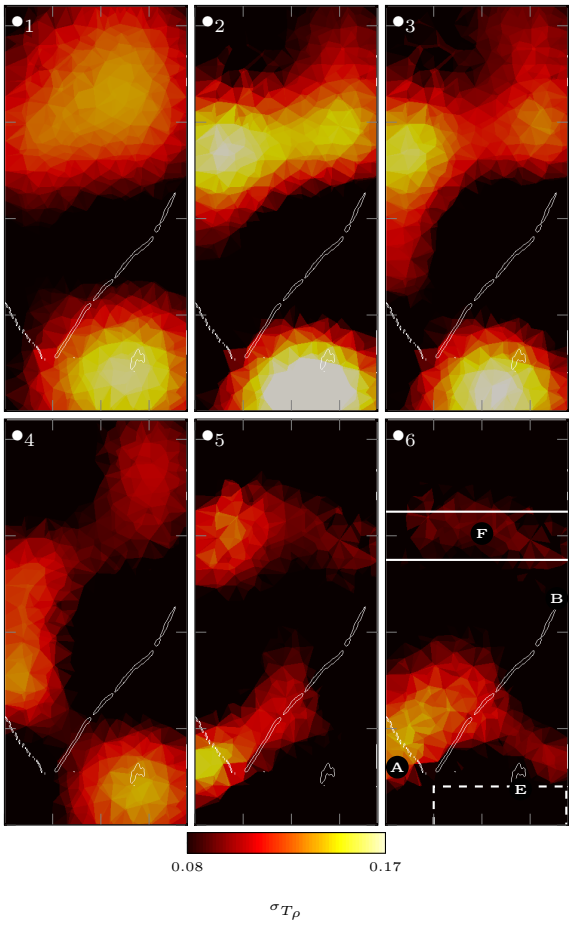

Figure 4.11: *The 28% S_w sample sliced along the x-z plane for time steps $\bullet_1$ to $\bullet_6$ as indicated by the $\bullet$ symbols in fig. 4.9. Points A and E indicate the position of the 4 mm sampling spheres at t_6. Point F indicates the dehydration planes; point E the low-density inhomogeneities; and B the main fracture tip. See appendix A.4.S7 for a movie of this figure.*

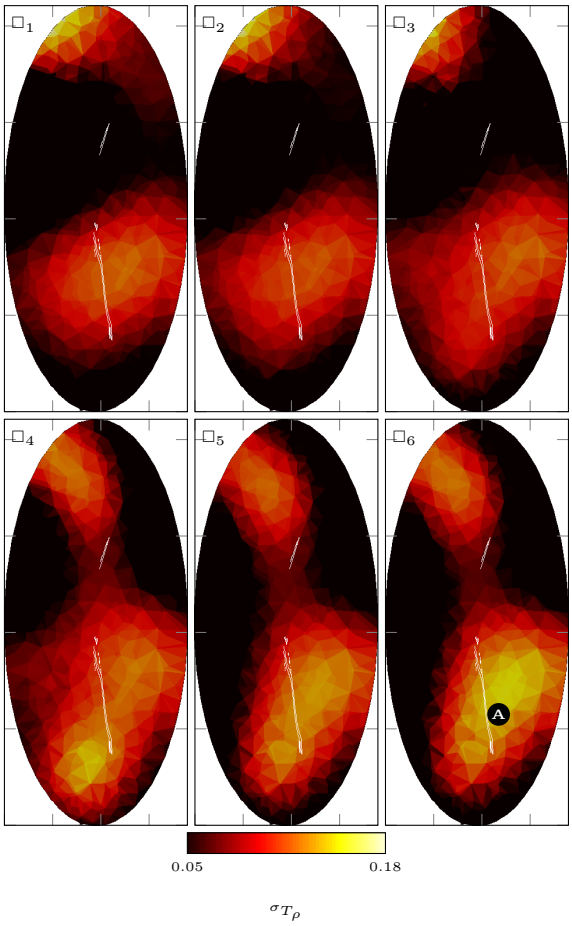

Figure 4.12: *The 28% S_w sample sliced along the main fracture plane A-B, for time steps $\square_1$ to $\square_6$ as indicated by the $\square$ symbols in fig. 4.9. Point A indicates the position of the* 4 mm *sampling sphere at t_6. See appendix A.4.S7 for a movie of this figure.*

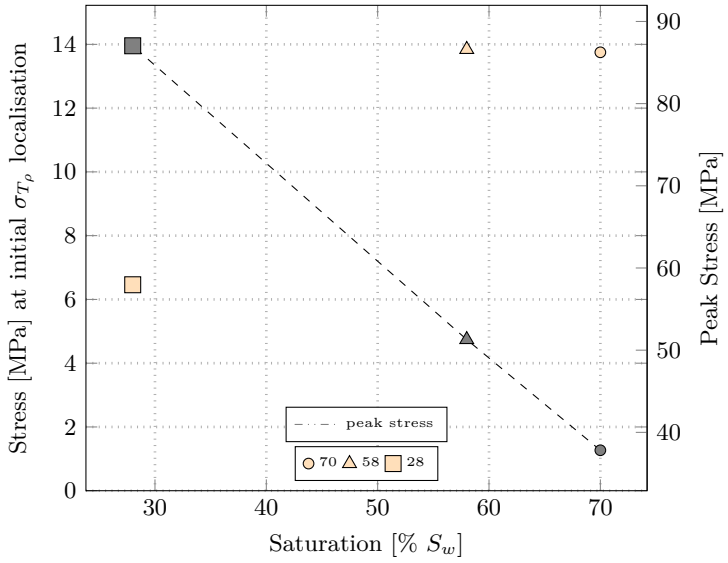

Figure 4.13: *Comparison between the interpreted onset of localised inelastic strain on the left axis, and differential peak stress on the right axis, vs initial water saturation of each core sample.*

4.4 Discussion

■ 4.4.1 The development of the fracture network as interpreted from the distribution of scattering cross-section

The application of CWD inversion in monitoring the triaxial deformation of three mudstones of varying initial water saturation, indicates progressive and repeated re-distribution of inelastic strain within the rock following strain localisation events. Here we define microscopic inelastic strain as associated with closure, opening or shearing along microscopic fractures, while macroscopic inelastic strain refers to the coalescence of microscopic cracks into a large shear fracture. A region of increased σ_{T_ρ} indicates initial localised microscopic inelastic strain and eventually the formation of macroscopic fractures. An increase in spatial distribution indicates the growth of a cracked region, while the increase in magnitude of σ_{T_ρ} indicates either an increase in the crack density and/or an increase in the impedance contrast between the cracks and the rock matrix, which can be interpreted as a change in the aperture of the cracks/fractures.

For the most saturated sample there are three stages of increase, followed by a decrease in σ_{T_ρ} at the base of the main shear fracture (point A in fig. 4.2.b). This suggests initial localised strain occurs, which is subsequently closed as the stress is reduced and redistributed throughout the rest of the sample. The reactivation of the same region and the increase in both the distribution (spatial extent) and magnitude of σ_{T_ρ} suggests an increase occurs in the width, and aperture of the fracture, respectively. This is evident when viewing the slice along the fracture plane (fig. 4.4 or the S.3 movie), where only after reactivation at 98 h ($\bullet_3$) does the spatial distribution of σ_{T_ρ} notably increase at both the base (A) and tip (B) of the fracture. The subsequent reduction in σ_{T_ρ} distribution at the tip (B) and increase at the base (A) before ($\bullet_4 - \bullet_5$), and after ($\bullet_5 - \bullet_6$) failure, indicates that the fracture plane grows laterally at the base while the tip closes up. Further, the observed reduction in the maximum rate-of-change in σ_{T_ρ} over the first three activations at the fracture base (dashed curve in fig. 4.2.a) suggests a linear reduction in the rate at which the micro/macroscopic fractures open.

The distribution of σ_{T_ρ} during the 58 % S_w test also displays a process of continuous re-distribution of stress, though in this case between a region corresponding to the minor (C-D) and major (A-B) fractures in fig. 4.5.b. Initially, in a region surrounding the minor fracture (C-D) at ∼82 h, we interpret the formation of microscopic inelastic strain. Growth occurs in both magnitude and distribution at ∼89 h (see $\blacktriangle_4$ in fig. 4.6 or S.4 movie), indicating larger scale coalescence occurs at this point. At 98 h, the main fracture appears to initiate, from the base (A) towards the tip (B), and eventually fails the sample. Throughout the test we identify approximately four stages of redistribution in σ_{T_ρ} (see $\bullet_1 - \bullet_4$ in fig. 4.8 or S.5 movie) between the minor and major fracture. This is interpreted as several stages of opening and closure of initially microscopic and eventually macroscopic fractures, as stress redistribution occurs.

The sample with the lowest initial water content (28 %S_w) with its major (A-B in fig. 4.9.b), and minor (C-D) fractures, show a similar process of re-distribution of

σ_{T_ρ}. However, a notable difference with this sample is the presence of the two low-density, approximately conical heterogeneities (region E in fig. 4.9.b) at the lower end of the core. These are interpreted as the void left by the exoskeleton of gastropods such as the Neptunea contraria [*Linnaeus*, 1771]. The distribution of σ_{T_ρ} supports an interpretation where initially the minor fracture (C-D) experiences localised strain at the base of the core, during the initial region of increased strain-rate, see snapshots ■ in (fig. 4.10) or S6 movie. This is followed by gradual prolonged fracturing of a large region surrounding the low-density impurities, see $\bullet_1 - \bullet_4$ in fig. 4.11 or the S.7 movie. Subsequently, the major shear fracture (A-B) develops ($\square_4 - \square_6$ in fig. 4.12 and $\bullet_5 - \bullet_6$ in fig. 4.11 or the S.7 movie) close to the peak stress, and the failure of the sample. This interpretation is supported by the fact that the region surrounding the interpreted marine exoskeletons (E) was fractured to the point that it fell off the end of the sample once removed from the pressure vessel. Additionally, the concentration in σ_{T_ρ} between the two preexisting dehydration fractures (F), particularly between $\bullet_2 - \bullet_3$ in fig. 4.11, indicates that either a change in compliance occurs over these interfaces, or microscopic changes occur within the region between them (a layer of different mineralogy or microstructure).

In summary, for all tested samples the identified localisation in σ_{T_ρ} was found early on during deformation, between 7 % and 36 % of the peak differential stress. We therefore interpret this initial localisation in σ_{T_ρ}, not as the formation of macroscopic coalesced shear fractures but primarily driven by distributed intergranular opening, closure, and shearing at the microscopic scale. A similar conclusion was reached in a recent study by *McBeck et al.* [2018] on the Green River shale, during which core samples were time-lapse imaged by X-Ray microtomography while under confining pressure. The identification of localised strain regions became apparent at 35 % of the peak differential stress, preceding macroscopic shear failure. This value is consistent with the upper limit of the range reported here. Further, *McBeck et al.* [2018] also demonstrate that microscopic opening, closure, and shearing work together to eventually produce macroscopic shear failure. Their observations support our interpretation of a complex timeline of locally increasing (opening or shearing) and decreasing (closure of micro/macroscopic fracturing) σ_{T_ρ} up until failure.

■ 4.4.2 The impact of water saturation

The Whitby mudstone plugs display an increase in strength and a reduction in plasticity with a reduction in water saturation. The primary mechanism driving these changes is expected to be an increase in the capillary suction within the pore space of the mudstone [*Erling et al.*, 2008; *Ramos da Silva et al.*, 2008]. As the pore-fluid evaporates from the mudstone, a reduction in the pore-pressure occurs, leading to a tensile stress or negative pressure, and finally a change in compliance (or stiffness) between individual grains [*Onaisi et al.*, 1994; *Forsans and Schmitt*, 1994; *Ewy*, 2014]. This ultimately leads to an increase in the strength and a reduction in the plasticity of the material. Our experimental results corroborate this relationship which has been recently confirmed for the Whitby [*Douma et al.*, 2019] as well as other mudstones [*Vales et al.*, 2004; *Ramos da Silva et al.*, 2008; *Ghorbani et al.*, 2009]. Furthermore, the comparison between the identified onset of inelastic strain

(microscopic damage), and initial water saturation suggests a non-linear relationship, see fig. 4.13. However, this may be also due to the added inhomogeneity of the low S_w sample (the low-density heterogeneity), or the higher initial strain-rate, and therefore more measurement points are required to statistically validate this argument.

As no AEs were detected during passive monitoring of the samples, this suggests that the brittle failure necessary to generate AEs is insufficient [*Main*, 1990] to overcome the environmental noise.

■ 4.4.3 CWD: An effective real-time fracture monitoring tool

This study on samples from the WMF indicates that CWD inversion has the potential to image the initiation, propagation and branching of fractures or other heterogeneities, tested under realistic subsurface conditions (stress, pressure, temperature). While there are several other techniques which provide spatio-temporal information on inelastic strain at in-situ conditions, they often require substantial investment in equipment and post-processing, or are inherently less sensitive to subtle localised microscopic changes.

Time-lapse synchrotron micro-tomography undoubtedly provides the highest spatial resolution, as it is able to resolve the detailed structure of macroscopic fractures [*Renard et al.*, 2017, 2018], and microscopic strain localisation through digital volume correlations [*Kandula et al.*, 2018; *Mao et al.*, 2019; *Mao and Chiang*, 2016; *McBeck et al.*, 2018]. The main limitation of this method is that it requires access to an X-ray beam in a synchrotron of sufficient energy to image a sample housed within a bespoke pressure vessel. Further, the maximum sample size is strictly constrained by both the spatial and temporal resolution requirements.

Traditional acoustic imaging methods such as velocity tomography, while more affordable, and able to provide sufficient spatiotemporal resolution to resolve the region around macroscopic fractures [*Jansen et al.*, 1993; *Brantut*, 2018; *Aben et al.*, 2019], have not shown sensitivity to microscopic inelastic strain localisation.

Passive AEs monitoring is a well established technique in experimental rock mechanics, and with a sufficiently accurate velocity model provides a spatio-temporal indication of the occurrence of brittle failure [*Lei et al.*, 2004; *Aben et al.*, 2019; *Brantut*, 2018; *Jansen et al.*, 1993; *Sarout et al.*, 2017]. However, as demonstrated by this study on the WMF, AEs monitoring relies on the existence of seismicity of sufficient magnitude and frequency to be detected by the available sensor network. For clay- or calcite-rich rocks, where inelastic deformation can develop in a plastic, relatively silent fashion [*Peng and Yang*, 2018], AEs monitoring is a less suitable method to determine the onset of inelastic strain. Further, both active and passive monitoring methods require time consuming pre-processing steps, such as first arrival picking, and the construction of a velocity model, thereby limiting their utility in real-time monitoring.

In summary, CWD inversion monitoring requires little to no additional investment in equipment where acoustic monitoring is already available. Further, it is more sensitive to subtle changes in scattering or velocity than methods which rely on the coherent arrivals [*Zotz-Wilson et al.*, 2019], and once appropriate inversion pa-

rameters are determined for a particular lithology and receiver arrangement, quasi-real-time monitoring is feasible. While CWD inversion cannot provide the same spatial resolution as synchrotron micro-tomography, it appears to demonstrate similar sensitivity to the onset of microscopic inelastic strain.

4.5 Conclusion

The CWD inversion monitoring of the Whitby mudstone during triaxial compaction, indicates that the formation of inelastic strain localisation occurs at less than 36 % of peak stress. The AEs monitoring indicates that these inelastic processes occur mostly through plastic deformation, while the comparison of different S_w suggests a non-linear relationship with the onset of strain localisation. In general, the application of CWD inversion to what is ostensibly an aseismic mudstone, has enabled a qualitative discussion of the time and location at which initial microscopic inelastic strain (opening, closure, and shearing) develops. Furthermore, subsequent stages of reactivation and eventual macroscopic shear failure are discernible.

Acknowledgments

We would like to thank David Nguyen and Stephen Frins at CSIRO's Geomechanics and Geophysics Laboratory, for their assistance during the experimentation. The assistance provided by Joost Van Meel at TUDelft in post processing the CT-scans is also much appreciated. Further, the funding provided by the Dutch Upstream Gas top-sector initiative (project TKIG01020) and our industry partners EBN B.V., Engie E&P NL B.V., Wintershall Noordzee B.V., and Baker Hughes NL B.V. is acknowledged. Furthermore, we would like to acknowledge the use of the open-source python module pyVista [*Sullivan and Kaszynski*, 2019], which is used to visualise all of the 3-D fracture networks, and CWD inversion results.

5

Conclusions and recommendations

In this final chapter a summary of the major findings and conclusions of this thesis are presented. This is followed by specific recommendations addressing the three research objectives outlined in section 1.4. Finally, a general research framework is recommended with the aim of developing coda-wave derived, truly precursory early warning systems.

5.1 Conclusions

■ 5.1.1 Conclusions from chapter 2

In chapter 2, the issue of excessive decorrelation when performing interferometry between a reference and a perturbed material state is discussed. For a continuously evolving medium, failure to ensure sufficient similarity between material states, will eventually result in a spurious correlation, and therefore the loss of sensitivity to change. Due to the serially correlated nature of geophysical time-series, estimating the statistical significance of such a correlation is not a trivial problem, with various approaches suggested over the past few decades [*Zwiers*, 1990; *Ebisuzaki*, 1997; *Hanson and Yang*, 2009]. This principle is experimentally demonstrated by a fixed reference comparison during the ultrasonic monitoring of an initially unstressed sandstone core. As uniaxial stress increases, a rapid loss of correlation occurs, with both CWI and CWD displaying insufficient sensitivity to determine the onset of inelastic deformation. While previous practitioners have opted to manually update the reference when a decay in sensitivity is observed, doing so represents a discontinuity in the quantity of interest. This has issues in terms of both one's ability to interpret the data, and in a monitoring sense, the timeliness and robustness of the system to environmental changes. As a result, its utility within early warning detection systems is reduced. As an alternative, this chapter demonstrates that through the choice of a rolling reference, both CWI and CWD are able to monitor the evolution of a material in terms of the relative velocity change $[\delta v/v]^{roll}_{sum}$ and

the rate-of-change in the scattering coefficient $K(|\dot{g}_0|)$. Furthermore, precursory indicators are determined from the trend lines of both the $[\delta v/v]^{roll}_{sum}$ and $K(|\dot{g}_0|)$, to the classically determined material yield-point. These coda-derived methods are compared with changes in the Time-Of-Flight $[\delta v/v]_{TOF}$ of the first arrivals, which for three samples and two different lithologies shows no precursory indication to the yield-point. In summary, within experimental rock mechanics the use of rolling-reference coda-wave monitoring enables the continuous evolution of both sample velocity and scattering power to be determined, and in turn provides for improved characterisation of different lithologies under various perturbations. Furthermore, it is suggested that outside the confines of this study, this simple modification, in combination with active-source monitoring, is well suited to early warning detection systems. In particular, applications where the likelihood of failure is low and the severity is sufficiently high to justify investment in active source infrastructure. Possible applications discussed are structural health monitoring of critical infrastructure, such as dams, bridges, and nuclear reactors, or environmental hazard monitoring of landslide, mudslides, or volcanoes.

■ 5.1.2 Conclusions from chapter 3

In chapter 3, coda-wave derived monitoring methods are applied to track the changes in material properties during the pore-pressure depletion of samples from the seismogenic Groningen gas field. Either linear continuous, or cyclical depletion is applied, beginning at pre-production reservoir pore-pressure of ∼35 MPa, and moving towards maximum depletion of 3 MPa. In addition to the active source ultrasonic monitoring, detailed micro-structural analysis of pre and post depletion samples is conducted, along with Acoustic Emissions (AE) monitoring on a single sample. Both CWI and CWD are applied, as well as MLTWA in order to determine the relative changes in scattering ${}^{Sc}Q^{-1}$ and intrinsic ${}^{I}Q^{-1}$ attenuation. The combination of all these data, with the theory of elastic wavefield propagation within fluid-saturated porous media [*Biot*, 1956], enables insight into the evolution of grain scale compaction. Within the context of the research objectives of this thesis, this chapter works towards improved characterisation of inelastic deformation within experimental rock mechanics. A summary of the main conclusions of this chapter are:

- The proportion of inelastic strain due to pore-pressure depletion does not progressively increase, but occurs in serial stages of predominantly intergranular closure, transitioning into predominantly intergranular slip/cracking. With continued depletion, and a suitably weak grain structure, the pervasive formation of intra/transgranular cracks is expected. These findings are supported by a conceptual model, as related to the high-frequency Biot-type viscous resistance to fluid flow.
- Samples with high initial porosity $\phi_0 > 27\,\%$, display a total increase in ${}^{I}Q^{-1}$ suggesting that intragranular cracking of the grains dominates over the total closure of preexisting cracks. This is in contrast with the observed total relative reduction in ${}^{I}Q^{-1}$, noted for samples of lower ϕ_0, suggesting that the total

closure of crack space dominates. These findings are strongly supported by literature.

- The identification of a transition from the reservoir coring pressure to virgin pore-pressure is identifiable within the acoustic response of the core. Specifically, an increase in $K(|\dot{g_0}|)$ is clearly identifiable, indicating an increase in the rate-of-change of the scattering power g_0 of the medium. Further, this transition is also marked by a stabilisation in the reduction of ${}^{I}Q^{-1}$ for samples $\phi_0 < 27\%$ and an increase for those $\phi_0 > 27\%$. This suggests an increase in crack density occurs within this region. These points are further supported by a three-fold increase in the rate of AE per strain as virgin pore-pressure is reached.

In addition to the immediate implications on the grain-scale processes, further discussion is provided on the associated implication to both the development of geomechanical models, and the feasibility of field scale monitoring.

5.1.3 Conclusions from chapter 4

In chapter 4, three Whitby mudstone core samples of different initial water saturation are triaxially compacted over a period of days. The acoustic response is monitored via both active ultrasonic, and passive AE with a network of receivers. From the impulse response of each active survey, CWD inversion is performed enabling the localisation and evolution of scattering cross-section σ_T changes in three dimensions throughout compaction. Analysis of these data for all samples, indicates that at less than 36 % of peak stress the onset of localised inelastic strain occurs, which correspond with the post-deformation X-ray images of the fracture network. These localised changes are followed by several stages of redistribution and reactivation up until, and after failure. This indicates that the evolution from microscopic to macroscopic fracturing is not a process of continuous development, but occurs in serial stages of reactivation. Importantly, in all experiments, no AE were detected, which suggests that these clay-rich mudstones deform mostly plastically, and therefore the study of fracture formation cannot rely on AE monitoring. In summary, this chapter demonstrates that through CWD inversion of an aseismic mudstone, the qualitative analysis of the time and location at which initial fracturing and growth occur, is possible. This has important implications on the study of samples under in-situ conditions, as it provides a highly sensitive imaging method, which requires little additional investment where acoustic equipment already exists.

5.2 Recommendations and outlook

The use of coda-wave derived monitoring methods have gained in popularity within the geophysics and NDT communities, particularly over the past decade. However, the application of these techniques within operational monitoring systems is a work in progress. Additionally, there are unexplored opportunities for the use of such methods within experimental rock-mechanics laboratories. In line with the objectives of this thesis as outlined in section 1.4, the following recommendations are

separated into three main areas; (i) the advancement of the utility of coda-wave derived monitoring methods (section 5.2.1); (ii) the improved understanding of the relationship between material property changes through the lens of the coda-wave (section 5.2.2); (iii) the development of coda-wave derived imaging as a tool to investigate inelastic changes within laboratory testing.

This section will conclude with a discussion of a possible research approach, with the aim of developing truly precursory, robust Early Warning Systems (EWS) through coda-wave monitoring.

■ 5.2.1 The utility of coda-wave derived monitoring methods

Where one wishes to employ the sensitivity benefits of the coda-wave within the operational monitoring of either long-term transient, or sudden large changes in a certain material quantity, three main requirements should be met:

- A repeatable source. The decision to use ambient noise interferometry, should only be made in scenarios where this does not come at the cost of the sensitivity of the monitoring system, or the stability of the system to environmental changes. Where possible, active source monitoring is the preferred choice, as it enables the design of the system to be optimally sensitive to the expected changes in material properties.

- The use of a rolling-reference waveform should be made where cross-correlations between successive measurements throughout monitoring are performed. This choice removes the associated ambiguity of selecting a fixed reference point, while ensuring the monitoring system does not result in a spurious correlation.

- The repeat measurement period must be sufficiently small such that it is able to resolve the maximum expected rate-of-change in the material quantities of interest.

It is suggested that through the careful consideration of these requirements, the feasibility of using the coda-wave within operational monitoring systems is greatly improved.

■ 5.2.2 Phenomenological observations through the coda-wave lens

On a very basic level, this thesis should provide significant motivation to all experimental rock-mechanics laboratories, to make coda-derived monitoring a standard part of their experimentation. This represents little-to-no additional investment for those who already apply P and S-wave velocity monitoring, however further research is required into the response of the coda-wave under different inelastic, grain scale processes.

In rock mechanics, there are essentially two components of investigation; (i) experimentation which aims to characterise samples through repeat measurements, thereby building statistical significance; and (ii) theoretical/numerical modelling which works from first principles to model these processes. As in many technical

fields of research, one cannot do without the other, since there must exist a continuous process of cross-check between the two. Therefore, in order to get the most out of coda-wave monitoring within experimental rock mechanics, advances must be made in the theoretical description of the expected physics of wavefield propagation through the grain structure. It is therefore recommended, that efforts are made to unify numerical modelling of grain-scale fracture formation, with wavefield propagation. This would enable better comparison between the experimentally observed coda-wave signature, and the evolution of changes at the grain-scale. An example of numerical modelling of poroelastic wavefield propagation is the thesis of *Blanc* [2014], which if unified with fracture formation models [*Gao et al.*, 2016] would be a first step in this direction.

5.2.3 Towards improved coda-wave derived imaging of change

The ability of CWD inversion to image the change within a medium is defined by the closeness that the employed sensitivity kernels approximate the diffusive propagation of energy within. The quality of these kernels, for a particular monitoring application, is therefore a crucial component governing the success of CWD inversion. In recognition of this, recent efforts have focused on either the derivation of kernels to include single scattering effects [*Margerin et al.*, 2016; *Nakahara and Emoto*, 2017], or the influence of boundary conditions through numerical modelling of the diffusive transport of energy [*Kanu and Snieder*, 2015; *Xue et al.*, 2019]. In this thesis the kernels used to locate change within the laboratory core assume that diffusive energy propagates within a homogeneous, infinite medium. Therefore the effects of the core boundary geometry, and in-situ heterogeneity are neglected. In order to improve the application of CWD inversion towards imaging fracture formation within the laboratory setting, it is recommended that efforts are made to numerically calculate the diffusive kernels within the core. A favourable workflow to achieve this would be:

- To firstly build a velocity/density model of the core from the pre-deformation X-ray, and Magnetic Resonance Imaging (MRI) scans. This would allow both the layered nature of lithology such as mudstones, and any large heterogeneities to be included into the diffusive approximation of energy transport.

- Secondly the numerical modelling of diffusive energy transport within the constructed velocity/density model is required. This must be undertaken for each source - receiver pair available within the experimental setup, thereby enabling the constructions of numerically determined sensitivity kernels which include the pre-deformation structure of the core sample.

All subsequent processing steps remain essentially unchanged, as the numerically determined kernels simply replace those which were analytically determined. An advantage of this approach is that the selection of window positions would not have to be constrained to the coda-wave where diffusive propagation occurs, as numerical modelled kernels includes the single scattering intensity [*Margerin et al.*, 2016].

■ 5.2.4 Towards truly precursory early warning systems

The vast majority of Early Warning Systems (EWSs) to material changes can be classified as passive, since they are only sensitive to a perturbation which is observable at the boundary of the region of interest. Landslide EWSs typically use acoustic emissions, often in combination with other indicators such as the velocity of the landslide face, or rainfall intensity [*Pecoraro et al.*, 2019]. Operational Earthquake Early Warning (EEW) systems rely solely on the actual detection of earthquake events, and therefore only provide value where the epicentre is sufficiently far form population centres. While landslide EWSs are able to provide between a few seconds (when operating as an alarm system) to one day of warning (when forecasting), EEWs typically only achieve between a few seconds to tens of seconds. As a result of the small lead time, the complexity of the alert criterion is able to be kept relatively simple, consisting of thresholding set by empirical measurements. However, where the objective is to detect and issue automated precursory warnings to a hazardous event, whether that be in the region of a large fault zone, a landslide, or critical infrastructure, the complexity of the signatures and therefore alert criterion is increased.

In order to combine the increased sensitivity available through active source monitoring, with the increased complexity of alert criteria within an EWS, it is recommended that a Machine Learning (ML) approach is adopted. Specifically, Deep Neural Networks (DNNs) have the capability to generalise a large non-linear distribution of detection scenarios, and once trained the computational effort and time required in data processing is negligible. This makes a well trained DNN highly portable, and therefore capable of efficiently operating on a continuous stream of data, without the latency associated with transmitting large quantities of raw data to a processing centre. The successful implementation of supervised ML methods requires labelled training data, however, due to the very nature of geophysical problems, the true earth model (the labelled data) is almost never known. It is for this reason that the recent applications of DNNs in EEWs are trained on labelled catalogues of detected earthquakes [*Perol et al.*, 2018; *Wu et al.*, 2017, 2018; *Wiszniowski et al.*, 2014], and therefore provide no precursory predictive power.

In order to make the first steps towards addressing both the lack of precursory predictive power, and the lack of available training data, a workflow which incorporates numerical waveform propagation [*Afanasiev*, 2018] is suggested. Such an approach would enable the generation of a sufficiently large labelled training set, covering numerical simulations of a particular material perturbation. While this requires substantial computational resources, once trained such a network has the potential to be used in real-time prediction scenarios [*DeVries et al.*, 2017].

It is suggested that this approach is also able to simultaneously detect and locate a perturbation. A particular advantage of applying DDNs to solve what is effectively the CWD inverse problem, is that they have the potential to learn for the influence of complex boundary conditions and medium inhomogeneities, thereby circumventing the need to first numerically calculate suitable sensitivity kernels. Specifically, it is suggested that the type of DNN most suitable to both the detection and location problem are Recurrent Neural Networks (RNNs) which are commonly used in trigger

word detection [*Chen et al.*, 2015] and machine translation [*Cho et al.*, 2014], as they are able to encode the sequence of information. An example of a possible network structure to validate this for a 1D medium is given in appendix A.5.

In summary, the suggestion to train DNNs on synthetic data which sufficiently generalises the underlying physics, allows one to assess the feasibility of using active source coda-wave monitoring to provide truly precursory information within EWSs. Furthermore, the validation of this concept within synthetic models would provide considerable strength to the argument that active source monitoring systems are capable of delivering a step-change within EWSs. In other-words, while the majority of EWSs can be considered as reactive to changes which are observable at the boundaries of a region of interest, active source monitoring systems can be considered as proactive, in their investigation.

A

Chapter appendices

A.1 Yield-point identification

The yield point of a stress(σ)-strain(ϵ) curve is determined by a search for the end of the linear region between the minimum and maximum σ. This is achieved by fitting q lines of length m to the trend as described by,

$$\sigma_i^{fit} = \beta_0 + \beta_1 \epsilon_i, \tag{A.1.1}$$

$$\sigma_i^{fit}(\epsilon) = \begin{cases} \sigma_1^{fit}(\epsilon) & \epsilon_1 \leq \epsilon \leq \epsilon_{1+m} \\ \sigma_2^{fit}(\epsilon) & \epsilon_2 \leq \epsilon \leq \epsilon_{2+m} \\ & \vdots \\ \sigma_q^{fit}(\epsilon) & \epsilon_q \leq \epsilon \leq \epsilon_{q+m} \end{cases}.$$

The end of the linear region ($q + m = yield$) is selected at the end of the line $\sigma_q^{fit}(\epsilon_{yield})$, which meets the following criterion,

- The maximum slope β_1, where
- The fitting error at the end of the line $\Delta(\sigma_q^{fit}(\epsilon_{yield}), \sigma(\epsilon_{yield})) < 2\%$.

The length of m is selected to be approximately half the length of the linear elastic region in terms of sample points. The yield point is then defined at $(\sigma_{yield}^{fit}, \epsilon_{yield}^{fit})$.

A.2 Additional pore-pressure figures

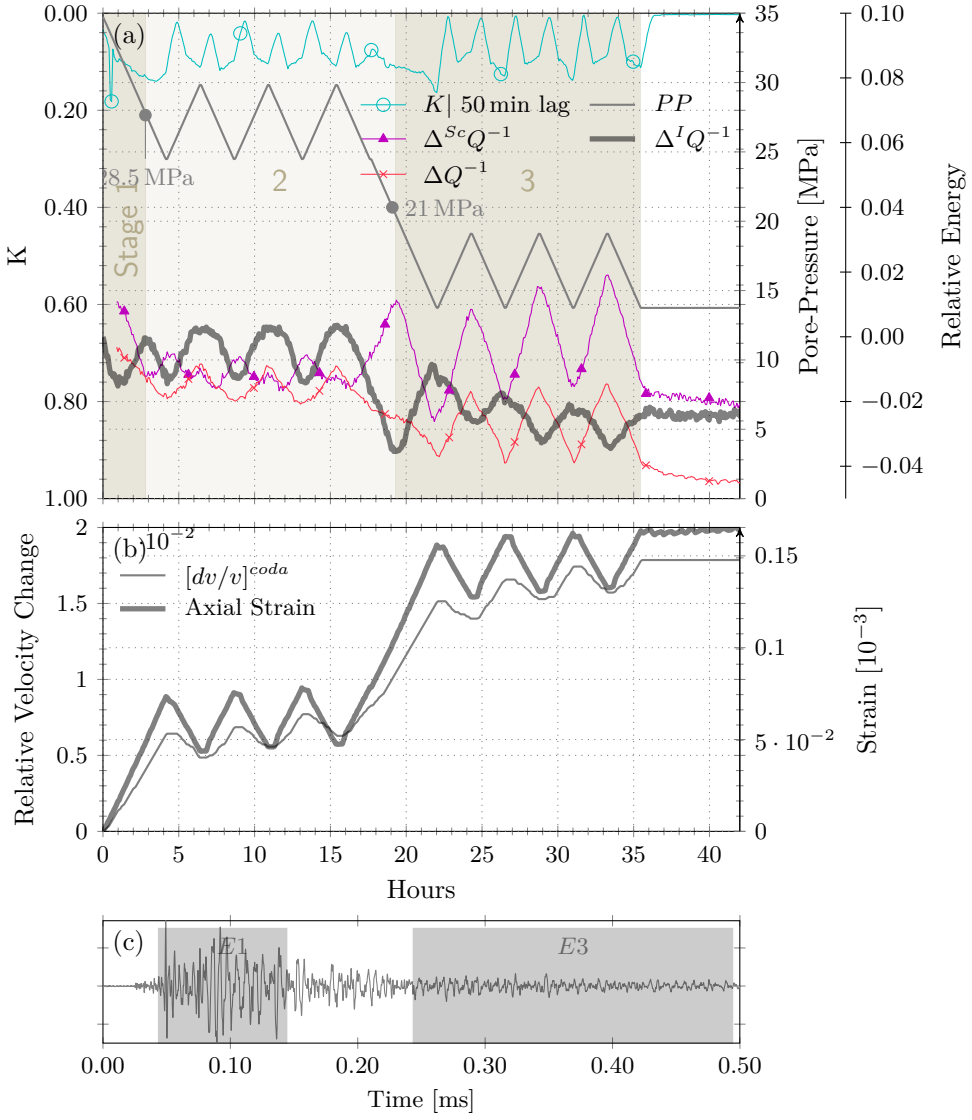

Figure A.1: *The 123BV* 24.68 % *porosity sample depleted at* 0.6 MPa h^{-1} *with the UPPD-MC protocol. a) Monitoring of the decorrelation coefficient* $K(|g_0|)$ *with a reference lag of* 50 min *and the relative changes in attenuative coefficients* ΔQ^{-1}, $\Delta^{Sc}Q^{-1}$, *and* $\Delta^{I}Q^{-1}$. *b) The CWI derived relative velocity change* dv/v^{coda} *are compared with the axial strain. c) Acquired waveform showing the* 0.1 ms E_1 *and* 0.25 ms E_3 *windows.*

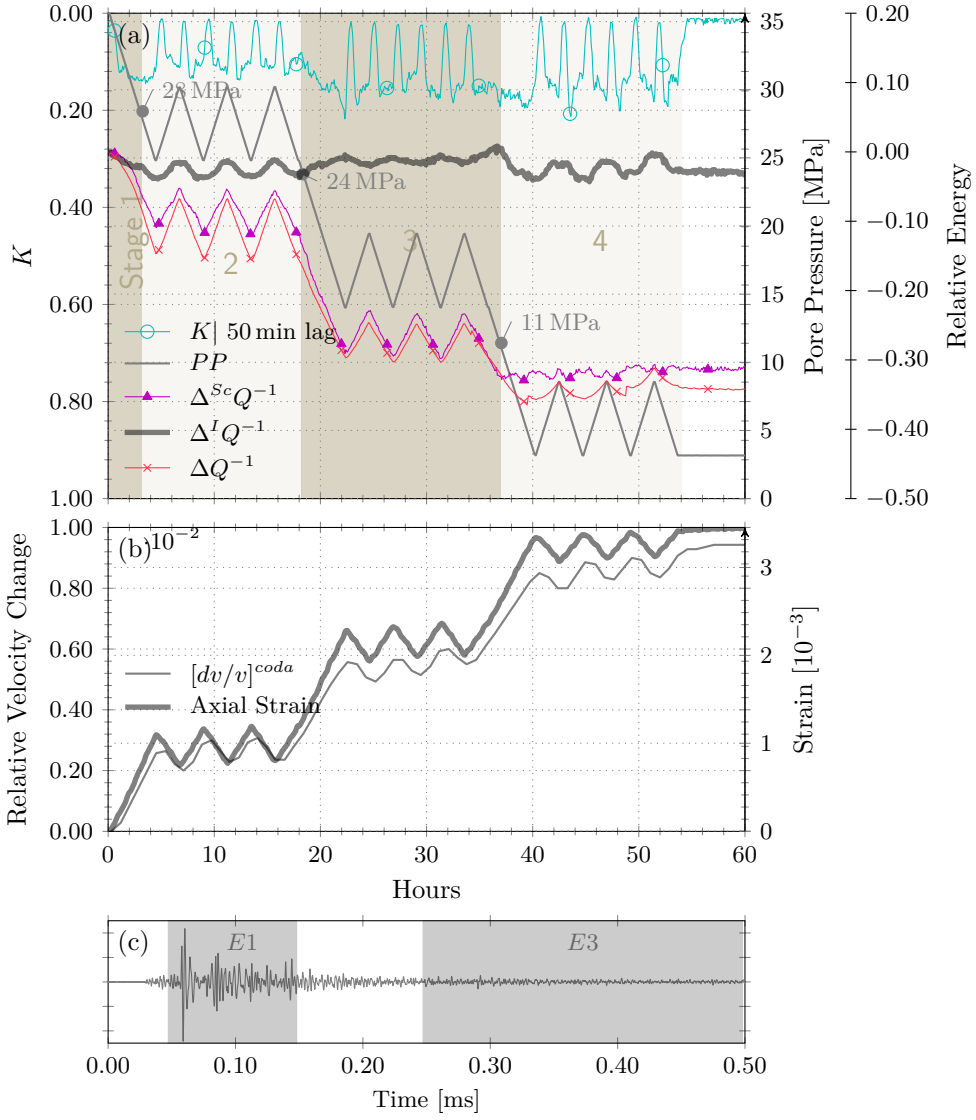

Figure A.2: *The 137AV* 19.2 % *porosity sample depleted at* 0.6 MPa h^{-1} *with the UPPD-MC protocol. a) Monitoring of the decorrelation coefficient* $K(|g_0|)$ *with a reference lag of* 50 min *and the relative changes in attenuative coefficients* ΔQ^{-1}, $\Delta^{Sc}Q^{-1}$, *and* $\Delta^{I}Q^{-1}$. *b) The CWI derived relative velocity change* dv/v^{coda} *are compared with the axial strain. c) Acquired waveform showing the* 0.1 ms E_1 *and* 0.25 ms E_3 *windows.*

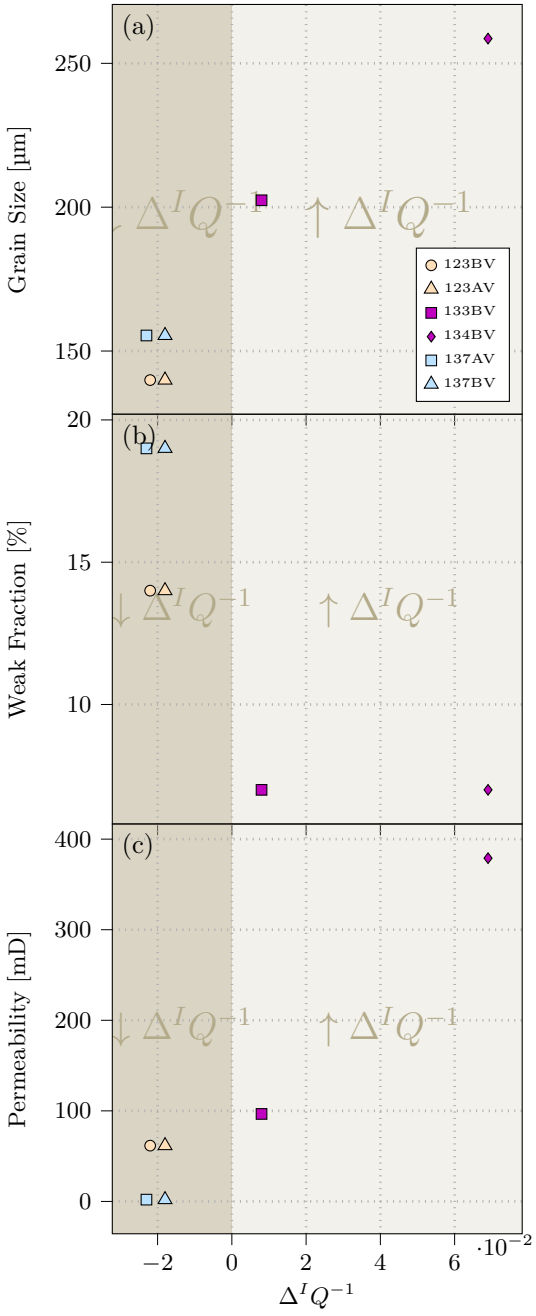

Figure A.3: *Comparison of the relative change in the intrinsic attenuation $\Delta^I Q^{-1}$ at maximum depletion vs a) average grain size, b) The fraction of weak minerals (Kfs(leached)+dol+kao+chl), and c) Initial Permeability.*

A.3 Supplementary information for chapter 3

■ Contents (Files uploaded separately)

[**1**] Backscattered electron (BSE) mosaics S1

[**2**] Acoustic, mechanical, and microstructure data S2

[**3**] Python based processing module pyCoda S3

■ Backscattered electron (BSE) mosaics S1.

Section-scale backscattered electron (BSE) mosaics were prepared using a FEI Helios Nanolab G3 scanning electron microscope, employing an acceleration voltage of 10 kV, beam current of 1.6 nA, and a working distance of 4 mm. See file *CrackMapping-123.pdf* available via
`https://doi.org/10.4121/uuid:45955068-7b0b-4b51-84f0-500a1c4cf63a`.

■ Acoustic, mechanical, and microstructure data S2.

Raw and processed data for all UPPD/UPPD-MC pore-pressure experiments as well as the corresponding Acoustic Emissions raw and processed data. All data is stored within Hierarchical Data Format (HDF5) within file *data.zip*, and is freely available via
`https://doi.org/10.4121/uuid:45955068-7b0b-4b51-84f0-500a1c4cf63a`.

■ Python based processing module pyCoda S3.

Processing code developed for the analysis of the raw data is available via DOI 10.5281/zenodo.3255940 or the github repository https://github.com/rdzotz/Coda-Analysis.

A.4 Supplementary information for chapter 4

A collection of movies supporting chapter 4 are available via http://doi.org/10.4121/uuid:dc3627dd-8434-4fa3-a4f0-b886c31c1ce2. In order to interact with the material please download and open with an Adobe Acrobat reader.

Contents (Files uploaded separately)

[**1**] Isometric rotation of the post-deformation fracture networks S1

[**2**] Time-Lapse movie of the Coda-Wave Decorrelation inversion results for sample 70 % S_w - S2

[**3**] Time-Lapse movie of the Coda-Wave Decorrelation inversion results for sample 58 % S_w - S3

[**4**] Time-Lapse movie of the Coda-Wave Decorrelation inversion results for sample 28 % S_w - S4

A.5 One dimensional validation of RNN performance in diffusive imaging

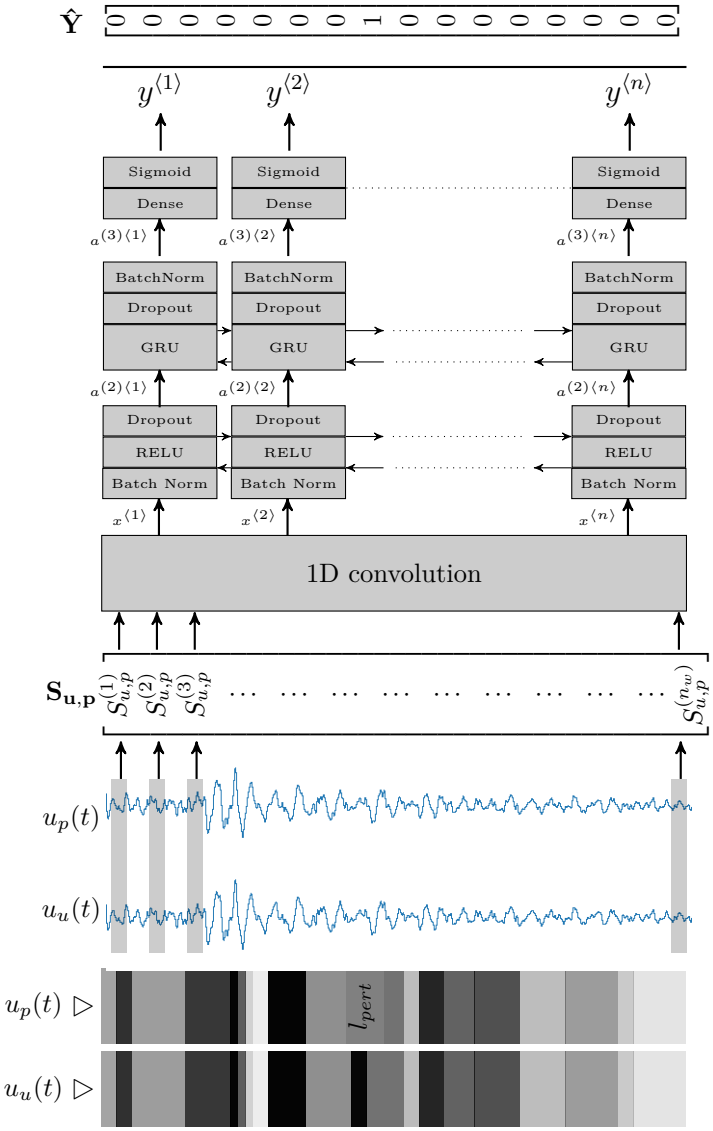

Figure A.4: *1D description of a possible RNN training structure for the detection of a local perturbation l_{pert}, between an unperturbed $u_u(t)$ and perturbed $u_p(t)$ waveform. The $\mathbf{S}_{u,p}$ represents the windowed spectrogram of the cross-correlation between $u_u(t)$ and $u_p(t)$, which is then pre-processed through a 1D convolution. This network consists of a RELU, GRU and Sigmoid output layer predicting for each grid cell the presence of a perturbation. The labelled training data $\hat{\mathbf{Y}}$ corresponds to the grid cells position of l_{pert}.*

Acknowledgements

While it is often stated that the primary objective of a PhD candidate is to become an independent researcher, this goal cannot be reached without the support and guidance of others. In the following section, I aim to acknowledge those individuals who have been instrumental during my pursuit of this goal, and who have ultimately made the writing of this thesis possible. Firstly, to my supervisors Kees Wapenaar and Auke Barnhoorn, thank you for allowing me to begin on this journey, it has been a privilege to work within the geophysics research group at the TU Delft. Thank you Kees, for providing such an excellent work environment, for your insightful and methodical feedback on my research, and for guiding me towards the body of research which ultimately led to the final research chapter of this thesis. Thank you Auke for all the guidance, support and motivation you provided me with, and for always being receptive to my ideas and aspirations. I am truly grateful for all of the time you invested in establishing and fostering collaborations during my PhD, without which the final two research chapters of this thesis would not have materialised. I also found our weekly conversations at the beginning of my PhD particularly useful as they helped me better understand rock-physics through the lens of geophysical investigation.

Like most PhD candidates, the first few months of research are consumed by reading countless papers, while struggling to find a reference point from which to build one's research. I want to thank Deyan Draganov and Kees Weemstra for their guidance during this period, without which it would have undoubtedly taken me much longer to stand on my own two feet. The support of the laboratory staff within the TU Delft rock mechanics lab and in particular Karel Heller for all his efforts in instrumentation enabled my first experimental study.

In my second year, it was thanks to the determination, optimism and energy of Nikoletta Filippidou that I was able to establish a collaboration with Shell Global Solutions International and Nederlandse Aardolie Maatschappij. Throughout this project the efforts of Arjan Van Der Linder, Sander Hol, Fons Marcelis and Ab

Coorn from Shell and Jan van Elk and Dirk Doornhof from NAM were invaluable. In particular, I want to thank my coauthor Bart Verberne for his guidance during this project, and his support during the ongoing peer-review process. The combined efforts of those mentioned enabled the writing of the second research chapter of this thesis.

I want to thank Lisanne Douma from the TU Delft and Jeremie Dautiat, Joel Sarout, and David Dewhurst from CSIRO Australia for their efforts during our collaboration. I understand it was no small feat to deal with the acquisition and data management requirements of the project without any guarantee that the method I was advocating would prove useful within an experimental rock mechanics context. Ultimately contributions of all parties involved allowed me to realise one of the main goals of my research, namely to combine the sensitivity of Coda-Wave interferometry with the ability to image change within a medium.

A special thank you goes to Christian Reinicke for allowing me to pollute his analytical world, through numerous discussions on often very empirical subjects, for sanity checking some of my more convoluted reasoning and most importantly, accompanying me on countless bike rides along the Vliet, through rain, hail, or shine to and from campus. Further, I want to thank all of my colleagues at the TU Delft, for the humorous, engaging and often left-of-field conversations held over lunch or during a coffee break. It has been these daily interactions with my colleagues which have made my PhD a truly enjoyable experience.

Katja, without your understanding and support I would never have had the courage to undertake a PhD in the first place, you truly give me wings. I appreciate the sacrifices you have made during the past four years, and I am sorry for all the evenings I spent working, for all the conversation you endured about my research, and for not always being fully present when you need me. Anfim and Miron, thank you for (almost) always greeting me at home with open arms and smiles on your faces. It has been my absolute pleasure to watch you both grow into the bright and cheerful boys you are today. To my mother, father and extended family, thank you for your collective nurture of nature. It goes without saying that your love, support, and culture of investigation through discussion has helped me greatly during the writing of this thesis, and now as a father myself, I can say thank you with full appreciation of the mammoth effort it takes to raise a child.

Reuben Zotz-Wilson,
Delft,
March 2020

Bibliography

Abdel-Fattah, A. K., M. Morsy, S. El-Hady, K. Y. Kim, and M. Sami (2008), Intrinsic and scattering attenuation in the crust of the Abu Dabbab area in the eastern desert of Egypt, *Phys. Earth Planet. Inter.*, *168*(1-2), 103–112, doi:10.1016/j.pepi.2008.05.005.

Aben, F. M., N. Brantut, T. M. Mitchell, and E. C. David (2019), Rupture Energetics in Crustal Rock From Laboratory-Scale Seismic Tomography, *Geophys. Res. Lett.*, doi:10.1029/2019GL083040.

Afanasiev, M. (2018), Salvus: A high-performance package for full waveform modelling and inversion from laboratory to global scales, in *Am. Geophys. Union, Fall Meet. 2016*.

Aikas, T., and R. Sundell (2014), ONKALO - From Concept to Reality, 1, pp. 1–9, WM2014 Conference, Phoenix,.

Aki, K. (1969), Analysis of the seismic coda of local earthquakes as scattered waves, *J. Geophys. Res.*, *74*(2), 615–631, doi:10.1029/JB074i002p00615.

Aki, K. (1980), Attenuation of shear-waves in the lithosphere for frequencies from 0.05 to 25 Hz, *Phys. Earth Planet. Inter.*, *21*(1), 50–60, doi:10.1016/0031-9201(80)90019-9.

Aki, K., and B. Chouet (1975), Origin of coda waves: Source, attenuation, and scattering effects, *J. Geophys. Res.*, *80*(23), 3322–3342, doi:10.1029/JB080i023p03322.

Akinci, A., and H. Eyidoan (2000), Scattering and anelastic attenuation of seismic energy in the vicinity of north anatolian fault zone, eastern Turkey, *Phys. Earth Planet. Inter.*, *122*(3-4), 229–239, doi:10.1016/S0031-9201(00)00196-5.

Akinci, A., E. Del Pezzo, and J. M. Ibáñez (1995), Separation of scattering and intrinsic attenuation in southern Spain and western Anatolia (Turkey), *Geophys. J. Int.*, *121*(2), 337–353, doi:10.1111/j.1365-246X.1995.tb05715.x.

Allen, R. M., and D. Melgar (2019), Earthquake Early Warning: Advances, Scientific Challenges, and Societal Needs, *Annu. Rev. Earth Planet. Sci.*, *47*(1), 361–388, doi:10.1146/annurev-earth-053018-060457.

Anugonda, P., J. S. Wiehn, and J. A. Turner (2001), Diffusion of ultrasound in concrete, *Ultrasonics*, *39*(6), 429–435, doi:10.1016/S0041-624X(01)00077-4.

Aplin, A. C., and J. H. Macquaker (2011), Mudstone diversity: Origin and implications for source, seal, and reservoir properties in petroleum systems, *Am. Assoc. Pet. Geol. Bull.*, doi:10.1306/03281110162.

Armitage, P. J., R. H. Worden, D. R. Faulkner, A. R. Butcher, and A. A. Espie (2016), Permeability of the Mercia Mudstone: suitability as caprock to carbon capture and storage sites, *Geofluids*, *16*(1), 26–42, doi:10.1111/gfl.12134.

Ayalew, L., and H. Yamagishi (2005), The application of GIS-based logistic regression for landslide susceptibility mapping in the Kakuda-Yahiko Mountains, Central Japan, *Geomorphology*, *65*(1-2), 15–31, doi:10.1016/j.geomorph.2004.06.010.

Barnhoorn, A., S. F. Cox, D. J. Robinson, and T. Senden (2010), Stress- and fluid-driven failure during fracture array growth: Implications for coupled deformation and fluid flow in the crust, *Geology*, *38*(9), 779–782, doi:10.1130/G31010.1.

Barnhoorn, A., J. Verheij, M. Frehner, A. Zhubayev, and M. Houben (2018), Experimental identification of the transition from elasticity to inelasticity from ultrasonic attenuation analyses, *GEOPHYSICS*, *83*(4), MR221–MR229, doi:10.1190/geo2017-0534.1.

Battaglia, J., J. P. Métaxian, and E. Garaebiti (2012), Earthquake-volcano interaction imaged by coda wave interferometry, *Geophys. Res. Lett.*, *39*(11), 4–7, doi:10.1029/2012GL052003.

Baud, P., E. Klein, and T. fong Wong (2004), Compaction localization in porous sandstones: Spatial evolution of damage and acoustic emission activity, *J. Struct. Geol.*, *26*(4), 603–624, doi:10.1016/j.jsg.2003.09.002.

Bernabé, Y., D. T. Fryer, and R. M. Shively (1994), Experimental Observations of the Elastic and Inelastic Behaviour of Porous Sandstones, *Geophys. J. Int.*, *117*(2), 403–418, doi:10.1111/j.1365-246X.1994.tb03940.x.

Bianco, F., E. Del Pezzo, M. Castellano, J. Ibanez, and F. Di Luccio (2002), Separation of intrinsic and scattering seismic attenuation in the Southern Apennine zone, Italy, *Geophys. J. Int.*, *150*(1), 10–22, doi:10.1046/j.1365-246X.2002.01696.x.

Bianco, F., E. Del Pezzo, L. Malagnini, F. Di Luccio, and A. Akinci (2005), Separation of depth-dependent intrinsic and scattering seismic attenuation in the northeastern sector of the Italian Peninsula, *Geophys. J. Int.*, *161*(1), 130–142, doi:10.1111/j.1365-246X.2005.02555.x.

Bieniawski, Z. T. (1967), Mechanism of brittle fracture of rock; Part I-theory of the fracture process, *Int. J. Rock Mech. Min. Sci.*, *4*, 395–406, doi:0148-9062(67)90030-7.

Biot, M. A. (1956), Theory of Propagation of Elastic Waves in a FluidSaturated Porous Solid. II. Higher Frequency Range, *J. Acoust. Soc. Am.*, *28*(2), 179–191, doi:10.1121/1.1908241.

Blanc, E. (2014), Time-domain numerical modeling of poroelastic waves : the Biot-JKD model with fractional derivatives To cite this version : HAL Id : tel-00954506 AIX-MARSEILLE UNIVERSITÉ Time-domain numerical modeling of poroelastic waves : the Biot-JKD model with fracti, Ph.D. thesis.

Blott, S. J., and K. Pye (2001), GRADISTAT: a grain size distribution and statistics package for the analysis of unconsolidated sediments, *Earth Surf. Process. Landforms*, *26*(11), 1237–1248, doi:10.1002/esp.261.

Borg, I., M. Friedman, J. Handin, and D. V. Higgs (1960), Chapter 6: Experimental Deformation of St. Peter Sand: A Study of Cataclastic Flow, in *Rock Deform. (A Symp.*, vol. 79, edited by D. Griggs and J. Handin, pp. 133—-192, Geological Society of America, doi:10.1130/MEM79-p133.

Bourne, S. J., S. J. Oates, J. van Elk, and D. Doornhof (2014), A seismological model for earthquakes induced by fluid extraction from a subsurface reservoir, *J. Geophys. Res. Solid Earth*, *119*(12), 8991–9015, doi:10.1002/2014JB011663.

Brantut, N. (2018), Time-resolved tomography using acoustic emissions in the laboratory, and application to sandstone compaction, *Geophys. J. Int.*, pp. 2177–2192, doi:10.1093/gji/ggy068.

Brantut, N., M. Heap, P. G. Meredith, and P. Baud (2013), Time-dependent cracking and brittle creep in crustal rocks: A review, *J. Struct. Geol.*, *52*(1), 17–43, doi:10.1016/j.jsg.2013.03.007.

Brookins, D. G. (1976), Shale as a repository for radioactive waste: The evidence from Oklo, *Environ. Geol.*, *1*(5), 255–259, doi:10.1007/BF02676715.

Brownjohn, J. M. W. (2007), Structural health monitoring of civil infrastructure, *Philos. Trans. R. Soc. A Math. Phys. Eng. Sci.*, *365*(1851), 589–622, doi:10.1098/rsta.2006.1925.

Brzesowsky, R. H., C. J. Spiers, C. J. Peach, and S. J. Hangx (2011), Failure behavior of single sand grains: Theory versus experiment, *J. Geophys. Res. Solid Earth*, *116*(6), 1–13, doi:10.1029/2010JB008120.

Brzesowsky, R. H., S. J. Hangx, N. Brantut, and C. J. Spiers (2014), Compaction creep of sands due to time-dependent grain failure: Effects of chemical environment, applied stress, and grain size, *J. Geophys. Res. Solid Earth*, *119*(10), 7521–7541, doi:10.1002/2014JB011277.

Busch, A., S. Alles, Y. Gensterblum, D. Prinz, D. Dewhurst, M. Raven, H. Stanjek, and B. Krooss (2008), Carbon dioxide storage potential of shales, *Int. J. Greenh. Gas Control*, *2*(3), 297–308, doi:10.1016/j.ijggc.2008.03.003.

Campillo, M. (2003), Long-Range Correlations in the Diffuse Seismic Coda, *Science (80-.).*, *299*(5606), 547–549, doi:10.1126/science.1078551.

Cannon, M., and P. Kole (2017), The First Year of Distributed Strain Sensing (DSS) Monitoring in the Groningen Gas Field, *Tech. Rep. November*, Nederlandse Aardolie Maatschappij.

Chandrasekhar, S. (1960), Radiative Transfer, in *Radiat. Transf.*, p. 393, Dover Publications, 1960.

Chen, G., C. Parada, and T. N. Sainath (2015), Query-by-example keyword spotting using long short-term memory networks, *ICASSP, IEEE Int. Conf. Acoust. Speech Signal Process. - Proc.*, *2015-Augus*, 5236–5240, doi:10.1109/ICASSP.2015.7178970.

Cho, K., B. van Merrienboer, D. Bahdanau, and Y. Bengio (2014), On the Properties of Neural Machine Translation: EncoderDecoder Approaches, in *Proc. SSST-8, Eighth Work. Syntax. Semant. Struct. Stat. Transl.*, pp. 103–111, Association for Computational Linguistics, Stroudsburg, PA, USA, doi:10.3115/v1/W14-4012.

Chuhan, F. A., A. Kjeldstad, K. Bjørlykke, and K. Høeg (2002), Porosity loss in sand by grain crushingexperimental evidence and relevance to reservoir quality, *Mar. Pet. Geol.*, *19*(1), 39–53, doi:10.1016/S0264-8172(01)00049-6.

Chung, T. W., M. Z. Iqbal, Y. Lee, K. Yoshimoto, and J. Jeong (2018), Depth-dependent seismicity and crustal heterogeneity in South Korea, *Tectonophysics*, *749*(April), 12–20, doi:10.1016/j.tecto.2018.10.020.

David, C., B. Menendez, W. Zhu, and T.-f. Wong (2001), Mechanical compaction, microstructures and permeability evolution in sandstones, *Phys. Chem. Earth, Part A Solid Earth Geod.*, *26*(1), 45–51, doi:https://doi.org/10.1016/S1464-1895(01)00021-7.

David, E. C., N. Brantut, A. Schubnel, and R. W. Zimmerman (2012), Sliding crack model for nonlinearity and hysteresis in the uniaxial stress-strain curve of rock, *Int. J. Rock Mech. Min. Sci.*, *52*, 9–17, doi:10.1016/j.ijrmms.2012.02.001.

De Waal, J. (1986), On the rate type compaction behaviour of sandstone reservoir rock, Ph.D. thesis, Delft University of Technology, doi:uuid:b805782b-2eb4-4f72-98f4-f727c4ea9df0.

Del Pezzo, E., F. Bianco, S. Marzorati, P. Augliera, E. D'Alema, and M. Massa (2011), Depth-dependent intrinsic and scattering seismic attenuation in north central Italy, *Geophys. J. Int.*, *186*(1), 373–381, doi:10.1111/j.1365-246X.2011.05053.x.

Dempsey, D., and J. Suckale (2017), Physics-based forecasting of induced seismicity at Groningen gas field, the Netherlands, *Geophys. Res. Lett.*, *44*(15), 7773–7782, doi:10.1002/2017GL073878.

Den Haan, E. (1994), Vertical compression of soils, Ph.D. thesis, TUDelft, doi:uuid:b8dc88e0-f400-4d86-9a2e-4e00b68d0472.

DeVries, P. M., T. B. Thompson, and B. J. Meade (2017), Enabling large-scale viscoelastic calculations via neural network acceleration, *Geophys. Res. Lett.*, *44*(6), 2662–2669, doi:10.1002/2017GL072716.

DiGiovanni, A. A., J. T. Fredrich, D. J. Holcomb, and W. A. Olsson (2007), Microscale damage evolution in compacting sandstone, *Geol. Soc. London, Spec. Publ.*, *289*(1), 89 LP – 103.

Doornhof, D., T. G. Kristiansen, N. B. Nogel, P. D. Pattillo, and C. Sayers (2006), Compaction and Subsidence, *Oilf. Rev.*, *Autumn*, 50–68.

Dost, B., E. Ruigrok, and J. Spetzler (2017), Development of seismicity and probabilistic hazard assessment for the Groningen gas field, *Geol. en Mijnbouw/Netherlands J. Geosci.*, *96*(5), s235–s245, doi:10.1017/njg.2017.20.

Douma, L. A. N. R., J. Dautriat, J. Sarout, D. N. Dewhurst, and A. Barnhoorn (2019), Impact of water saturation on the elastic anisotropy of the Whitby Mudstone, United Kingdom, *Submitt. to Geophys.*

Dudley, J. W., M. Brignoli, B. R. Crawford, R. T. Ewy, D. K. Love, J. D. McLennan, G. G. Ramos, J. L. Shafer, M. H. Sharf-Aldin, E. Siebrits, J. Boyer, and M. A. Chertov (2016), ISRM Suggested Method for Uniaxial-Strain Compressibility Testing for Reservoir Geomechanics, *Rock Mech. Rock Eng.*, *49*(10), 4153–4178, doi:10.1007/s00603-016-1055-4.

Ebisuzaki, W. (1997), A method to estimate the statistical significance of a correlation when the data are serially correlated, *J. Clim.*, *10*(9), 2147–2153, doi:10.1175/1520-0442(1997)010<2147:AMTETS>2.0.CO;2.

Elliott, G. M., and E. T. Brown (1986), Further development of a plasticity approach to yield in porous rock, *Int. J. Rock Mech. Min. Sci.*, *23*(2), 151–156, doi:10.1016/0148-9062(86)90341-4.

Erling, F., R. Holt, A. M. Raaen, R. Risnes, and P. Horsrud (2008), *Petroleum related rock mechanics*, 2nd ed., 251 – 287 pp., Elsevier Sience.

Ewy, R. T. (2014), Shale swelling/shrinkage and water content change due to imposed suction and due to direct brine contact, *Acta Geotech.*, *9*(5), 869–886, doi:10.1007/s11440-013-0297-5.

Fatt, I., and D. Davis (1952), Reduction in Permeability With Overburden Pressure, *J. Pet. Technol.*, *4*(12), 16–16, doi:10.2118/952329-G.

Fehler, M., M. Hoshiba, H. Sato, and K. Obara (1992), Separation of scattering and intrinsic attenuation for the Kanto-Tokai region, Japan, using measurementsof S-wave energy versus hypocentral distance, *Geophys. J. Int.*, *108*(3), 787–800, doi:10.1111/j.1365-246X.1992.tb03470.x.

Fialko, Y., and M. Simons (2000), Deformation and seismicity in the Coso geothermal area, Inyo County, California: Observations and modeling using satellite radar interferometry, *J. Geophys. Res. Solid Earth*, *105*(B9), 21,781–21,793, doi:10.1029/2000JB900169.

Forsans, T. M., and L. Schmitt (1994), Capillary forces: The neglected factor in shale instability studies?, *Soc. Pet. Eng. - Rock Mech. Pet. Eng. 1994*, pp. 71–84.

Frangos, W. (1967), The effect of continuing pressure on the permeability of westerly granite: B.S. thesis M.I.T.

Frankel, A., and L. Wennerberg (1987), Energy-flux model of seismic coda: Separation of scattering and intrinsic attenuation, *Bull. Seismol. Soc. Am.*, *77*(4), 1223–1251.

Gao, F., D. Stead, and D. Elmo (2016), Numerical simulation of microstructure of brittle rock using a grain-breakable distinct element grain-based model, *Comput. Geotech.*, *78*, 203–217, doi:10.1016/j.compgeo.2016.05.019.

Garrels, R. M., and F. T. Mackenzie (1969), Sedimentary Rock Types: Relative Proportions as a Function of Geological Time, *Science (80-.).*, *163*(3867), 570–571, doi:10.1126/science.163.3867.570.

Geuzaine, C., and J.-F. Remacle (2017), A three-dimensional finite element mesh generator with built-in pre- and post-processing facilities, *Int. J. Numer. Meth. Engng.*

Ghorbani, A., M. Zamora, and P. Cosenza (2009), Effects of desiccation on the elastic wave velocities of clay-rocks, *Int. J. Rock Mech. Min. Sci.*, *46*(8), 1267–1272, doi:10.1016/j.ijrmms.2009.01.009.

Grasso, J. R. (1992), Mechanics of seismic instabilities induced by the recovery of hydrocarbons, *Pure Appl. Geophys. PAGEOPH*, *139*(3-4), 507–534, doi:10.1007/BF00879949.

Grêt, A. (2005), Monitoring rapid temporal change in a volcano with coda wave interferometry, *Geophys. Res. Lett.*, *32*(6), L06,304, doi:10.1029/2004GL021143.

Grêt, A., R. Snieder, and U. Özbay (2006a), Monitoring in situ stress changes in a mining environment with coda wave interferometry, *Geophys. J. Int.*, *167*(2), 504–508, doi:10.1111/j.1365-246X.2006.03097.x.

Grêt, A., R. Snieder, and J. Scales (2006b), Time-lapse monitoring of rock properties with coda wave interferometry, *J. Geophys. Res. Solid Earth*, *111*(3), 1–11, doi:10.1029/2004JB003354.

Griffiths, L., O. Lengliné, M. J. Heap, P. Baud, and J. Schmittbuhl (2018), Thermal Cracking in Westerly Granite Monitored Using Direct Wave Velocity, Coda Wave Interferometry, and Acoustic Emissions, *J. Geophys. Res. Solid Earth*, *123*(3), 2246–2261, doi:10.1002/2017JB015191.

Grinfeld, M. A., and A. N. Norris (1996), Acoustoelasticity theory and applications for fluidsaturated porous media, *J. Acoust. Soc. Am.*, *100*(3), 1368–1374, doi:10.1121/1.415983.

Gusev, A., and V. K. Lemzikov (1985), Properties of scattered elastic waves in the lithosphere of kamchatka: Parameters and temporal variations, *Tectonophysics*, *112*(1-4), 137–153, doi:10.1016/0040-1951(85)90177-5.

Hadziioannou, C., E. Larose, O. Coutant, P. Roux, and M. Campillo (2009), Stability of monitoring weak changes in multiply scattering media with ambient noise correlation: Laboratory experiments, *J. Acoust. Soc. Am.*, *125*(6), 3688–3695, doi:10.1121/1.3125345.

Hadziioannou, C., J. Salvermoser, R. Steinmann, L. Marten, and E. Niederleithinger (2019), Structural Health Monitoring Meets Ambient Noise Seismology, EAGE, doi:10.3997/2214-4609.201902553.

Hangx, S. J., C. J. Spiers, and C. J. Peach (2010), Creep of simulated reservoir sands and coupled chemical-mechanical effects of CO 2 injection, *J. Geophys. Res.*, *115*(B9), B09,205, doi:10.1029/2009JB006939.

Hanson, J. a., and H. Yang (2009), A general statistical test for correlations, *J. Chem. Phys.*, *112*(44), 13,962–13,970, doi:10.1021/jp804440y.Quantitative.

Heap, M., and D. Faulkner (2008), Quantifying the evolution of static elastic properties as crystalline rock approaches failure, *Int. J. Rock Mech. Min. Sci.*, *45*(4), 564–573, doi:10.1016/j.ijrmms.2007.07.018.

Heap, M. J., P. Baud, P. G. Meredith, A. F. Bell, and I. G. Main (2009), Time-dependent brittle creep in darley dale sandstone, *J. Geophys. Res. Solid Earth*, *114*(7), 1–22, doi:10.1029/2008JB006212.

Heap, M. J., N. Brantut, P. Baud, and P. G. Meredith (2015), Time-dependent compaction band formation in sandstone, *J. Geophys. Res. Solid Earth*, *120*(7), 4808–4830, doi:10.1002/2015JB012022.

Herrmann, R. B. (1975), The use of duration as a measure of seismic moment and magnitude, *Bull. Seismol. Soc. Am.*

Hol, S., A. Mossop, A. van der Linden, P. Zuiderwijk, and A. Makurat (2015), Long-term compaction behavior of Permian sandstones - An investigation into the mechanisms of subsidence in the Dutch Wadden Sea, *Arma*, *15-618*.

Hol, S., A. Van Der Linden, S. Bierman, F. Marcelis, and A. Makurat (2018a), Rock Physical Controls on Production-induced Compaction in the Groningen Field, *Sci. Rep.*, *8*(1), 1–13, doi:10.1038/s41598-018-25455-z.

Hol, S., A. Van Der Linden, S. Bierman, F. Marcelis, and A. Makurat (2018b), Proxies for quantifying depletion-induced reservoir compaction in the Groningen Field, in *ARMA18 - 52nd US Rock Mech. / Geomech. Symp.*

Hoshiba, M. (1991), Simulation of multiple-scattered coda wave excitation based on the energy conservation law, *Phys. Earth Planet. Inter.*, *67*(1-2), 123–136, doi:10.1016/0031-9201(91)90066-Q.

Hoshiba, M. (1993), Separation of scattering attenuation and intrinsic absorption in Japan using the multiple lapse time window analysis of full seismogram envelope, *J. Geophys. Res.*, *98*(B9), 15,809, doi:10.1029/93JB00347.

Hoshiba, M. (1994), Simulation of coda wave envelope in depth dependent scattering and absorption structure, *Geophys. Res. Lett.*, *21*(25), 2853–2856, doi:10.1029/94GL02718.

Hoshiba, M. (1995), Estimation of nonisotropic scattering in western Japan using coda wave envelopes: Application of a multiple nonisotropic scattering model, *J. Geophys. Res. Solid Earth*, *100*(B1), 645–657, doi:10.1029/94JB02064.

Hoshiba, M. (1997), Seismic coda wave envelope in depth-dependent S wave velocity structure, *Phys. Earth Planet. Inter.*, *104*(1-3), 15–22, doi:10.1016/S0031-9201(97)00055-1.

Hoshiba, M., A. Rietbrock, F. Scherbaum, H. Nakahara, and C. Haberland (2001), Scattering attenuation and intrinsic absorption using uniform and depth dependent model-application to full seismogram envelope recorded in Northern Chile, *J. Seismol.*, *5*(2), 157–179, doi:10.1023/A:1011478202750.

Houben, M., A. Barnhoorn, L. Wasch, J. Trabucho-Alexandre, C. Peach, and M. Drury (2016a), Microstructures of Early Jurassic (Toarcian) shales of Northern Europe, *Int. J. Coal Geol.*, *165*, 76–89, doi:10.1016/j.coal.2016.08.003.

Houben, M. E., A. Barnhoorn, J. Lie-A-Fat, T. Ravestein, C. J. Peach, and M. R. Drury (2016b), Microstructural characteristics of the Whitby Mudstone Formation (UK), *Mar. Pet. Geol.*, *70*, 185–200, doi:10.1016/j.marpetgeo.2015.11.011.

Izumi, K., M. Ogihara, and H. Kameyaf (1998), *Displacements of bridge foundations on sedimentary soft rock: A case study on small-strain stiffness*, pp. 233–246, doi:10.1680/pdbog.26421.0016.

Jacobson, R. S. (1987), An investigation into the fundamental relationships between attenuation, phase dispersion, and frequency using seismic refraction profiles over sedimentary structures, *GEOPHYSICS*, *52*(1), 72–87, doi:10.1190/1.1442242.

Jansen, D. P., S. R. Carlson, R. P. Young, and D. A. Hutchins (1993), Ultrasonic imaging and acoustic emission monitoring of thermally induced microcracks in Lac du Bonnet granite, *J. Geophys. Res.*, *98*(B12).

Jianghui, M., Z. Min, Z. Hongjing, L. Luofu, W. Zhiyong, Z. Jieli, and W. Ying (2012), Geochemical Evidence for Coal and Carbonaceous Mudstone as the Possible Major Oil Source Rock in the Jurassic Turpan Basin, Northwest China, *Acta Geol. Sin. - English Ed.*, *86*(5), 1171–1181, doi:10.1111/j.1755-6724.2012.00739.x.

Jin, A., and K. Aki (1986), Temporal Change in Coda Q Before the Tangshan Earthquake of 1976 and the Haicheng Earthquake of 1975, *J. Geophys. Res.*, *91*(B1), 665–673, doi:10.1029/JB091iB01p00665.

Jin, A., and K. Aki (1989), Spatial and Temporal Correlation Between Coda and Seismicity and Its Physical Mechanism, *J. Geophys. Res.*, *94*, 14,041–14.

Johnston, D. H., M. N. Toksöz, and A. Timur (1979), Attenuation of seismic waves in dry and saturated rocks: II. Mechanisms, *GEOPHYSICS*, *44*(4), 691–711, doi:10.1190/1.1440970.

Kandula, N., B. Cordonnier, D. K. Dysthe, J. R. Sanchez, X. Zheng, F. Renard, W. Zhu, M. Kobchenko, J. McBeck, P. Meakin, C. Noiriel, and F. Fusseis (2018), Dynamic In Situ Three-Dimensional Imaging and Digital Volume Correlation Analysis to Quantify Strain Localization and Fracture Coalescence in Sandstone, *Pure Appl. Geophys.*, *C*, doi:10.1007/s00024-018-2003-x.

Kanu, C., and R. Snieder (2015), Numerical computation of the sensitivity kernel for monitoring weak changes with multiply scattered acoustic waves, *Geophys. J. Int.*, *203*(3), 1923–1936, doi:10.1093/gji/ggv391.

Kawahara, J., T. Ohno, and K. Yomogida (2009), Attenuation and dispersion of antiplane shear waves due to scattering by many two-dimensional cavities, *J. Acoust. Soc. Am.*, *125*(6), 3589–3596, doi:10.1121/1.3124779.

Kopnichev, Y. (1975), A model of generation of the tail of the seismogram, *Dok Akad Nauk. USSR*, (222), 333–335.

Kopnichev, Y. (1977a), Models for the Formation of the Coda of the Longitudinal Wave, *Dok Akad Nauk. USSR*, (234), 560–563.

Kopnichev, Y. (1977b), The Role of Multiple Scattering in the Formation of a Seismogram's Tail, *Izv. Acad. Sci. USSR, Phys. Solid Earth*, (13), 394–398.

Laloui, L., S. Salager, and M. Rizzi (2013), Retention behaviour of natural clayey materials at different temperatures, *Acta Geotech.*, *8*(5), 537–546, doi:10.1007/s11440-013-0255-2.

Larose, E., and S. Hall (2009), Monitoring stress related velocity variation in concrete with a 2E10-5 relative resolution using diffuse ultrasound, *J. Acoust. Soc. Am.*, *125*(4), 1853–1856, doi:10.1121/1.3079771.

Larose, E., J. De Rosny, L. Margerin, D. Anache, P. Gouedard, M. Campillo, and B. Van Tiggelen (2006), Observation of multiple scattering of kHz vibrations in a concrete structure and application to monitoring weak changes, *Phys. Rev. E - Stat. Nonlinear, Soft Matter Phys.*, doi:10.1103/PhysRevE.73.016609.

Larose, E., T. Planes, V. Rossetto, and L. Margerin (2010), Locating a small change in a multiple scattering environment, *Appl. Phys. Lett.*, *96*(20), doi:10.1063/1.3431269.

Larose, E., A. Obermann, A. Digulescu, T. Planès, J.-F. Chaix, F. Mazerolle, and G. Moreau (2015), Locating and characterizing a crack in concrete with diffuse ultrasound: A four-point bending test, *J. Acoust. Soc. Am.*, *138*(1), 232–241, doi:10.1121/1.4922330.

Lei, X., K. Masuda, O. Nishizawa, L. Jouniaux, L. Liu, W. Ma, T. Satoh, and K. Kusunose (2004), Detailed analysis of acoustic emission activity during catastrophic fracture of faults in rock, *J. Struct. Geol.*, *26*(2), 247–258, doi:10.1016/S0191-8141(03)00095-6.

Lele, S. P., S.-Y. Hsu, J. L. Garzon, N. DeDontney, K. H. Searles, G. A. Gist, P. F. Sanz, E. A. O. Biediger, and B. A. Dale (2016), Geomechanical Modeling to Evaluate Production-Induced Seismicity at Groningen Field, in *Abu Dhabi Int. Pet. Exhib. Conf.*, Society of Petroleum Engineers, doi:10.2118/183554-MS.

Li, C., R. Prikryl, and E. Nordlund (1998), The stress-strain behaviour of rock material related to fracture under compression, *Eng. Geol.*, *49*(3-4), 293–302, doi:10.1016/S0013-7952(97)00061-6.

Linnaeus, C. (1771), Mantissa Plantarum, *Mantissa Plant.*

Lockner, D. (1993), The role of acoustic emission in the study of rock fracture, *Int. J. Rock Mech. Min. Sci. Geomech. Abstr.*, *30*(7), 883–899, doi:10.1016/0148-9062(93)90041-B.

Lockner, D. A., J. B. Walsh, and J. D. Byerlee (1977), Changes in seismic velocity and attenuation during deformation of granite, *J. Geophys. Res.*, *82*(33), 5374–5378, doi:10.1029/JB082i033p05374.

Main, I. G. (1990), Quasi-static modelling of stress histories during the earthquake cycle: precursory seismic and aseismic stress release, *Geophys. J. Int.*, *102*(1), 195–203, doi:10.1111/j.1365-246X.1990.tb00541.x.

Mainsant, G., E. Larose, C. Brönnimann, D. Jongmans, C. Michoud, and M. Jaboyedoff (2012), Ambient seismic noise monitoring of a clay landslide: Toward failure prediction, *J. Geophys. Res. Earth Surf.*, *117*(F1), n/a–n/a, doi:10.1029/2011JF002159.

Mao, L., and F.-p. Chiang (2016), 3D strain mapping in rocks using digital volumetric speckle photography technique, *Acta Mech.*, *227*(11), 3069–3085, doi:10.1007/s00707-015-1531-z.

Mao, L., H. Liu, Y. Zhu, Z. Zhu, R. Guo, and F.-p. Chiang (2019), 3D Strain Mapping of Opaque Materials Using an Improved Digital Volumetric Speckle Photography Technique with X-Ray Microtomography, *Appl. Sci.*, *9*(7), 1418, doi:10.3390/app9071418.

Margerin, L., T. Planès, J. Mayor, and M. Calvet (2016), Sensitivity kernels for coda-wave interferometry and scattering tomography: Theory and numerical evaluation in two-dimensional anisotropically scattering media, *Geophys. J. Int.*, *204*(1), 650–666, doi:10.1093/gji/ggv470.

Martini, F., C. J. Bean, G. Saccorotti, F. Viveiros, and N. Wallenstein (2009), Seasonal cycles of seismic velocity variations detected using coda wave interferometry at Fogo volcano, São Miguel, Azores, during 2003-2004, *J. Volcanol. Geotherm. Res.*, *181*(3-4), 231–246, doi:10.1016/j.jvolgeores.2009.01.015.

Masera, D., P. Bocca, and A. Grazzini (2011), Coda Wave Interferometry Method Applied in Structural Monitoring to Assess Damage Evolution in Masonry and Concrete Structures, *J. Phys. Conf. Ser.*, *305*, 012,108, doi:10.1088/1742-6596/305/1/012108.

Matsumoto, S., K. Obara, K. Yoshimoto, T. Saito, A. Ito, and A. Hasegawa (2001), Temporal change in P -wave scatterer distribution associated with the M 6.1 earthquake near Iwate volcano, northeastern Japan, *Geophys. J. Int.*, *145*(1), 48–58, doi:10.1111/j.1365-246X.2001.00339.x.

Mavko, G., E. Kjartansson, K. Winkler, and M. Park (1979), Seismic wave attenuation in rocks, *Rev. Geophys. Sp. Physics, Am. Geophys. Union*, *17*(6), 1155–1164.

Mayeda, K., S. Koyanagi, M. Hoshiba, K. Aki, and Y. Zeng (1992), A comparative study of scattering, intrinsic, and coda Q-1for Hawaii, Long Valley, and central California between 1.5 and 15.0 hz, *J. Geophys. Res.*, *97*(B5), 6643–6659, doi:10.1029/91JB03094.

McBeck, J., M. Kobchenko, S. A. Hall, E. Tudisco, B. Cordonnier, P. Meakin, and F. Renard (2018), Investigating the Onset of Strain Localization Within Anisotropic Shale Using Digital Volume Correlation of Time-Resolved X-Ray Microtomography Images, *J. Geophys. Res. Solid Earth*, *123*(9), 7509–7528, doi:10.1029/2018JB015676.

Menéndez, B., W. Zhu, and T.-F. Wong (1996), Micromechanics of brittle faulting and cataclastic flow in Berea sandstone, *J. Struct. Geol.*, *18*(1), 1–16, doi:https://doi.org/10.1016/0191-8141(95)00076-P.

Michaels, J. E., and T. E. Michaels (2005), Detection of structural damage from the local temporal coherence of diffuse ultrasonic signals, *IEEE Trans. Ultrason. Ferroelectr. Freq. Control*, doi:10.1109/TUFFC.2005.1561631.

Michoud, C., S. Bazin, L. H. Blikra, M. H. Derron, and M. Jaboyedoff (2013), Experiences from site-specific landslide early warning systems, *Nat. Hazards Earth Syst. Sci.*, *13*(10), 2659–2673, doi:10.5194/nhess-13-2659-2013.

Mobach, E., and H. Gussinklo (1994), In-situ reservoir compaction monitoring in the Groningen field, *Rock Mech. Pet. Eng.*, doi:10.2118/28094-MS.

Mogi, K. (2007), *Experimental rock mechanics*, 361 pp., CRC Press, doi:10.1016/j.ijrmms.2007.08.006.

Morton, R. A., J. C. Bernier, and J. A. Barras (2006), Evidence of regional subsidence and associated interior wetland loss induced by hydrocarbon production, Gulf Coast region, USA, *Environ. Geol.*, *50*(2), 261–274, doi:10.1007/s00254-006-0207-3.

Mossop, A. (2012), An explanation for anomalous time dependent subsidence, in *46th US Rock Mech. / Geomech. Symp. 2012*.

Mulders, F. (2003), Modelling of stress development and fault slip in and around a producing gas reservoir, Ph.D. thesis, Delft University of Technology.

Nakahara, H., and K. Emoto (2017), Deriving Sensitivity Kernels of Coda-Wave Travel Times to Velocity Changes Based on the Three-Dimensional Single Isotropic Scattering Model, *Pure Appl. Geophys.*, *174*(1), 327–337, doi:10.1007/s00024-016-1358-0.

NAM (2013), Technical Addendum to the Winningsplan Groningen 2013 Subsidence, Induced Earthquakes and Seismic Hazard Analysis in the Groningen Field, *Tech. Rep. November*, Nederlandse Aardolie Maatschappij.

NAM (2016a), Supplement to the Technical Addendum for Winningsplan Groningen 2016, *Tech. rep.*, Nederlandse Aardolie Maatschappij.

NAM (2016b), Technical Addendum to the Winningsplan Groningen 2016 Production, Subsidence, Induced Earthquakes and Seismic Hazard and Risk Assessment in the Groningen Field - Part V Damage and Appendices, *Tech. Rep. April*, Nederlandse Aardolie Maatschappij.

Niu, F., P. G. Silver, T. M. Daley, X. Cheng, and E. L. Majer (2008), Preseismic velocity changes observed from active source monitoring at the Parkfield SAFOD drill site, *Nature*, *454*(7201), 204–208, doi:10.1038/nature07111.

Obermann, A., T. Planès, E. Larose, and M. Campillo (2013a), Imaging preeruptive and coeruptive structural and mechanical changes of a volcano with ambient seismic noise, *J. Geophys. Res. Solid Earth*, *118*(12), 6285–6294, doi:10.1002/2013JB010399.

Obermann, A., T. Planès, E. Larose, C. Sens-Schönfelder, and M. Campillo (2013b), Depth sensitivity of seismic coda waves to velocity perturbations in an elastic heterogeneous medium, *Geophys. J. Int.*, *194*, 372–382, doi:10.1093/gji/ggt043.

Obermann, A., B. Froment, M. Campillo, E. Larose, T. Planès, B. Valette, J. H. Chen, and Q. Y. Liu (2014), Seismic noise correlations to image structural and mechanical changes associated with the Mw 7 . 9 2008 Wenchuan earthquake, *J. Geophys. Res. Solid Earth*, *119*(4), 3155–3168, doi:10.1002/2013JB010932.Received.

Obermann, A., T. Planès, E. Larose, and M. Campillo (2019), 4-D Imaging of Subsurface Changes with Coda Waves: Numerical Studies of 3-D Combined Sensitivity Kernels and Applications to the M_{w} 7.9, 2008 Wenchuan Earthquake, *Pure Appl. Geophys.*, *176*(3), 1243–1254, doi:10.1007/s00024-018-2014-7.

Obregon, A., A. Gutierrez, A. Kavvada, C. Larlee, D. Cripe, G. Camara, I. Jarvis, J. Norris, J. Nelson, P. D. Salvo, S. Volz, S. Ramage, W. Chu, and Y. Gevorgyan (2018), Geo highlights 2017-2018, *Tech. rep.*

Onaisi, A., C. Durand, and A. Audibert (1994), Role of hydration state of shales in borehole stability studies, *Soc. Pet. Eng. - Rock Mech. Pet. Eng. 1994*, pp. 275–285.

Ord, A., I. Vardoulakis, and R. Kajewski (1991), Shear band formation in Gosford Sandstone, *Int. J. Rock Mech. Min. Sci. Geomech. Abstr.*, *28*(5), 397–409, doi:https://doi.org/10.1016/0148-9062(91)90078-Z.

Otsu, N. (1979), A Threshold Selection Method from Gray-Level Histograms, *IEEE Trans. Syst. Man. Cybern.*, *9*(1), 62–66, doi:10.1109/TSMC.1979.4310076.

Paasschens, J. (1997), Solution of the time-dependent Boltzmann equation, *Phys. Rev. E*, *56*(1), 1135–1141, doi:10.1103/PhysRevE.56.1135.

Pacheco, C., and R. Snieder (2005), Time-lapse travel time change of multiply scattered acoustic waves, *J. Acoust. Soc. Am.*, *118*(3), 1300, doi:10.1121/1.2000827.

Page, J. H., M. L. Cowan, and D. Weitz (2000), Diffusing acoustic wave spectroscopy of fluidized suspensions, *Phys. B Condens. Matter*, *279*(1-3), 130–133, doi:10.1016/S0921-4526(99)00698-5.

Pandolfi, D., C. J. Bean, and G. Saccorotti (2006), Coda wave interferometric detection of seismic velocity changes associated with the 1999 M = 3.6 event at Mt. Vesuvius, *Geophys. Res. Lett.*, *33*(6), 4–7, doi:10.1029/2005GL025355.

Paterson, M. S., and T. F. Wong (2005), Experimental Rock Deformation The Brittle Field, in *Exp. Rock Deform. - Brittle F.*, p. 32, Springer-Verlag, Berlin/Heidelberg, doi:10.1007/b137431.

Payan, C., V. Garnier, J. Moysan, and P. A. Johnson (2009), Determination of third order elastic constants in a complex solid applying coda wave interferometry, *Appl. Phys. Lett.*, doi:10.1063/1.3064129.

Pecoraro, G., M. Calvello, and L. Piciullo (2019), Monitoring strategies for local landslide early warning systems, *Landslides*, *16*(2), 213–231, doi:10.1007/s10346-018-1068-z.

Peksa, A. E., K. H. A. Wolf, and P. L. Zitha (2015), Bentheimer sandstone revisited for experimental purposes, *Mar. Pet. Geol.*, *67*, 701–719, doi:10.1016/j.marpetgeo.2015.06.001.

Peng, J., and S. Q. Yang (2018), Comparison of mechanical behavior and acoustic emission characteristics of three thermally-damaged rocks, *Energies*, *11*(9), doi:10.3390/en11092350.

Perol, T., M. Gharbi, and M. Denolle (2018), Convolutional neural network for earthquake detection and location, *Sci. Adv.*, *4*(2), e1700,578, doi:10.1126/sciadv.1700578.

Pijnenburg, R. P. J., B. A. Verberne, S. J. Hangx, and C. J. Spiers (2018), Deformation Behavior of Sandstones From the Seismogenic Groningen Gas Field: Role of Inelastic Versus Elastic Mechanisms, *J. Geophys. Res. Solid Earth*, *123*(7), 5532–5558, doi:10.1029/2018JB015673.

Pijnenburg, R. P. J., B. A. Verberne, S. J. T. Hangx, and C. J. Spiers (2019), Inelastic Deformation of the Slochteren Sandstone: StressStrain Relations and Implications for Induced Seismicity in the Groningen Gas Field, *J. Geophys. Res. Solid Earth*, p. 2019JB017366, doi:10.1029/2019JB017366.

Pijpers, F., and D. J. Van der Laan (2016), Trend changes in ground subsidence in Groningen, (May).

Pine, D., D. Weitz, J. Zhu, and E. Herbolzheimer (1990), Diffusing-wave spectroscopy: dynamic light scattering in the multiple scattering limit, *J. Phys.*, *51*(18), 2101–2127, doi:10.1051/jphys:019900510180210100.

Planès, T. (2013), Imagerie de chargements locaux en regime de diffusion multiple, Ph.D. thesis, Université de Grenoble.

Planès, T., and E. Larose (2013), A review of ultrasonic Coda Wave Interferometry in concrete, *Cem. Concr. Res.*, *53*, 248–255, doi:10.1016/j.cemconres.2013.07.009.

Planès, T., E. Larose, V. Rossetto, and L. Margerin (2013), LOCADIFF: Locating a weak change with diffuse ultrasound, *405*(2013), 405–411, doi:10.1063/1.4789076.

Planès, T., E. Larose, L. Margerin, V. Rossetto, and C. Sens-Schönfelder (2014), Decorrelation and phase-shift of coda waves induced by local changes: multiple scattering approach and numerical validation, *Waves in Random and Complex Media*, *24*(2), 99–125, doi:10.1080/17455030.2014.880821.

Planès, T., E. Larose, V. Rossetto, and L. Margerin (2015), Imaging multiple local changes in heterogeneous media with diffuse waves, *J. Acoust. Soc. Am.*, *137*(2), 660–667, doi:10.1121/1.4906824.

Poupinet, G., F. Glangeaud, and P. Côte (1982), P-Time delay measurement of a doublet of microearthquakes, *ICASSP, IEEE Int. Conf. Acoust. Speech Signal Process. - Proc.*, *1982-May*(June), 1516–1519, doi:10.1109/ICASSP.1982.1171796.

Poupinet, G., W. L. Ellsworth, and J. Frechet (1984), Monitoring velocity variations in the crust using earthquake doublets: An application to the Calaveras Fault, California, *J. Geophys. Res.*, *89*(B7), 5719–5731, doi:10.1029/JB089iB07p05719.

Poupinet, G., J. L. Got, and F. Brenguier (2008), Monitoring Temporal Variations of Physical Properties in the Crust by CrossCorrelating the Waveforms of Seismic Doublets, in *Eff. Seism. Waves, Adv. Geophys.*, chap. 14, pp. 374–399, Advanc, New York.

Powell, J. H. (2010), Jurassic sedimentation in the Cleveland Basin: a review, *Proc. Yorksh. Geol. Soc.*, *58*(1), 21–72, doi:10.1144/pygs.58.1.278.

Pratt, W. E., and D. W. Johnson (1926), Local Subsidence of the Goose Creek Oil Field, *J. Geol.*, doi:10.1086/521238.

Preibisch, S., S. Saalfeld, and P. Tomancak (2009), Globally optimal stitching of tiled 3D microscopic image acquisitions, *Bioinformatics*, *25*(11), 1463–1465, doi:10.1093/bioinformatics/btp184.

Pruiksma, J. P., J. N. Breunese, K. Van Thienen-Visser, and J. A. de Waal (2015), Isotach formulation of the rate type compaction model for sandstone, *Int. J. Rock Mech. Min. Sci.*, *78*, 127–132, doi:10.1016/j.ijrmms.2015.06.002.

Pujades, L. G., A. Ugalde, J. A. Canas, M. Navarro, F. J. Badal, and V. Corchete (1997), Intrinsic and scattering attenuation from observed seismic codas in the Almeria Basin (southeastern Iberian Peninsula), *Geophys. J. Int.*, *129*(2), 281–291, doi:10.1111/j.1365-246X.1997.tb01581.x.

Pye, K. (1985), Electron microscope analysis of zoned dolomite rhombs in the Jet Rock Formation (Lower Toarcian) of the Whitby area, U.K., *Geol. Mag.*, *122*(3), 279–286, doi:10.1017/S0016756800031496.

Rachman, A. N., T. W. Chung, K. Yoshimoto, and B. Son (2015), Separation of Intrinsic and Scattering Attenuation Using Single Event Source in South Korea, *Bull. Seismol. Soc. Am.*, *105*(2A), 858–872.

Rachman, A. N., T. W. Chung, and K.-H. Chung (2017), Multiple lapse time window analysis using solely single events in South Korea, *Explor. Geophys.*, *48*(4), 504–511, doi:10.1071/EG16098.

RAJI, W. O., and A. Rietbrock (2012), The use of seismic attenuation for monitoring saturation in hydrocarbon reservoirs, in *SEG Tech. Progr. Expand. Abstr. 2012*, pp. 1–6, Society of Exploration Geophysicists, doi:10.1190/segam2012-0309.1.

Ramos da Silva, M., C. Schroeder, and J. C. Verbrugge (2008), Unsaturated rock mechanics applied to a low-porosity shale, *Eng. Geol.*, *97*(1-2), 42–52, doi:10.1016/j.enggeo.2007.12.003.

Ratdomopurbo, A., and G. Poupinet (1995), Monitoring a temporal change of seismic velocity in a volcano: Application to the 1992 eruption of Mt. Merapi (Indonesia), *Geophys. Res. Lett.*, *22*(7), 775–788, doi:10.1029/95GL00302.

Rautian, T., and V. Khalturin (1978), The use of the coda for determination of the earthquake source spectrum, *Bull. Seismol. Soc. Am.*

Renard, F., B. Cordonnier, M. Kobchenko, N. Kandula, J. Weiss, and W. Zhu (2017), Microscale characterization of rupture nucleation unravels precursors to faulting in rocks, *Earth Planet. Sci. Lett.*, *476*, 69–78, doi:10.1016/j.epsl.2017.08.002.

Renard, F., J. Weiss, J. Mathiesen, Y. Ben-Zion, N. Kandula, and B. Cordonnier (2018), Critical Evolution of Damage Toward System-Size Failure in Crystalline Rock, *J. Geophys. Res. Solid Earth*, *123*(2), 1969–1986, doi:10.1002/2017JB014964.

Roecker, S. W., B. Tucker, J. King, and D. Hatzfeld (1982), Estimates of Q in central Asia as a function of frequency and depth using the coda of locally recorded earthquakes, *Bull. Seismol. Soc. Am.*, *72*, 129–149.

Rossetto, V., L. Margerin, T. Planès, and E. Larose (2011), Locating a weak change using diffuse waves: Theoretical approach and inversion procedure, *J. Appl. Phys.*, *109*(3), 034,903, doi:10.1063/1.3544503.

Sarout, J., C. Delle Piane, D. Nadri, L. Esteban, and D. N. Dewhurst (2015), A robust experimental determination of Thomsen's δ parameter, *GEOPHYSICS*, *80*(1), A19–A24, doi:10.1190/geo2014-0391.1.

Sarout, J., Y. Le Gonidec, A. Ougier-Simonin, A. Schubnel, Y. Gu??guen, and D. N. Dewhurst (2017), Laboratory micro-seismic signature of shear faulting and fault slip in shale, *Phys. Earth Planet. Inter.*, *264*, 47–62, doi:10.1016/j.pepi.2016.11.005.

Sato, H. (1977a), Energy Propagation Including Scattering Effects, Single Isotropic Scattering Approximation, *J. Phys. Earth*, *25*, 27–41.

Sato, H. (1977b), Single isotropic scattering model including wave conversions simple theoretical model of the short period body wave propagation., *J. Phys. Earth*, *25*(2), 163–176, doi:10.4294/jpe1952.25.163.

Sato, H. (1978), Mean free path of S-waves under the Kanto district of Japan, *J. Phys. Earth*, *26*, 185–198, doi:10.4294/jpe1952.26.185.

Sato, H. (1994), Multiple isotropic scattering model including, *0*, 487–494.

Sato, H., M. C. Fehler, and T. Maeda (2012), *Seismic Wave Propagation and Scattering in the Heterogeneous Earth : Second Edition*, vol. 9783642230, 1–494 pp., Springer Berlin Heidelberg, Berlin, Heidelberg, doi:10.1007/978-3-642-23029-5.

Schindelin, J., I. Arganda-Carreras, E. Frise, V. Kaynig, M. Longair, T. Pietzsch, S. Preibisch, C. Rueden, S. Saalfeld, B. Schmid, J.-Y. Tinevez, D. J. White, V. Hartenstein, K. Eliceiri, P. Tomancak, and A. Cardona (2012), Fiji: an open-source platform for biological-image analysis., *Nat. Methods*, *9*(7), 676–682, doi:10.1038/nmeth.2019.

Schurr, D. P., J. Y. Kim, K. G. Sabra, and L. J. Jacobs (2011), Damage detection in concrete using coda wave interferometry, *NDT E Int.*, *44*(8), 728–735, doi:10.1016/j.ndteint.2011.07.009.

Segall, P., and S. D. Fitzgerald (1998), A note on induced stress changes in hydrocarbon and geothermal reservoirs, *Tectonophysics*, *289*(1-3), 117–128, doi:10.1016/S0040-1951(97)00311-9.

Selleck, S. F., E. N. Landis, M. L. Peterson, S. P. Shah, and J. D. Achenbach (1998), Ultrasonic investigation of concrete with distributed damage, *ACI Mater. J.*, *95*(1), 27–36, doi:10.14359/349.

Sens-Schönfelder, C., and E. Larose (2008), Temporal changes in the lunar soil from correlation of diffuse vibrations, *Phys. Rev. E - Stat. Nonlinear, Soft Matter Phys.*, *78*(4), 1–4, doi:10.1103/PhysRevE.78.045601.

Sens-Schönfelder, C., and U. Wegler (2006), Passive image interferometry and seasonal variations of seismic velocities at Merapi Volcano, Indonesia, *Geophys. Res. Lett.*, *33*(21), L21,302, doi:10.1029/2006GL027797.

Sens-Schönfelder, C., L. Margerin, and M. Campillo (2009), Laterally heterogeneous scattering explains Lg blockage in the Pyrenees, *J. Geophys. Res. Solid Earth*, *114*(7), 1–19, doi:10.1029/2008JB006107.

Shabelansky, A. H., A. Malcolm, and M. Fehler (2015), Monitoring viscosity changes from time-lapse seismic attenuation: case study from a heavy oil reservoir, *Geophys. Prospect.*, *63*(5), 1070–1085, doi:10.1111/1365-2478.12229.

Shah, A. A., and S. Hirose (2010), Nonlinear Ultrasonic Investigation of Concrete Damaged under Uniaxial Compression Step Loading, *J. Mater. Civ. Eng.*, *22*(5), 476–484, doi:10.1061/(ASCE)MT.1943-5533.0000050.

Shalev, E., V. Lyakhovsky, A. Ougier-Simonin, Y. Hamiel, and W. Zhu (2014), Inelastic compaction, dilation and hysteresis of sandstones under hydrostatic conditions, *Geophys. J. Int.*, *197*(2), 920–925, doi:10.1093/gji/ggu052.

Shang, T., and L. S. Gao (1988), Transportation theory of multiple scattering and its application to seismic coda waves of impulse source, *Sci. Sin. (series B)*, *1*(12), 26, doi:10.1360/yb1988-31-12-1503.

Shapiro, N. M., M. Campillo, L. Stehly, and M. H. Ritzwoller (2005), High-resolution surface-wave tomography from ambient seismic noise, *Science (80-.).*, doi:10.1126/science.1108339.

Sharp, J. M., and D. W. Hill (1995), Land subsidence along the northeastern Texas Gulf coast: Effects of deep hydrocarbon production, *Environ. Geol.*, *25*(3), 181–191, doi:10.1007/BF00768547.

Shokouhi, P., A. Zoëga, and H. Wiggenhauser (2010), Nondestructive investigation of stress-induced damage in concrete, *Adv. Civ. Eng.*, *2010*, doi:10.1155/2010/740189.

Snieder, R. (2002a), Coda Wave Interferometry for Estimating Nonlinear Behavior in Seismic Velocity, *Science (80-.).*, *295*(5563), 2253–2255, doi:10.1126/science.1070015.

Snieder, R. (2002b), Coda wave interferometry and the equilibration of energy in elastic media, *Phys. Rev. E - Stat. Nonlinear, Soft Matter Phys.*, *66*(4), 1–8, doi:10.1103/PhysRevE.66.046615.

Snieder, R., and M. Hagerty (2004), Monitoring change in volcanic interiors using coda wave interferometry: Application to Arenal Volcano, Costa Rica, *Geophys. Res. Lett.*, *31*(9), doi:10.1029/2004GL019670.

Snieder, R., and M. Vrijlandt (2005), Constraining the source separation with coda wave interferometry: Theory and application to earthquake doublets in the Hayward fault, California, *J. Geophys. Res. Solid Earth*, *110*(4), 1–15, doi:10.1029/2004JB003317.

Snieder, R., H. Douma, and J. Scales (2002), Coda Wave Interferometry for Estimating Nonlinear Behavior in Seismic Velocity, *Science (80-.).*, *295*(March), 2253–2255, doi:10.1126/science.1070015.

Spetzler, J., and B. Dost (2017), Hypocentre estimation of induced earthquakes in Groningen, *Geophys. J. Int.*, *209*(1), 453–465, doi:10.1093/gji/ggx020.

Spiers, C. J., S. J. Hangx, and A. R. Niemeijer (2017), New approaches in experimental research on rock and fault behaviour in the Groningen gas field, *Geol. en Mijnbouw/Netherlands J. Geosci.*, *96*(5), s55–s69, doi:10.1017/njg.2017.32.

Stähler, S. C., C. Sens-Schönfelder, and E. Niederleithinger (2011), Monitoring stress changes in a concrete bridge with coda wave interferometry., *J. Acoust. Soc. Am.*, *129*(4), 1945–1952, doi:10.1121/1.3553226.

Stähli, M., M. Sättele, C. Huggel, B. W. McArdell, P. Lehmann, A. Van Herwijnen, A. Berne, M. Schleiss, A. Ferrari, A. Kos, D. Or, and S. M. Springman (2015), Monitoring and prediction in early warning systems for rapid mass movements, *Tech. Rep. 4*, doi:10.5194/nhess-15-905-2015.

Stoll, R. D., and G. M. Bryan (1970), Wave Attenuation in Saturated Sediments, *J. Acoust. Soc. Am.*, *47*(5B), 1440–1447, doi:10.1121/1.1912054.

Suckale, J. (2009), Induced Seismicity in Hydrocarbon Fields, *Adv. Geophys.*, *51*(C), 55–106, doi:10.1016/S0065-2687(09)05107-3.

Sullivan, C., and A. Kaszynski (2019), PyVista: 3D plotting and mesh analysis through a streamlined interface for the Visualization Toolkit (VTK), *J. Open Source Softw.*, *4*(37), 1450, doi:10.21105/joss.01450.

Tarantola, A. (2005), *Inverse Problem Theory and Methods for Model Parameter Estimation*, vol. 120, 1816–24 pp., Society for Industrial and Applied Mathematics, doi:10.1137/1.9780898717921.

Toksoz, M. N., and D. H. Johnston (1981), *Seismic Wave Attenuation*, geophysics ed., Soc of Exploration Geophysicists.

Toupin, R. A., and B. Bernstein (1961), Sound Waves in Deformed Perfectly Elastic Materials. Acoustoelastic Effect, *J. Acoust. Soc. Am.*, *33*(2), 216–225, doi:10.1121/1.1908623.

UN/ISDR: Global (2006), Global Survey of Early Warning Systems, *Tech. rep.*, United Nations.

Vales, F., D. Nguyen Minh, H. Gharbi, and A. Rejeb (2004), Experimental study of the influence of the degree of saturation on physical and mechanical properties in Tournemire shale (France), *Appl. Clay Sci.*, *26*(1-4 SPEC. ISS.), 197–207, doi:10.1016/j.clay.2003.12.032.

van Eijs, R. (2015), Neotectonic Stresses in the Permian Slochteren Formation of the Groningen Field, *Tech. Rep. November*, NAM.

Van Eijs, R. M., F. M. Mulders, M. Nepveu, C. J. Kenter, and B. C. Scheffers (2006), Correlation between hydrocarbon reservoir properties and induced seismicity in the Netherlands, *Eng. Geol.*, *84*(3-4), 99–111, doi:10.1016/j.enggeo.2006.01.002.

Van Thienen-Visser, K., and J. N. Breunese (2015), Induced seismicity of the Groningen gas field: History and recent developments, *Lead. Edge*, *34*(6), 664–671, doi:10.1190/tle34060664.1.

Van Thienen-Visser, K., and P. A. Fokker (2017), The future of subsidence modelling: Compaction and subsidence due to gas depletion of the Groningen gas field in the Netherlands, *Geol. en Mijnbouw/Netherlands J. Geosci.*, *96*(5), s105–s116, doi:10.1017/njg.2017.10.

Van Wees, J. D., L. Buijze, K. Van Thienen-Visser, M. Nepveu, B. B. Wassing, B. Orlic, and P. A. Fokker (2014), Geomechanics response and induced seismicity during gas field depletion in the Netherlands, *Geothermics*, *52*, 206–219, doi:10.1016/j.geothermics.2014.05.004.

Verberne, B., and C. J. Spiers (2017), A quantitative microstructural investigation of depleted and undepleted reservoir sandstones, *51st US Rock Mech. / Geomech. Symp. held San Fr. California, USA, 25-28 June 2017*.

Vomvoris, S., A. Claudel, I. Blechschmidt, and H. Muller (2013), The Swiss Radioactive Waste Management Program - Brief History, Status, and Outlook, *J. Nucl. Fuel Cycle Waste Technol.*, *1*(1), 9–27, doi:10.7733/jnfcwt.2013.1.1.9.

Walsh, J. B. (1965), The effect of cracks on the compressibility of rock, *J. Geophys. Res.*, *70*(2), 381–389, doi:10.1029/JZ070i002p00381.

Walsh, J. B. (1966), Seismic Wave Attenuation in Rock Due to Frcition, *J. Geophys. Res.*, *71*(10), 2591–2599.

Walsh, J. B. (1969), New analysis of attenuation in partially melted rock, *J. Geophys. Res.*, *74*(17), 4333–4337, doi:10.1029/JB074i017p04333.

Wang, B., P. Zhu, Y. Chen, F. Niu, and B. Wang (2008), Continuous subsurface velocity measurement with coda wave interferometry, *J. Geophys. Res. Solid Earth*, *113*(12), 1–12, doi:10.1029/2007JB005023.

Wang, T., H. Wu, Y. Li, H. Gui, Y. Zhou, M. Chen, X. Xiao, W. Zhou, and X. Zhao (2013), Stability analysis of the slope around flood discharge tunnel under inner water exosmosis at Yangqu hydropower station, *Comput. Geotech.*, *51*, 1–11, doi:https://doi.org/10.1016/j.compgeo.2013.01.006.

Wapenaar, K. (2004), Retrieving the Elastodynamic Green's Function of an Arbitrary Inhomogeneous Medium by Cross Correlation, *Phys. Rev. Lett.*, *93*(25), 254,301, doi:10.1103/PhysRevLett.93.254301.

Wassing, B. (2015), Modeling of Fault Reactivation and Fault Slip in Producing Gas Fields, in *Second EAGE Work. Geomech. Energy*, October 2015, doi:10.3997/2214-4609.201414288.

Weaver, R. L., and O. I. Lobkis (2000), Temperature dependence of diffuse field phase, *Ultrasonics*, doi:10.1016/S0041-624X(99)00047-5.

Wegler, U., and C. Sens-Schönfelder (2007), Fault zone monitoring with passive image interferometry, *Geophys. J. Int.*, *168*(3), 1029–1033, doi:10.1111/j.1365-246X.2006.03284.x.

Wesley, J. P. (1965), Diffusion of Seismic Energy in the Near Range, *J. Geophys. Res.*, *70*(9).

Widess, M. B. (1973), HOW THIN IS A THIN BED?, *GEOPHYSICS*, *38*(6), 1176–1180, doi:10.1190/1.1440403.

Wiszniowski, J., B. M. Plesiewicz, and J. Trojanowski (2014), Application of real time recurrent neural network for detection of small natural earthquakes in Poland, *Acta Geophys.*, *62*(3), 469–485, doi:10.2478/s11600-013-0140-2.

Wu, R.-S. (1982), Mean Field Attenuation and Amplitude Attenuation Due to Wave Scattering, *Wave Motion*, *4*, 305–316, doi:10.1016/0165-2125(82)90026-9.

Wu, R.-S. (1985), Multiple scattering and energy transfer of seismic waves – separation of scattering effect from intrinsic attenuation – I. Theoretical modelling, *Geophys. J. Int.*, *82*(1), 57–80, doi:10.1111/j.1365-246X.1985.tb05128.x.

Wu, R.-S., and K. Aki (1988), Multiple scattering and energy transfer of seismic waves - separation of scattering effect from intrinsic attentuation II. Application of the theory to Hindu Kush region, *Pure appl. Geophys.*, *128*, 49–80.

Wu, Y., Y. Lin, Z. Zhou, D. C. Bolton, J. Liu, and P. Johnson (2017), Cascaded Region-based Densely Connected Network for Event Detection: A Seismic Application, pp. 1–14.

Wu, Y., Y. Lin, Z. Zhou, and A. Delorey (2018), Seismic-Net: A Deep Densely Connected Neural Network to Detect Seismic Events, *i*(April), 1–8.

Wunderlich, C., and E. Niederleithinger (2012), Evaluation of temperature influence on ultrasound velocity in concrete by coda wave interferometry, *RILEM Bookseries*, doi:10.1007/978-94-007-0723-8_33.

Xue, Q., E. Larose, and L. Moreau (2019), Locating structural changes in a multiple scattering domain with an irregular shape, *J. Acoust. Soc. Am.*, *146*(1), 595–602, doi:10.1121/1.5118246.

Yamamoto, M., and H. Sato (2010), Multiple scattering and mode conversion revealed by an active seismic experiment at Asama volcano, Japan, *J. Geophys. Res. Solid Earth*, *115*(7), 1–14, doi:10.1029/2009JB007109.

Yoshida, N., M. Nishi, M. Kitamura, and T. Adachi (1997), Analysis of mudstone deterioration and its effect on tunnel performance, *Int. J. Rock Mech. Min. Sci.*, *34*(3-4), 353.e1–353.e19, doi:10.1016/S1365-1609(97)00289-X.

Yoshimoto, K. (2000), Monte Carlo simulation of seismogram envelopes in scattering media, *J. Geophys. Res. Solid Earth*, *105*(B3), 6153–6161, doi:10.1029/1999JB900437.

Yoshimoto, K., H. Sato, and M. Ohtake (1993), Frequency-Dependent Attenuation of P and S Waves In the Kanto Area, Japan, Based On the Coda-Normalization Method, *Geophys. J. Int.*, *114*(1), 165–174, doi:10.1111/j.1365-246X.1993.tb01476.x.

Yoshimoto, K., H. Sato, Y. Iio, H. Ito, T. Ohminato, and M. Ohtake (1998), Frequency-dependent attenuation of high-frequency P and S waves in the Upper Crust in Western Nagano, Japan, *Pure Appl. Geophys.*, doi:10.1007/s000240050205.

Yuehua Zeng (1991), Compact solutions for multiple scattered wave energy in time domain, *Bull. - Seismol. Soc. Am.*, *81*(3), 1022–1029.

Zbinden, D., A. P. Rinaldi, L. Urpi, and S. Wiemer (2017), On the physics-based processes behind production-induced seismicity in natural gas fields, *J. Geophys. Res. Solid Earth*, *122*(5), 3792–3812, doi:10.1002/2017JB014003.

Zeng, Y., Feng Su, and K. Aki (1991), Scattering wave energy propagation in a random isotropic scattering medium: 1. Theory, *J. Geophys. Res.*, *96*(B1), 607–619, doi:10.1029/90jb02012.

Zhang, F., C. Juhlin, C. Cosma, A. Tryggvason, and R. G. Pratt (2012a), Cross-well seismic waveform tomography for monitoring CO2 injection: a case study from the Ketzin Site, Germany, *Geophys. J. Int.*, *189*(1), 629–646, doi:10.1111/j.1365-246X.2012.05375.x.

Zhang, Y., O. Abraham, E. Larose, T. Planes, A. Le Duff, B. Lascoup, V. Tournat, R. El Guerjouma, L. M. Cottineau, and O. Durand (2011), Following stress level modification of real size concrete structures with CODA wave interferometry (CWI), *AIP Conf. Proc.*, *1335*(June 2011), 1291–1298, doi:10.1063/1.3592082.

Zhang, Y., O. Abraham, F. Grondin, A. Loukili, V. Tournat, A. L. Duff, B. Lascoup, and O. Durand (2012b), Study of stress-induced velocity variation in concrete under direct tensile force and monitoring of the damage level by using thermally-compensated Coda Wave Interferometry, *Ultrasonics*, *52*(8), 1038–1045, doi:10.1016/j.ultras.2012.08.011.

Zhang, Y., T. Planès, E. Larose, A. Obermann, C. Rospars, and G. Moreau (2016), Diffuse ultrasound monitoring of stress and damage development on a 15-ton concrete beam, *J. Acoust. Soc. Am.*, *139*(4), 1691–1701, doi:10.1121/1.4945097.

Zhang, Y., E. Larose, L. Moreau, and G. D'Ozouville (2018), Three-dimensional in-situ imaging of cracks in concrete using diffuse ultrasound, *Struct. Heal. Monit.*, *17*(2), doi:10.1177/1475921717690938.

Zhao, H. (2019), Monitoring our changing planet, *ITU News Mag.*, (1), 62.

Zijp, M., J. Ten Veen, R. Verreussel, J. T. Heege, D. Ventra, and J. Martin (2015), Shale gas formation research: From well logs to outcrop - And back again, *First Break*, *33(2)*(2), 99–106.

Zoback, M., S. Hickman, and W. Ellsworth (2011), Scientific Drilling Into the San Andreas Fault Zone -An Overview of SAFOD's First Five Years, *Sci. Drill.*, *11*(March 2011), 14–28, doi:10.2204/iodp.sd.11.02.2011.

Zoback, M. D. (2007), Effects of reservoir depletion, in *Reserv. Geomech.*, edited by M. D. Zoback, pp. 378–422, Cambridge University Press, Cambridge, doi:DOI:10.1017/CBO9780511586477.013.

Zotz-Wilson, R. (2019a), Acoustic, mechanical, and microstructure data used in: Coda-Wave Based Monitoring of Pore-Pressure Depletion-driven Compaction of Slochteren Sandstone Samples from the Groningen Gas Field, doi:https://doi.org/10.4121/uuid:45955068-7b0b-4b51-84f0-500a1c4cf63a.

Zotz-Wilson, R. (2019b), Coda-Analysis: First release of Coda-Analysis, doi:10.5281/zenodo.3255940.

Zotz-Wilson, R., T. Boerrigter, and A. Barnhoorn (2019), Coda-wave monitoring of continuously evolving material properties and the precursory detection of yielding, *J. Acoust. Soc. Am.*, *145*(2), 1060–1068, doi:10.1121/1.5091012.

Zwiers, F. (1990), The effect of serial correlation on statistical inferences made with resampling procedures, *J. Clim.*, *3*, 1452–1461, doi:10.1175/1520-0442(1990)003<1452:TEOSCO>2.0.CO;2.

List of symbols and abbreviations

Symbols

The principal symbols used are alphabetically listed. Symbols formed by adding overbars, primes or indices are not listed separately. Boldface type indicates vector quantities.

Symbol	Description	Units
ϕ_0	Initial porosity	%
Q^{-1}	Total attenuation	-
${}^{Sc}Q^{-1}$	Scattering attenuation	-
${}^{I}Q^{-1}$	Intrinsic attenuation	-
$\mathcal{D}$	Diffusivity	$\mathrm{m^2\,s^{-1}}$
a_1	Characteristic length of scatterers/fractures	m
λ_0	Dominate wavelength	m
k_0	Dominate wavenumber	$\mathrm{m^{-1}}$
B_0	Seismic albedo	-
J^0	Incident energy flux density	$\mathrm{W\,m^{-2}}$
J^1	Scattered energy flux density	$\mathrm{W\,m^{-2}}$
σ_T	Total scatterer cross-section	$\mathrm{m^2}$
ρ_n	Number density of scatterers	$\mathrm{m^{-3}}$
g_0	Scattering coefficient/power	$\mathrm{m^{-1}}$
l^*	Mean free path	m
τ^*	Mean free time	s
S_w	Water saturation	%
d	Distance	m
S	Source position vector	m

Symbol	Description	Units
R	Receiver position vector	m
$\mathbf{r}$	Position vector	m
$\mathbf{D}_p$	Impulse response data cube	-
t_k	Centre of correlation window	s
t_w	Half correlation window width	s
K^m	Measured data decorrelation coefficient	-
K^T	Theoretical decorrelation coefficient	-
$Q(...)$	Sensitivity kernel	-
L_c	Correlation distance between model cells	mm
σ_m	Standard deviation of the model parameters	-

Abbreviations

AEs	Acoustic Emissions
CWI	Coda-Wave Interferometry
CWD	Coda-Wave Decorrelation
DAWS	Diffusing Acoustic Wave Spectroscopy
DWS	Diffusing Wave Spectroscopy
DNN	Deep Neural Network
EEW	Earthquake Early Warning
ESW	Early Warning Systems
GRU	Gated Recurrent Unit
LVDT	Linear Variable Differential Transformers
MRI	Magnetic Resonance Imaging
ML	Machine Learning
MLTWA	Multi-Lapse Time Window Analysis
NDT	Non-Destructive Testing
PSF	Posidonia Shale Formation
RELU	Rectified Linear Unit
RNN	Recurrent Neural Network
SAFOD	San Andreas Fault Observatory at Depth
SHM	Structural Health Monitoring
SNR	Signal-to-Noise Ratio
TOF	Time-Of Flight
UCS	Unconfined Compressive Strength
WM	Whitby Mudstone
WMF	Whitby Mudstone formation
XRD	X-ray Diffraction

Curriculum Vitæ

Reuben Denley Zotz-Wilson

Born: 08-01-1986 Tasmania, Australia.

Education

2004–2007	B.Sc of Mechanical Engineering University of Tasmania, Hobart.
2013–2015	M.Sc of Applied Geophysics Delft University of Technology, Delft, Eidgenössische Technische Hochschule, Zürich, Rheinisch-Westfälische Technische Hochschule, Aachen.

Experience

2008–2013	Wireline Engineer Schlumberger Oilfield Services

List of publications

■ Peer-reviewed publications of this thesis

[3] **Zotz-Wilson, R.**, Boerrigter, T., Barnhoorn, A., (2018), *Coda-wave monitoring of continuously evolving material properties and the precursory detection of yielding*, Journal of the Acoustical Society of America, 145,2,1060–1068. Chapter 2 of this thesis

[2] **Zotz-Wilson, R.**, Filippidou, N., Van Der Linden, A. ,Verberne, B. A., Barnhoorn, A.,(2019), *Coda-Wave Based Monitoring of Pore-Pressure Depletion-driven Compaction of Slochteren Sandstone Samples from the Groningen Gas Field*, Under Review - J. Geophys. Res. - Solid Earth Chapter 3 of this thesis

[1] **Zotz-Wilson, R.**, Douma L.,Sarout J., Dautriat J., Dewhurst D., Barnhoorn A., (2019), *Ultrasonic Imaging of the onset and growth of fractures within Partially Saturated Whitby Mudstone using coda-wave decorrelation inversion*, Under Review - J. Geophys. Res. - Solid Earth Chapter 4 of this thesis

Note that minor changes have been introduced to make the text consistent with the other chapters.

■ Full publication record

An up-to-date record of peer-reviewed publications and selected conference presentations is available at `https://www.researchgate.net/profile/Reuben_Zotz-wilson`.

978-94-6366-262-8